SEPTEMBER 2022

Ph.D. in Civil Engineering

HALUK IŞIK

REPUBLIC OF TURKEY

GAZİANTEP UNIVERSITY

GRADUATE SCHOOL OF NATURAL & APPLIED SCIENCES

SOIL BEHAVIOR AT THE GRAIN SCALE AND ITS EFFECT ON MACRO SCALE

Ph.D. THESIS

IN

CIVIL ENGINEERING

BY

HALUK IŞIK

SEPTEMBER 2022

SOIL BEHAVIOR AT THE GRAIN SCALE AND ITS EFFECT ON MACRO SCALE

Ph.D. Thesis

in

Civil Engineering

Gaziantep University

Supervisor

Prof. Dr. Ali Fırat ÇABALAR

by

Haluk IŞIK

September 2022

I hereby declare that all information in this document has been obtained and presented in accordance with academic rules and ethical conduct. I also declare that, as required by these rules and conduct, I have fully cited and referenced all material and results that are not original to this work.

Haluk IŞIK

ABSTRACT

SOIL BEHAVIOR AT THE GRAIN SCALE AND ITS EFFECT ON MACRO SCALE

IŞIK, Haluk
Ph.D. in Civil Engineering
Supervisor: Prof. Dr. Ali Fırat ÇABALAR
September 2022
158 pages

The objective of this study is to investigate soil behavior while taking into consideration its shape characteristics, and establishing a relationship between these characteristics and macro problems of soil. One of the key problems that will be looked at within the scope of this thesis is slope stability. When considering stability of slopes, the contribution of, if any, shape and size parameters to the calculation of shear strength of soils is not addressed in the literature. One may think that the reason for the absence of this particular topic in the literature could be that in slope stability, factor of safety generally provides us with enough safe room, leaving any further analysis especially anything that concerns micro mechanics of soil redundant. However, we argue that studying slope stability using only the continuum theories may not always be sufficient and that it could not allow us to leverage the full potential of strength of soil in our engineering designs. In soil mechanics, there are always many unknowns and even in slope stability there are still many topics yet to be researched. The brief literature review shows that micro mechanics of soil can have a significant effect on overall soil behavior. Although this study will be concerned with cohesion-less soils, we believe that it is still another step into understanding soil behavior in the context of slope stability.

Key Words: Soil Shape, Slope Stability, Digital Image Processing.

ÖZET

DANE ÖLÇEĞİNDE ZEMİN DAVRANIŞI VE BUNUN MAKRO ÖLÇEKTE ETKİSİ

IŞIK, Haluk
Doktora Tezi, İnşaat Mühendisliği
Danışman: Prof. Dr. Ali Fırat ÇABALAR
Eylül 2022
158 sayfa

Bu çalışmanın amacı, zemin davranışını şekil özelliklerini dikkate alarak incelemek ve bu özellikler ile zeminin makro sorunları arasında bir ilişki kurmaktır. Bu tez kapsamında incelenecek olan temel problemlerden biri şev stabilitesidir. Şevlerin stabilitesi göz önüne alındığında, eğer varsa şekil ve boyut parametrelerinin zeminlerin kesme dayanımının hesaplanmasına katkısı literatürde ele alınmamaktadır. Literatürde bu özel konunun bulunmamasının nedeninin, şev stabilitesinde güvenlik faktörünün genellikle bize yeterli güvenli alan sağlaması ve özellikle zeminin mikro mekaniği ile ilgili herhangi bir ek analiz bırakması olabileceği düşünülebilir. Bununla birlikte, sadece süreklilik teorilerini kullanarak şev stabilitesini çalışmanın her zaman yeterli olmayabileceğini ve mühendislik tasarımlarımızda zeminin mukavemetinin tüm potansiyelinden yararlanmamıza izin veremeyeceğini iddia ediyoruz. Zemin mekaniğinde her zaman birçok bilinmeyen vardır ve şev stabilitesinde bile hala araştırılması gereken birçok konu vardır. Kısa literatür incelemesi, zeminin mikro mekaniğinin genel zemin davranışı üzerinde önemli bir etkiye sahip olabileceğini göstermektedir. Bu çalışma kohezyonsuz zeminlerle ilgili olacak olsa da, bunun, şev stabilitesi bağlamında zemin davranışını anlamanın bir başka adımı olduğuna inanıyoruz.

Anahtar Kelimeler: Zemin Şekli, Şev stabilitesi, Dijital Görüntü İşleme.

Dedicated to Nawang Khechog,

the great Tibetan musical improvisor

ACKNOWLEDGEMENTS

I am forever grateful to my supervisor, Prof. Dr. Ali Fırat ÇABALAR, for his guidance and endless support throughout the course of this research. I am thankful for his encouragement and motivation.

I would like to extend my sincere gratitude to Asst. Prof. Dr. Nurullah Akbulut for his friendship and support and for helping with the necessary laboratory facilities and equipment for this thesis.

I would also like to thank my defense committee members - Dr. Nildem Taysi, Dr. Esra M. Guneyisi, Dr. Eyyub Karakan, and Dr. Murat Ornek for their insightful feedback, input and criticisms.

Finally, I would like to thank my loving and patient wife Batima, for enduring the effects of my frustrations and never wavering in her belief that I could see this thesis through to completion.

TABLE OF CONTENTS

Page

LIST OF TABLES

Page

LIST OF FIGURES

Page

LIST OF SYMBOLS

α	Angle of the sliding plane
β	Slope inclination angle
ε_q	Shear strain
ε_v	Volumetric strain
φ	Angle of friction
φ'	Effective angle of friction
γ	Bulk unit weight of soil (kN/m3)
γ_d	Dry unit weight of soil (kN/m3)
γ_w	Unit weight of water (kN/m3)
λ	Scale factor
ρ	Mass density of soil (g/cm3)
ρ_s	Grain density of solids (g/cm3)
σ’	Effective normal stress (kPa)
τ	Shear stress or mobilized shear stress (kPa)
τ_f	Shear strength of soil (kPa)
θ	Angle of inclination of interslice resultant force
b	Width of a slice
c	Apparent (total) cohesion (kPa)
c'	Effective cohesion (kpa)
e	Void ratio
g	Acceleration due to gravity (m/s2)
h	Average height of a slice
k	Permeability coefficient (m/s)
l	Length of a slice
u	Pore pressure (kPa)
w	Moisture content

$\mathbf{c_u}$	Coefficient of uniformity
$\mathbf{c_c}$	Coefficient of curvature
$\mathbf{D_r}$	Relative density of soil
F	Factor of safety
$\mathbf{G_s}$	Specific gravity
L	Total length of sliding surface
H	Depth of soil layer
$\mathbf{S_r}$	Degree of saturation
T	Inter-slice shear force (kN)
$\mathbf{V_s}$	Shear wave velocity (m/s)
W	Weight of each slice or total sliding mass (kN)

LIST OFABBREVIATIONS

ACS	Angular Crushed Sand
ASTM	American Society for Testing and Materials
AF	Angularity Factor
BS	British Standard
BSM	Bishop's Simplified Method
CCD	Charge-Coupled Device
CRR	Cyclic Resistance Ratio
CSS	Crushed Sand Sample
DIA	Dynamic Image Analysis
ESZ	Electrical Sensing Zone
FAP	Fly Ash Pellets
FE	Finite Element
FEM	Finite Element Method
FOS	Factor of Safety
GLE	Generalized Limit Equilibrium
GUI	Graphical User Interface
ICF	Isik Cabalar Shape Factor
ISO	International Organization for Standardization
JCM	Janbu's Corrected Method
JDM	Janbu's Direct Method
JGM	Janbu's General Method
JSM	Janbu's Simplified Method
LBS	Leighton Buzzard Sand
LD	Laser Diffraction
LE	Limit Equilibrium
LEM	Limit Equilibrium Method
NS	Narli Sand
OM	Ordinary method (Fellenius or Swedish method)

OMC	Optimum moisture content
OS	Ottowa Sand
PI	Plasticity index
R	Roundness (Wadell's Roundess)
RFEM	Random Finite Element Method
RRS	Rounded River Sand
SEM	Scanning Electron Microscope
SI	International System of Units
SPT	Standard Penetration Test
SF	Sukumaran Shape Factor
SM	Spencer's Method
SPOS	Single Particle Optical Sizing
SSR	Shear Strength Reduction
TS	Thrace Sand
TYS	Toyoura Sand
USCS	Unified Soil Classification System
VBA	Visual Basic for Applications

CHAPTER I

INTRODUCTION

1.1 General

Soils are particulate materials within which many interactions between individual particles develop. Geotechnical engineers usually idealize behavior of soil in order to utilize convenient theories based on continuum approach. They enable us to easily understand and categorize soils whether in-situ or at laboratory. However, there are limitations that comes with the use of this method. Instead of using continuum approach if we regard soil consisting of individual elements, we will be able to explain phenomena that are related with micro-mechanics of soil. In this study, we will analyze and investigate phenomena related with the micro mechanics of soil. The stick-slip which is one of the phenomena that is related with micro-mechanics of soil could be correlated with the seismic activity of the earth. A special importance will be given to slope stability analysis while considering shape and size characteristics of soil.

When dealing with soil mechanics problems, geotechnical engineers usually utilize theories based on continuum approach. However, there are limitations that come with the use of this method. Soil is actually composed of many small individual materials, which in their sum make up what we perceive as soil. Hypotheses that were based on the continuum approach were established in the 18th century by Charles-Augustine de Coulomb who was a French physicist. A notable example of his work includes the Mohr-Coulomb theory, which is a mathematical model that describes how brittle materials like concrete or rubber piles respond to shear, or normal stress, that we use in continuum mechanics. The Mohr-Coulomb theory, which was named in honor of Christian Otto Mohr and Charles-Augustin de Coulomb, is widely used in many solutions of geotechnical problems. Coulomb's contribution to the development of the theory appears in his work titled *"Essai sur une application des règles des maximis et minimis à quelques problèmes de statique relatifs à l'architecture".* The theory can

effectively express the failure criterion in soils in a single equation. This equation is given as:

$$\tau = \sigma \tan\varphi + c \tag{1.1}$$

where σ and τ denotes the normal and the shear stress respectively, and ϕ is the angle of internal friction and c represents cohesion. The equation can be applied to any material that is regarded as a continuum medium, and soil is one of them. The convenience that this equation gives is that the characteristics of what make up soil could be expressed in only two terms: ϕ (angle of internal friction) and c (cohesion). While this method of approach could prove to be very convenient, dealing with individual elements that make up soil and analyzing their interactions between them and their environment explains different phenomena within soil such as capillary effect, stick-slip phenomenon or Van der Waals forces that we also observe in nature. Understanding these phenomena in soil and developing theories will enable geotechnical engineers to have more tools to approach soil problems.

Estimation of shape parameters have been an interesting topic since there soil particles can be represented and found in a variety of ways, and there have been a number of methods presented by researchers regarding this subject. The shape of soils in terms of micro characteristics is concerned is usually categorized into 3 parameters: (1) sphericity, which is sometimes also called form, (2) angularity or roundness, and (3) roughness or texture (Barrett 1980, Bowman et al., 2001, Sukumaran & Ashmawy, 2001, Santamarina & Cho, 2004). Using these parameters, the soil particles can be defined numerically which can in turn modeled using computer algorithms. Commonly used terms with respect to particle size in geotechnical engineering is form, roundness, and roughness.

The stability of slopes is one of the important research topics in geotechnical engineering. The analyses help researchers understand the causes of slope failures in earth and rock-fill dams, embankments, and other excavated slopes (Das et al., 2011; Xue et al., 2015; Stead, D., 2016; Kumar, A., Rathee, R., 2017, Wang, X., 2017). The information can be used to plan future soil stabilization programs and prevent disasters, injury, or loss of life that might be caused by slope failures. Due to slope failures, there have been many disasters involving loss of life, injuries, and property

damage (Chowdhury et al., 2009; Ahmed et al., 2011; Petley, D., 2012; Sepúlveda S.A., Petley D.N., 2015; Görüm, T., Fidan, S., 2021). Slope instabilities may occur due to changes in geometry, changes in external forces in natural soil slopes that have stayed dormant for a long period of time (Abramson et al., 2002). Therefore, stability of slopes is the focus of many studies in geotechnical engineering.

The objective of this thesis is to present a novel shape parameter for soils based on image analysis using computer algorithms, and use this shape parameter in order to understand its effect on soil properties and draw a correlation. A large-scale slope stability test will be conducted for this purpose.

1.2 Statement of the problem

The need to investigate the soil on micro scale has been realized in the early 20th century. In fact, Karl von Terzaghi addresses this very topic in his work titled "Old Earth Pressure Theories and New Test Results" in 1920. He talks about how Coulomb purposely established his theories without actually considering individual grains of soil in order to derive a convenient and very useful method. According to Terzaghi (1920), even though Coulomb's methodology was an efficient way to describe a one aspect of the earth-pressure theory and laid the groundwork as far as the hypothesis is concerned, the necessary innovations were not made even long after the methodologies were proposed. In order to see further beyond the model, some of the old principles should be put aside and new models should be developed based on the fact that sand is actually composed of individual particles (Terzaghi, 1920). Therefore, as convenient as it may be, when we approach geotechnical engineering problems using only continuum hypotheses, we are leaving out some essential parameters of soils that may be useful in understanding the other phenomena which are related with soil, such as stick-slip, force chains, seismic vibrations.

1.3 Research aims and objectives

The primary aim of this thesis is to analyze the mechanic behavior of soils, analyze the slopes under the plate loads with relation to the shape differences in the micro scale, and find correlations that explains the soil behavior in this respect. A novel shape factor is presented that defines a novel shape parameter for soils that depends on image analysis using numerical algorithms. The applicability and effectiveness of the shape

factor is examined by performing a series of plate load tests. A load is applied on top of the soil until failure. The data are collected from the two flat disc pressure cells and four button type pressure cells which were installed inside the box. The slope stability analyses are performed using sand with different shape parameters. A loading frame made of steel with a capacity of 40 t was used to carry out the tests.

The main objectives of the current research are as follows:

(1) To define a novel shape parameter for sands using inverse Fourier transformation. The present study is thought to be the first in the literature that takes advantage of Fourier transform for shape generation and definition of a shape parameter.

(2) To conduct plate load tests on soil with different gradations by simulating the performance of a sandy slope and examine the stress and strain behavior in the large-scale soil box.

(3) To correlate the results of the analysis with the shape parameter.

1.4 Methodology

The works that has been performed in order to achieve the research objectives of this thesis can be outlined as follows:

1- Review the extensive literature on relevant theoretical and experimental work, focus on Fourier transformation for the shape analysis,
2- Two educational computer programs were developed that are aimed at civil engineering students in order to help them learn the concepts of geotechnical engineering in a laboratory setting.
3- A computer algorithm based novel shape parameter was developed that has a high correlation value with the traditional roundness parameter and that also can produce more consistent results for shapes that have too many concave corners, and better differentiate rounded particles between each other.
4- Necessary standards regarding the experimental procedures have been studied, and preparations of samples were done accordingly in order to prepare an experimental program.

5- A soil box model with dimensions of 3m × 2m and in 1.5m in height having a steel frame with a capacity of 40 tons was used to carry out the large-scale tests.

1.5 Significance of the research

Slope stability has always been an important research area due to the disasters, injury, or loss of life that might be caused by slope failures. Over the past few years, there has been an increasing number of research in image analysis, and as the computers advance more complex definitions for shape emerge. By successfully applying the inverse Fourier analysis in sandy soils a novel shape factor can be defined that can more realistically characterize the soil. The shape factor can be used to find a correlation between shape and size of the soils in micro scale and the soil properties. This would lead to the following outcomes:

- Analyzing the shape of soils more effectively and efficiently
- Decreasing the time that is needed to analyze the shape
- Understanding of slope stability failures from a new perspective
- Providing an alternate solution to the problems

1.6 Layout of the thesis

This thesis studies the micro shape characteristics of soils, and its effect on the strength of the sandy soil. A new shape factor, which is denoted as ICF for soils was presented using 8 separate categories of granular materials (NS, CSS, TS, LBS, OS, TYS, FAP, and mica). The thesis is comprised of six chapters and they are organized as follows:

Chapter 1 summarizes the general information, contribution, and the aim and objectives of the thesis.

Chapter 2 presents an extensive literature review on the subject of the shape and size characteristics of soil particles. It gives the methods to determine particle size and also presents a computer program that was developed for soil classification

Chapter 3 presents the materials and methods that were utilized in preparation for the

laboratory experiments. The methodology of the sample preparation techniques was explained in details. This chapter also includes the description of the novel shape parameter and a remote data logging and monitoring system to use in the large-scale slope box model.

Chapter 4 presents the findings of the tests and discussions of the data gained from the shape size studies and the large-scale slope model studies in the laboratory and field studies. The grain size distribution, shape, index properties, and strength of the sand using during the experiments are discussed, compared, and interpreted.

CHAPTER II

LITERATURE REVIEW

2.1 Shape and Size Characteristics of Soil Particles

2.1.1 Micrometer and Orders of Magnitude

If we consider the orders of magnitude, micron lies in the lowest boundary of what is called the human scale. Orders of magnitude are defined as ranging from astronomical to Planck region. Although the term micron has been revoked from official usage to be changed with micrometer by the SI (International System of Units) in 1967, it is still commonly used in practice. A micrometer is an SI derived unit of length which is 10^{-6} of a meter.

2.1.2 Granular Matter

A granular material is a conglomeration or aggregation of diverse macroscopic solid particles that usually form a heterogeneous sum. Lower size limit for each of the grains in this sum is defined to be 1 μm. As for the upper size limit of the grains, we can consider asteroids in our solar system to be individual grains of asteroid belts. In this case, the diameter of each grain could be more than 1 km. Each particle within a granular material follows Newton's laws, ie., when there is a contact between particles, reactive forces develop. As simple as they are to be defined, they actually possess a tremendously complex behavior. They are even defined as being a new form of matter by some researchers.

2.1.3 Sand Particle Shape and Formation

The sand particles can be categorized into three in regards to its formation: the creation of the quartz crystal that occurs inside the magma that is cooled, attrition of the material that the particle originated from, and the release of the particles.

Granite is what makes up the majority of these grains, which forms during the gradation of rock crystals. The detailed study of the composition of the granite material suggests a

gradual crystallization of magma which is siliceous in character. The crystals which form are partially of a solid mixture feldspar and quartz, which originate approximately at 983 Kelvin following the bigger feldspar grains that have already created. The quartz forms right after the temperature hits 846 Kelvin, at which point they are named high quartz. At this stage, they go through a transformation which alters their bond angle and creates low quartz. During the instant at which the quartz particles fuses in granite magma, their shape and size properties are permanently defined (Smalley 1966). Sand grain quartz have a characteristic where the measurement of elongations is about 1.3, which suggest that the formation of the crystals occur due to a cooling procedure rather than a weathering one (Smalley 1966). The evidence that supports this idea can be given as (1) parallel to the elongated axis, quartz crystals do not prefer to fracture, (2) a differential scuffing cannot be a probable result of the elongation that is seen parallel to this axis, and (3) the grains that are intact and not having been weathered are elongated. Since the elongation of schist - which is also a kind of this soil - is observed to be rather big, this eliminates the hypothesis that the reason that quartz has this shape is through a metamorphic process.

Elongation of grains during their creation could be explained by two mathematical models. In the first model, the focus is on the change of shape from an elevated β (stable above 1570 K and 35 kb) to a lower α (stable below 846 K and 1 kb) quartz during the transformation. An equation was developed by Nabarro (1940) using theory of elasticity in order to produce a mathematical relation which includes the energy in the grains that is cooling and its compressibility, its volume change, and the ratio of the diameters of the ellipse.

$$SE = K \cdot \Delta V \cdot \frac{1}{3} f\left(\frac{b}{a}\right) \tag{2.1}$$

In Equation 2.1, E denotes the energy, ΔV denotes the volume change and b/a ratio is the ratio of the diameters of the ellipse. It is seen that the value of E becomes the smallest for a disk with a b/a value is zero. And it reaches its maximum value when the b/a value is greater than one.

In the second model, the quartz crystal cools to 323 K from 1073 K, while the b/a ratio increases to 1.1 (Smalley 1966). Moreover, while the transformation is taking place to a low β quartz, a shrinkage of volume is observed. The explanation for that behavior is that

during the process the change only occurs at the short axis, meaning that the stresses induced by this shrinkage will lead to a tensile stress gain in the other axis, resulting in elongation and cracks.

2.1.4 Surface Features of Sand Particles

The shape that defines the sand particles is fixed and permanent during their formation. However, textural characteristics can change significantly over time via chemical or mechanical processes. During these processes, small particles can be created. The different mechanisms of chemical weathering are shown in Figure 2.1. Margolis and Krinsley (1974) studied these processes and shown that more than seven different types of cleavages might occur in quartz. Between the two particles a uniform compression takes place. This can also occur if one particle is facing a surface that is relatively rough. Concoidal fractures is the consequence of this as can be seen in Figure 2.1a. These fractures can be defined as round shaped or cup shaped. However, they can also be fairly irregular depending on the environment that the particle is in. Glacial environments and granite which is newly weathered are the environments which make the particles most prone to fractures. The particle size is one of the important factors that contribute to this particular fracture. This type of fracture is observed mostly in bigger particles owing to their more imperfect nature. The fractures usually cover a small part of the surface. The reason for this behavior is that the stress appears at the crack that is most visible

In Figure 2.1b a quartz particle is shown featuring grooves and t-shaped patterns, these are basically indents that are at its outer layer. It can be clearly seen in these images that these notches are cut across numerous cleavage plates that run parallel to each other. As the notches sink deeper, they become less prominent until they eventually vanish. This is a particular behavior that is observed in subaqueous environments. It characterizes the abrasion that is occurring in this type of environments since there is more impact between the grains. As the particle size gets smaller the notches are grooves get less prominent, especially at the particle diameter size less than 300 μm.

The grooves that are straight or almost straight are not seen frequently. These grooves are usually less than 30 μm with a thickness of around 3 μm. They are generally observed inside a subaqueous environment. They are usually observed on particles that have a

diameter of at least 400 μm since smaller grains do not possess enough momentum to produce the grooves.

A similar process to that of formation of grooves in the particles takes place during abrasion of metals. While polishing the metals, the metal starts grinding on the grinding surface, resulting in propelling small chips of metals, which are usually at the end of lines that occur because of the abrasion. In an analogous fashion to metals, small chips come out of the particles during their contact, which form the notches and grooves that is observed.

In Figure 2.1c a microscopic image of a particle is seen, where a series of thin plates that run parallel to each other and are directed along the previously formed cleavage plates. These plates can be continuous depending on the curvature of the grains and the angle which they make with the particle surface. Plate relief is usually a few micrometers. The chemical process has the defining factor that plays a role in creating the form of the particle, which can differ greatly such as being wavy or jagged.

When the particles are crushed the inverted cleavage, plates can be seen and they generally persist after the mechanical wear. The edge of a particle is the most likely place for the cleavages. However, they can practically be seen at any location in the particle. Almost all natural environments possess these plates, and the most common location for these plates are near glaciers and along the coast.

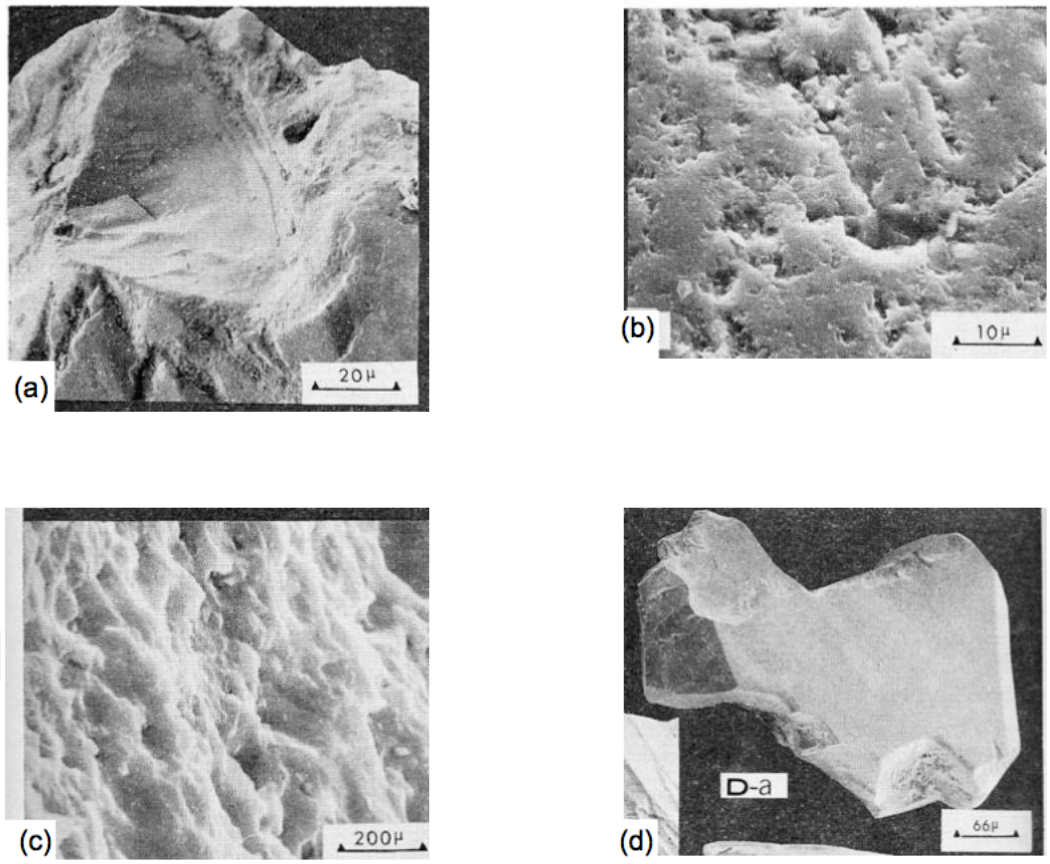

Figure 2.1 Mechanical abrasion of quartz sands. (a) Conchoidal fracture, (b) v-shaped grooves, (c) inverted cleavage plates and (d) flat particle broke off from a sand particle along a cleavage plane (Margolis and Krinsley 1974).

In a windy environment, upturned cleavage plates have a major function that is important for rounding sand particles. During simulations conducted with a wind machine, Kuenen (1960) observed that the plates appear mostly at the edges of the particles rather than in the hollow parts. The abrasion smooths them out, and given enough time the particles become more like a sphere.

There is also another type of weathering, namely chemical weathering that takes place at the surface of quartz particles. It creates oriented or non-oriented etch type pits or overgrowths, which are generally a layer of film around the particle. The two types of chemical processes can completely alter the surface features of particles, which were previously of mechanical origin. Its attributes can be difficult to differentiate from that of mechanical weathering. However, a careful examination can reveal the processes caused by mechanical action since they tend to be conspicuously cleaner.

In every environment result from chemical processes can be seen to a varying extent. However, generally certain features are more dominant in a given particle which gives away its originating location. For example, when marine sands are examined, it can be seen that they mostly feature crystallographically-oriented pits. Oriented etches are observed in sea water, whereas non-oriented etch pits are usually caused by surface weathering, etc.

When a sand particle is observed throughout many years it is obvious that it goes through both mechanical and chemical weathering. The two types of actions both produce their results which affect the surface feature of the sand particle. For instance, in a desert, all of the sand particles are subject to chemical weathering, which results in the particles to be coated with a thin layer of silica. The strong wind in the desert causes formation of the upturned cleavage plates. When the effects from both of these actions are observed over a long period of time, a balance will occur. In hot and humid environments chemical weathering is the dominating cause, whereas in dry and cold environments the opposite is true, where the dominating cause is the mechanical one.

2.1.5 Clay Particle Shape and Formation

Four factors determine the crystalline structure of a clay mineral, which are as follows (Mitchell 1993):

• Sheet Type

• Unit Cell Order

• Bonding Mechanism

• Substitution

The molecular composition of clay minerals reveals that they have two fundamental building elements. The first of these is the structure called silica tetrahedron, which is a strong geometrical structure made up of a single central silicon atom bonded by 4 oxygen atoms. These structures bind together in order to construct silica sheets. The second one is aluminum tetrahedron, which is a molecular unit that has an aluminum and a magnesium atom that is bonded by eight oxygen atoms. Aluminum octahedrons combine to form gibbsite sheets, and magnesium octahedrons combine and produce brucite sheets.

Clay mineral is formed by these sheets making layers on top of each other successively in a particular manner. The layers which repeat continuously has a smallest section which is called the unit cell.

The thickness of a particular clay particle is determined by the bond strength that the unit cells have between each other. The cells can be bonded in groups of two or three in a number of patterns. The most common ones are Van der Waals forces, ionic bonds, and hydrogen bonds. The unit cell that is made up of the very soft phyllosilicate group of minerals called montmorillonite is divided into three sheets, since they are only bonded together by Van der Waals forces, which are very weak and they allow layers to separate from one another. Because of that the structure that makes up kaolin can be up to 100 times stronger that this unit structure due its bonding mechanism, which is hydrogen bonds (Mitchell 1993).

The shape of the particle can be influenced by strength of bonds that its structure has. An aluminosilicate clay mineral that is called Hallolysite has two variants: 7a and 10a, which are shown in Figure 2.2. The 7a structure can be thought as being very similar to kaolinite except a water later sandwiched between every other sheet. In kaolin structure, the width of the gibbsite sheet is 8.93 Å, while the width of the free gibbsite is 0.31 Å shorter than that, which suggests that while forming the silica sheets, the gibbsite stretches. Additionally, the existence of water between the layers makes the bonds weaker, allowing the gibbsite to have a direct contact with water that shrinks it. Because of the curvature of the structure, the water stays facing an inward position, while the silica tetrahedron stays on the outer perimeter (Weaver 1989). SEM photographs of halloysite and kaolin are presented in Figure 2.3.

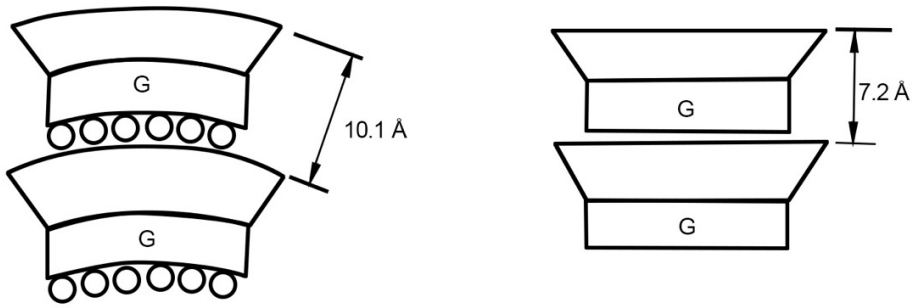

Figure 2.2 Schematic view of Halloysite-10a (left) and Halloysite-7a (right) unit structure (Mitchell 1993).

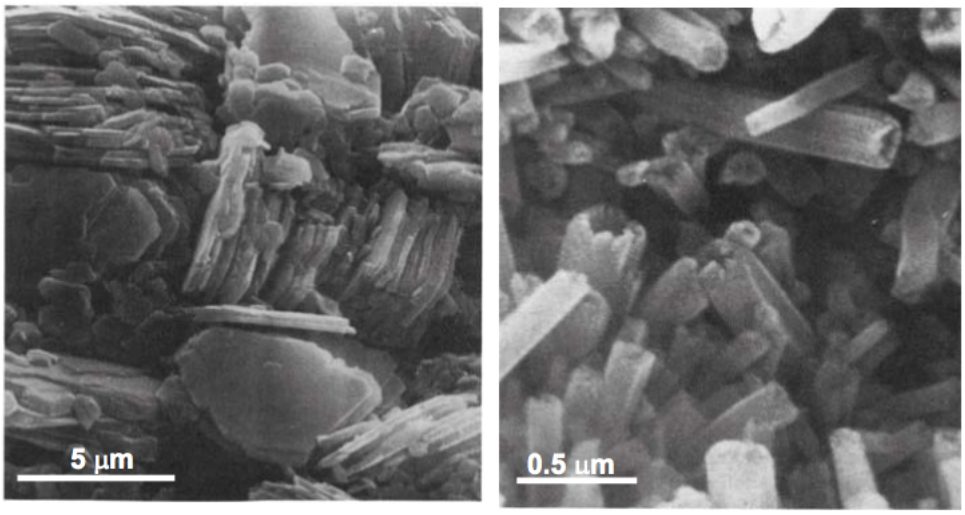

Figure 2.3 SEM images of kaolin (left) and halloysite particles (right) (Mitchell 1993).

The formation of clay minerals also gets influenced by the phenomenon called isomorphous substitution in which one structural cation gets replaced by another one that has a similar size. Some of the common replacements are aluminum and magnesium cations, which takes the place of silicon. The shape of montmorillonite can be given as an example that illustrates this procedure. After a significant number of silicon atoms displace, the particles that substitute their place gives the mineral a slender shape. The reason for this behavior is that the replacement ions cause a strain to take place in the mineral (Mitchell 1993).

Clay minerals which are of completely different geometries but almost identical crystalline structures can be produced with this phenomenon. An extensive study was done on 57 halloysite samples by Nagasawa and Miyazaki (1975). In the study, the samples were divided into 4 different groups: (1) Minerals that are produced by hydrothermal alteration of granite, or a volcanic rock, (2) minerals that are produced by the modification of volcanic glass, (3) minerals that are produced by dissolution of feldspar, and finally (4) minerals that are produced by epigenesis of feldspar. The conclusions of their research revealed that there is a strong correlation that exists between the formation type of the mineral and its morphology. Halloysite minerals that were allowed to be grown on feldspar particles or in the rock cracks resulted in a tubular formation. Particles that are formed during the substitution of allophones sometimes resulted in aggregates that are of a very short tubular character, which in turn gave them a round shape.

2.1.6 Particle Shape and Size

In soil mechanics, the traditional method to assess particle size distribution is by the use of sieve analysis and sedimentation methods. Sieve analysis is utilized for coarse particles (particles having a diameter which is bigger than or equal to 63μm) while sedimentation methods are utilized for fine particles (particles having a diameter which is smaller than 63μm) According to the sieve analysis method, particle size is defined by the size of the square holes of each sieve. And in the sedimentation method, the size is correlated with the falling velocity of the particles. Neither of these methods tell anything about the form, roughness or angularity of individual particles of soils. As one may imagine, a very angular particle and a smooth one can both pass through the same size sieve. And if we consider two soil samples consisting of two different particle shapes, we can arrange them so that they will have the exact same grain size distribution; and yet their behavior will be different.

The shape of soils with respect to their micro characteristics is generally divided into 3 parameters: (1) sphericity, which is sometimes also called form, (2) angularity or roundness, and (3) roughness or texture (Barrett 1980, Bowman et al., 2001, Sukumaran & Ashmawy, 2001, Santamarina & Cho, 2004) as can be seen in Figures 2.4-2.5. Using these parameters, the soil particles can be defined numerically which can in turn modeled using computer algorithms. Forming a model using these three arguments, which explains the internal structure of soil grains is an idealized one, and may not entirely cover whole aspects of soil particles. However, this approach will be the one to be utilized throughout the thesis.

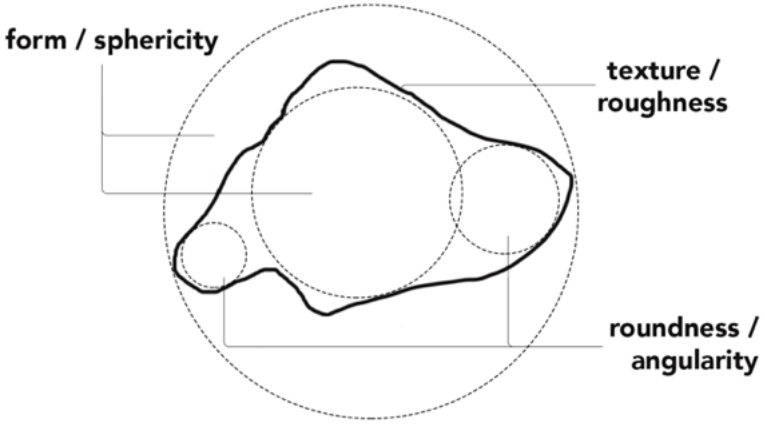

Figure 2.4 Particle shape parameters (Modified after Barrett, 1980).

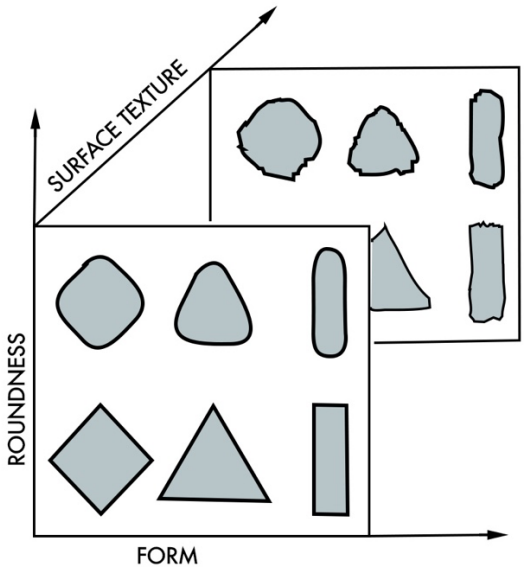

Figure 2.5 Diagram showing the interrelationship of form, roundness and roughness (Barrett 1980).

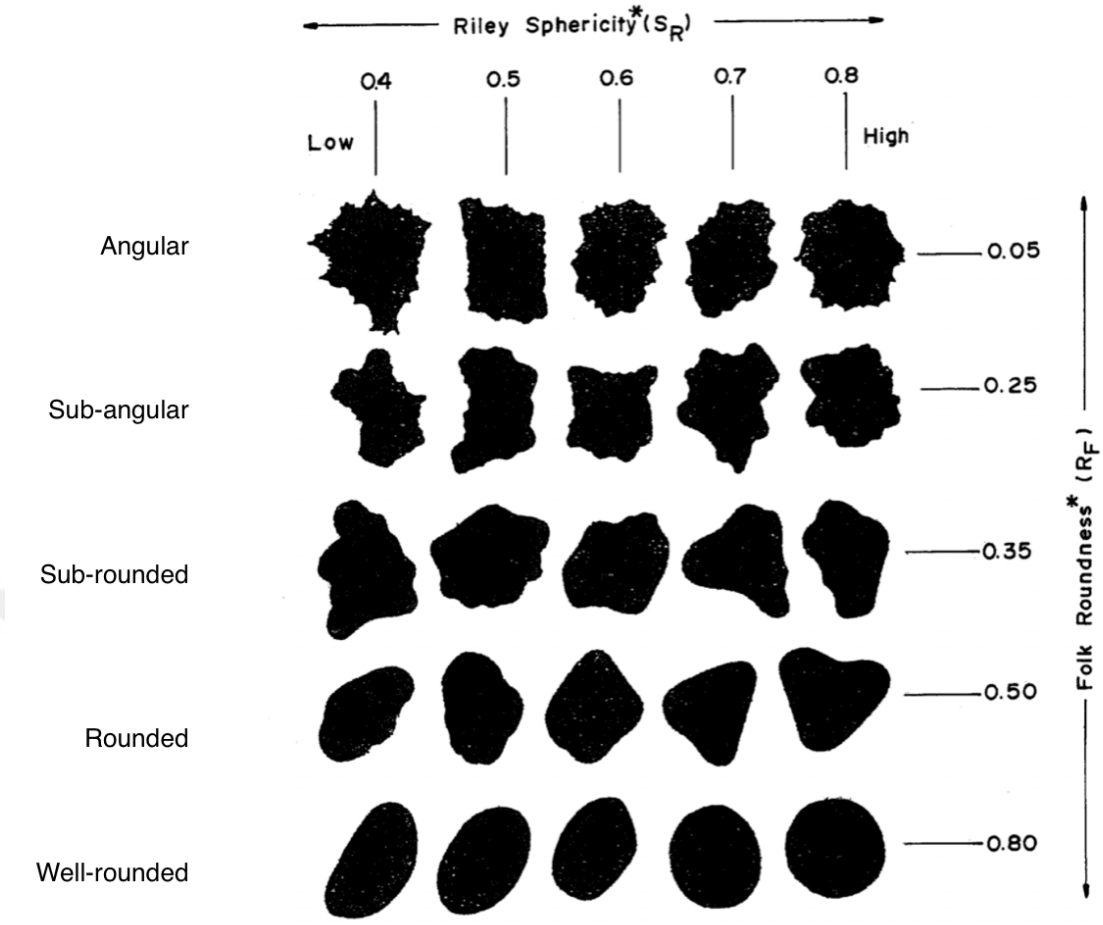

Figure 2.6 Degrees of roundness according to Russel-Taylor-Pettijohn (after Schneiderhöhn, 1954) (quoted by Norman, 2000 (c)).

Figure 2.6 shows a visual chart of definitions of angularity and sphericity of particles. This method was introduced by Powers (1953) and was later revised by other researchers (Krumbein and Sloss, 1963). The method relies on 2-dimensional representations of soil particles. These kinds of visual charts could be used to quickly identify and categorize soil grains by looking at them. These charts were developed prior to 70's when computer systems were in their infancy. Obviously, in today's technology, complex computer models and algorithms provide much more precise results, especially if 3-dimensional models were to be used.

One of the main categories to divide the particles in is called form. There is a variety of forms that the particles are represented with, such as needle-like, lath-like, platy, tubular, elliptical, cubical, spherical, and flat. There is at least one way of quantifying this vast array of diverse forms, and that is by comparing the particles by their length ratios of their

vertical axes. A minimum of 15 individual parameters have been found by Barrett (1980) that can describe the form using the aforementioned ratios. A parameter that is commonly used in the literature is aspect ratio, otherwise called elongation, is described as the ratio of the long axis to that of the intermediate axis. Another parameter is flatness that is defined by the ratio of the intermediate axis to the ratio of the short axis. Other common parameters used to describe particle form is eccentricity and sphericity. The volume of the particle divided by its circumscribing sphere is called sphericity (Wadell 1932). However, this definition of sphericity also includes roundness in it. A redefined definition of this parameter was given as the surface area of the particle divided by the surface area of a sphere that is equal in volume to the particle (Santamarina et al., 2001). The definition of eccentricity of an elliptical particle is given as δ_ρ / R_ρ which can also be rewritten $R_\rho = \delta_\rho \cos(2\theta)$ in polar coordinates.

Sukumaran and Ashmawy (2001) presented a new method to quantify form, which is based on measuring the deviation of a given particle outline with respect to a perfect circle. The process starts first by slicing the particle outline image into a number of segments. Slices are made from the center of the outline towards the outside edges. The outer points are then connected in order to form a polygon. A comparison is made to determine the ratio of orientations of connecting lines of the perimeter and the ones created by each slice of the polygon. The new shape factor then can be defined by factoring in the difference in orientations denoted by α, and the number of sample points which is denoted by N.

$$SF = \sum_{i=1}^{n} \left(\left| \frac{\alpha_i(particle)}{\alpha_i(flat\_particle)} \right| \right) \cdot 100\% \tag{2.2}$$

$$SF = \sum_{i=1}^{n} \left(\left| \frac{\alpha_i(particle)}{N.45°} \right| \right) \cdot 100\% \tag{2.3}$$

As can be seen in Equations 2.2-2.3, the average value of curvature radius that corresponds to every individual corner (r_i) is divided by the radius value of the maximum inscribed circle in order to find roundness parameter (Wadell 1932). This defines the

roundness parameter in two dimensions, however, by using additional radius value in the third dimension this concept can be extrapolated into three dimensions.

Since the definition of a corner is usually subjective, it becomes problematic to assess the roundness value numerically. As a solution to this problem, Sukumaran and Ashmawy (2001) presented a novel method that describes the roundness mathematically. The first step is to construct the polygon using the slicing method. Then a parameter called the angularity factor is introduced, which is calculated by finding the internal angles (β) of the polygon and the internal angles of the corresponding polygon drawn inside a circle by the following equation:

$$AF = \frac{\sum_{i=1}^{n}\left(\beta_{i,particle} - 180°\right)^2 - \sum_{i=1}^{n}\left(\beta_{i,circle} - 180°\right)^2}{3 \cdot (180°)^2 - \sum_{i=1}^{n}\left(\beta_{i,circle} - 180°\right)^2} \cdot 100\% \qquad (2.4)$$

When this angularity factor is compared with Wadell's definition of roundness, Sukumaran and Ashmawy (2001) found a significant scatter, which further underlines the subjective nature of the roundness value of Wadell.

Considering the particle roughness, it is evident that every surface has roughness to a certain extent that can be defined and therefore scale can be deemed critical as far as characterization of this parameter is concerned (Santamarina et al. 2001).

An understanding of the formation of the soils is also necessary in order to evaluate soil particles according to the places where they are found. It appears that most of the clastic sediment is formed through the weathering and erosion processes of their parent rocks. These parent rocks can be igneous, sedimentary, or metamorphic in nature and the sediments that are formed from them possess resistant components of primary rock-forming minerals (which are mainly quartz and muscovite mica) while the clay minerals are formed by weathering of non-resistant components of primary rock-forming minerals.

The original formation, moss defects and the rock cycle determine the size of the resistant components inside the mineral grains. Moss defects are defined to be the fracture planes that appear in the crystals, which are formed during the high-to-low transformation of quartz (Moss & Green, 1975). These defects cause grains to split into more pieces during the weathering of rocks.

The main factor that defines the shape of quartz crystals found in igneous rocks is their internal atomic structure. Although small distortions that occur during the high-to-low transformation of quartz do have some effect on the size, they are not the main factor (Bokman, 1952). Considering the metamorphic rocks, an additional factor i.e., the distortion caused by metamorphic action, plays a role in their shape (Smalley, 1966). In granite rocks the general shape of the quartz crystals are of a bulky type (approximately equi-dimensional), and in metamorphic rocks they are of a bulky to platy type depending on their origin i.e., igneous or sedimentary. Mica particles always have a sheet-like shape, while their sizes vary according to what kind of weathering mechanisms they were exposed to. Clay particles also have a sheet-like structure, but the mechanism by which the particles have their form is their atomic structure. Depending on the strength of bonds between the individual sheets, clays acquire their thicknesses.

There are combinations of mechanical and chemical processes that take place during the time span starting from the release of grains from the parent rocks through their deposition. There are no definitive ways with which we can formulate how these processes actually alter the sizes and shapes of the particles. However, they do have a correlation with the particle size. Krinsley & Smalley (1973) and Margolis & Krinsley (1974) have shown that coarse quartz particles (typically >50μm) typically break by concoidal fracture whereas fine particles (typically <50μm) form fractures along their cleavage planes. Smalley and his co-workers (Smalley & Glendinning, 1991, Rogers & Smalley, 1993, Smalley, 1995, Wright, 1995, Jefferson et al., 1997, Wright et al., 1998, Assallay et al., 1998, Wright, 2001, Wright, 2004, Smalley et al., 2004) have extensively studied the possible mechanisms behind the formation of huge amounts of silt and clay-sized quartz particles, which include significant quantities of loess deposits. Their results have shown that glacial grinding, aeolian abrasion, fluvial communition, salt weathering and frost weathering are the chief factors that might contribute to producing massive amounts of silt and clay-sized quartz particles. The overall shape of these particles found to be platy (Blatt, 1987, Rogers & Smalley, 1993). Similar results have been found for the fine fraction of tailings by Vermeulen (2001) and Wesselloo (2004).

In summary, the nature of formation and (i.e., the type of weathering mechanism and transporting agent) and the depositional environment are the factors by which the surface features (angularity and roughness) of coarse particles are formed to be either smooth and

well-rounded or rough and angular (Margolis & Krinsley, 1974). In the case of fine particles, since they tend to fracture along their cleavage planes, they do not have surface irregularities and their shapes can be easier to define.

2.2 Soil Behavior and Methods to Determine Shape and Size

2.2.1 Methods to Determine Particle Shape

Estimation of shape parameters have been an interesting topic since there soil particles can be represented and found in a variety of ways, and there have been a number of methods presented by researchers in order to estimate form, roundness and roughness. These mentioned parameters and corresponding expressions are presented in Tables 2.1 & 2.2, and are briefly elaborated in the following paragraphs.

One of the terms regarding the particle shape is called form, and it defines the general outline or characteristics of the particle from a broad perspective, which can be given either in 2 dimensions or 3 dimensions. Experimental and theoretical studies have been presented in this topic by numerous researchers (Wadell, 1933; Wadell, 1935; Zing, 1935; Krumbein & Sloss, 1963; Hawkins, 1993; Podczeck, 1997; Sukumaran & Ashmawy, 2001; Hentschel & Page, 2003; Alshibli & Alsaleh, 2004; Cho et al., 2005). One of the interesting methods that was used in the literature is Fourier transform. Wettimuny & Penumadu (2004) used inverse Fourier transformation in order to reconstruct boundaries of sand particles, which they presented as a method to estimate the shape of sand particles. Several other studies were done using 2 dimensional outlines of particles based on Fourier series of lower order harmonics (Ehrlich & Weinberg, 1970; Ehrlich et al., 1980; Clark, 1981; Santamarina et al., 2001) or Fourier descriptor methods (Clark, 1981; Thomas et al., 1995, Bowman et al., 2001). The disadvantage of these 2D estimates is that there is no means to differentiate bulky and platy particles, especially when they have similar outline. There are other researchers, such as Zingg, 1935, Krumbein, 1941, Aschenbrenner, 1956, and Sneed & Folk, 1958, who studied form in 3-D, and have proposed 3D estimates of form, based on the three-orthogonal dimensions of a particle. These estimates are not efficient to be applied to very small particles, since it requires obtaining orthogonal dimensions of particles. True sphericity parameter, proposed by Hawkins (1993) is also not very efficient for small particles. Wadell (1932) found a 3D estimate based on the specific surface (surface area per unit mass) measurements. But the problem with this method is that since it is related with surface area it will be sensitive to surface irregularities and pores, and might give an undesired result.

The second parameter is called roundness, which defines irregular features of surface of a particle. The traditional definition given by Wadell (1933) is found by finding the

average of corner radiuses and dividing them by the radius of the outlining circle for the particle. One caveat of this definition lies in the fact that the definition of the corners is subjective, which can change the calculations dramatically. To overcome this issue, comparison charts that are designed to visually aid the experimenter have been proposed by different researchers (Powers, 1953; Krumbein & Sloss, 1963; Cho et al., 2005). The disadvantages of using charts to examine the shape is that they will provide slightly different results depending on the person, and that they only provide limited options to choose from. The angularity parameter that was presented by Lee (1964) estimates the roundness better in comparison to Wadell's roundess. In his study, Lees (1964) shows that Wadell's roundness is not a good measure to be applied for crushed/broken rock particles and he came up with a new term which he called 'angularity number'. The angularity number is found by relative projection of the tip of corner of a particle from the center of its largest inscribed circle (See Figure 2.4 & Table 2.2). However, the procedure still requires the corners to be consistently defined, a feature which Lee's method is still lacking as seen in the previous definitions. An alternative option is to remove the corners and analyze the shape in a different manner in the case of Fourier transformation or fractal techniques. To overcome this difficulty, fractal technique (Mandelbrot, 1977, Orford & Whalley, 1983, Vallejo, 1995, Hyslip & Vallejo, 1997, Gori & Mari, 2001) can be utilized, but the fractal dimension is shown to be less sensitive to the particle's morphology (Sukumaran & Ashmawy, 2001). Furthermore, the fractal technique does not differentiate the roundness and roughness. Hofmann (1959) proposed another term, named coefficient of angularity, which is defined as the ratio of specific surface of particles (measured by indirect method based air flow permeability) to the calculated value (assuming the particle's shape is spherical). Hofmann showed that the increase in angularity causes a deviation between the measured and calculated specific surface values. Other researchers showed that it works well in the case of nearly equi-dimensional particles (Holubec & D'Appolonia, 1973). Hoffmann's angularity method can work by combining the form for the cases when the particles are rather long and/or platy since sieve and measured specific surface are influenced by the elongation. The development of image analysis techniques allowed several researchers (e.g. Yudhbhir & Abedinzadeh, 1991, Sukumaran & Ashmawy, 2001, Alshibli & Alsaleh, 2004) to establish more ways of evaluating the angularity. The formulations developed by some of these researchers are presented in Table 2. Yudhbhir and Abedinzadeh put forward a

formula that considers the count of average tangents, or how many protrusions a particle has along its boundary, and the particle perimeter. Sukumaran and Ashmawy (2001) also developed a method, which is based on calculating the differences of the inner angles of the polygon drawn inside the circle with regards to particle outline itself (i.e., angle between chords BC and CD in Figure 2.4) and the particle (i.e., angle between chords EF and FG in Figure 2.4). Sezer (2008) took advantage of digital imaging techniques in order to evaluate roundness and form of sand particles. In his research, some approximations were made in order to make the calculations. Among these approximation methods were line sections, counting of boxes, and fractal area and perimeter. Sukumaran & Ashmawy's method is the most straightforward and efficient one, since the method is able to distinguish the particles having varied angularities, and since the process can be quickly adapted into computer using an image analyzer. The definitions for this method is shown in a cross section of a sand particle in Figure 2.7.

Roughness is another measure that is related with surface irregularities, but at a much lower scale (i.e., asperities) than roundness. In addition, the scale to measure roughness varies with the particle size. Roughness can be observed by naked eye under an ordinary microscope or using SEM, however it is not easy to characterize this term. There are some researchers who studied roughness by observing 2D outlines of particles with the use of fractal method (Hyslip & Vallejo 1997) and higher-order harmonics (or descriptors) of the Fourier methods (Bowman et al., 2001). The measurements for the roughness found using these methods may not exactly define what the actual roughness is, or may not lie with the definition of a roughness, because there could be fine surface features of a particle that cannot be captured through its 2D projection. In order to overcome this problem, 3D techniques are necessary. Currently there are a number of 3D surface measurement tools are available (e.g., stylus systems, focus detection measurements, interferometric methods, stereo-comparators, scanning tunneling microscope, atomic force microscope etc.) which can be utilized to devise 3D methods. Stout & Blunt made a thorough review of these tools and instruments in their study (2000). A quick look at these 3D surface measurement instruments reveals that they only allow the top surface of a particle to be characterized. Alshibli & Alsaleh (2004) utilized optical interferometry approach in order to arrive at a definition of surface roughness of the top surface of sand particles. Because of the nature of particles, measurement of each of them is expected to

take a rather long time. Instead of measuring surface roughness a group of researchers proposed measuring the surface area (Blott et al., 2004). In addition to aforementioned tools there are also more sophisticated tools such as laser scanning and X-ray CT, with which it is possible to acquire the three-dimensional images of particles (Podczeck & Newton 1995; Lanaro & Tolppanen 2002; Taylor 2002; Kim et al. 2002; Garboczi 2002; Abou-chakra et al. 2004; Wang et al. 2004). However, they do pose a limitation in that, they are not very efficient in capturing the fine surface features of particles.

Table 2.1 Selected definitions of particle form

Shape parameter	**Formula**	**Range**	**Dimension**	**Reference**	**Shape parameter**
Sphericity	$\frac{s_a}{S_a}$	0 - 1	3-D	Wadell, 1932	Sphericity
Projection sphericity	$\frac{d_c}{D_c}$	0 - 1	2-D	Wadell, 1933, 1935	Projection sphericity
Elongation ratio	$\frac{l}{L}$	0 - 1	2-D	Zingg, 1935 (cited in Barett, 1980)	Elongation ratio
Flatness ratio	$\frac{S}{L}$	0 - 1	3-D	Zingg, 1935	Flatness ratio
Intercept sphericity	$\sqrt[3]{\frac{l \cdot S}{L^2}}$	0 - 1	3-D	Krumbein, 1941	Intercept sphericity
Working sphericity	$\frac{12.8\sqrt[3]{p^2 q}}{1+p(1+q)+6\sqrt{1+p^2(1+q^2)}}$ *where* $p=\frac{S}{l}$, $q=\frac{l}{L}$	0 - 1	3-D	Aschenbrenner, 1956	Working sphericity
Shape factor	$\frac{L \cdot S}{l^2}$	0 - ∞	3-D	Aschenbrenner, 1956	Shape factor
Maximum projection sphericity	$\sqrt[3]{\frac{S^2}{L \cdot l}}$	0 - 1	3-D	Sneed & Folk, 1958 (cited in Barett 1980)	Maximum projection sphericity
True sphericity	$\frac{d_{vs}}{D_{cs}}$	0 - 1	3-D	Hawkins, 1993 (cited in Santamarina et al., 2001)	True sphericity

Table 2.1 (Continued)

Inscribed circle sphericity	$\frac{d_{ic}}{D_{cc}}$	0 - 1	2-D	Hawkins, 1993 (cited in Santamarina et al., 2001)	Inscribed circle sphericity
Shape factor	$NS = Co + H_4 + H_3 + H_2 + H_1$	-	2-D	Podczeck, 1997	Shape factor
Normalized shape factor	$\frac{\sum_{i=1}^{N} \alpha_{i,particle}}{N \times 45^{\circ}} \times 100\%$	0 - 100	2-D	Sukuraman & Ashmawy, 2001	Normalized shape factor
Form factor	$\frac{4\pi A}{p^2}$	-	2-D	Henschel & Page, 2003	Form factor
Sphericity	$\frac{1}{N}\sum_{i=1}^{N}\left\lvert \frac{D_{equ(i)}}{d_{S(i)}} - \frac{D_{equ(i)}}{d_{L(i)}} \right\rvert$	> 0	2-D	Alshibli & Alsaleh, 2004	Sphericity

Table 2.2 Selected definitions of particle roundness and roughness

Shape parameter	**Formula**	**Range**	**Dimension**	**Reference**	**Shape parameter**
Wadell's roundness	$\sum\left(\frac{r}{R}\right)/N_c$ or $\sum\left(\frac{r}{R}\right)$	0 - 1	2-D	Wadell, 1932	Wade's roundness
Angularity	$\sum(180-a)\frac{X}{r}$	0 - ∞	2-D and 3-D	Lees, 1964	Angularity
Angularity	$\frac{\sum T_i}{n \times \text{average number of grains}}$	-	2-D	Yudhbir & Abedinzadeh, 1991	Angularity
Normalized angulary factor	$\frac{\sum_{i=1}^{N}\left(\beta_{i,particle}-180\right)^2 - \frac{360^2}{N}}{3\times(180)^2 - \frac{360^2}{N}} \times 100\%$	0 - 100	2-D	Sukumaran & Ashmawy, 2001	Normalized angulary factor
Roundness	$\frac{1}{N}\sum_{i=1}^{N}\frac{P_{act(i)}}{\frac{\pi\left(d_{S(i)}+d_{L(i)}\right)}{2}}$	> 1	2-D	Alshibli & Alsaleh, 2004	Roundness
Roughness number	$\frac{\sum \text{actual surface of the element}}{\sum \text{projected surface of the element}}$	> 1	3-D	Lange et al., 1993	Roughness number
Average roughness	$\frac{1}{M}\sum_{i=1}^{M}\sum_{i=1}^{M}\lvert Z_{ij}\rvert$	-	3-D	Alshibli & Alsaleh, 2004	Average roughness

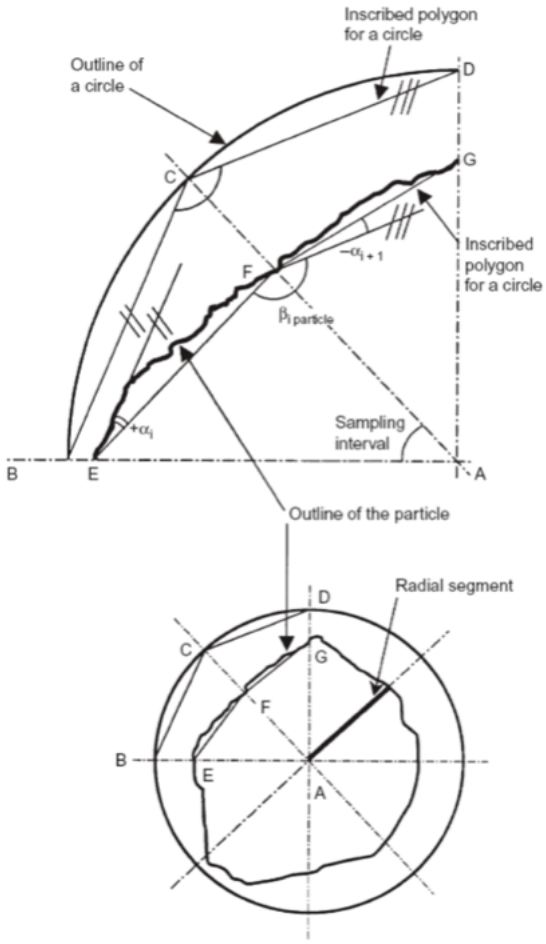

Figure 2.7 Sukumaran and Ashmawy's method of angularity (Sukumaran & Ashmawy, 2001).

Several different modes of a particle shape can be acquired through the use of Fourier analysis. The method makes use of convergent trigonometric series in order to trace the outline of a shape as shown in Equations 2.5-2.6 (Bowman et al. 2001).

$$R(\theta) = a_0 + \sum_{n=1}^{N} (a_n \cos(n\theta) + b_n \sin(n\theta)) \tag{2.5}$$

$$x_m + iy_m = \sum_{n=-\frac{N}{2}+1}^{N/2} (a_n + ib_n) \cdot \cos\left(\frac{2\pi \cdot n \cdot m}{M} + i \cdot \sin\left(\frac{2\pi \cdot n \cdot m}{M}\right)\right) \tag{2.6}$$

Equation 2.5 shows the traditional method of Fourier transform. In Equation 2.6, the method of Fourier descriptor can be seen. The second method makes use of complex numbers, which allows it to be used in cases where the outline of the particle retraces itself. Therefore, two different radius values can be associated with a single θ value. In both of the equations, phase angle is represented by θ_i, and the coefficients for the orders of the harmonics are represented by a_n and b_n.

The different characterizations of shape are represented by the level of harmonics. As the harmonics level increase they capture more details and they define shape in incrementally finer details. Using the Fourier descriptors, roundness is represented with a harmonics level of 10, whereas higher harmonic levels are necessary in order to represent roughness (Santamarina et al. 2001). Characterizations of a particle shape gradually changing from a basic shape to more detailed one that closely matches the original shape is shown in Figure 2.8 (Garboczi 2002). A significant amount of information can be gained from the usage of the Fourier method. The method allows the representation of the particles to be given numerically which makes it possible to reproduce them. However, there are more than one coefficient that describes the shape rather than a single parameter (Bowman et al. 2001).

In a fractal system, how large the unit of measurement is dependent on the measured property. Using this concept, the size of the measured property is inversely proportional to the unit of measurement as illustrated in Figure 2.9. The distance between the lines that are parallel to each other indicate the unit measurement, while the polygon perimeter indicates the property that is being measured, as seen in the diagram. An estimation of the length of a fractal line can be given by the following equation:

$$P(\lambda) = n\lambda^{1-D_R} \tag{2.7}$$

In Equation 2.7, $P(\lambda)$ represents the fractal length, λ represents the unit length, n is the constant of proportionality, and D_R is the fractal dimension.

This type of analysis can only work if the property that is being studied can be considered self-similar. Hyslip and Vallejo (1997) categorize the sand particles as having a bi-fractal feature meaning that the researchers studied the structure and texture of the sand particles as having a fractal nature, while at the same time being independent of each another. Self-

affinity has been another feature of a number of materials according to Chaiai (2002). This feature is important, since it makes the analysis of surface roughness possible using the fractal system. Several researches have shown correlations between fractal dimension and surface roughness (Militky & Bazjik 2001, Parrot 2005, Ayala-Landeros et al. 2018).

A graph of surface roughness as a function of fractal dimension is given in Figure 2.10. In the figure, there are 6 sand samples numbered 1 through 6, and as the numbers increase the surface features of the samples get smoother. An apparent trend can be seen between the roughness values and the fractal dimensions. However, since a distinction was not made between structural and textural aspects, inconsistencies are seen for the particles that exhibit smoother features.

Fractal analysis poses two major drawbacks when it comes to analyzing particle shape. The first one is the range of the surface feature length to apply the fractal analysis. The second one is that it is not possible to describe the form of the particle using the fractal dimension. This requires a different kind of shape analysis in order to properly characterize the shape of the particles (Sukumaran and Ashmawy 2001).

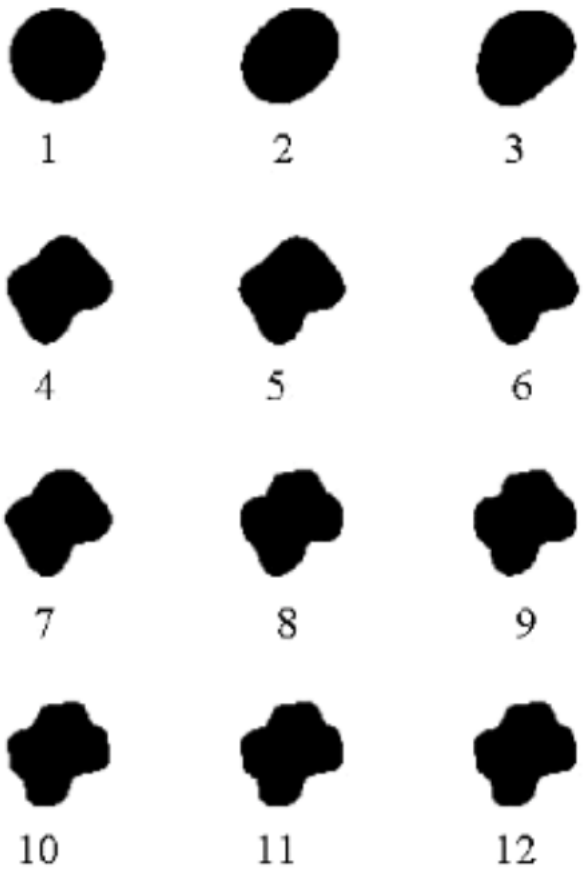

Figure 2.8 Gradual change in the characterization of particle shape using Fourier descriptors (Garboczi 2002).

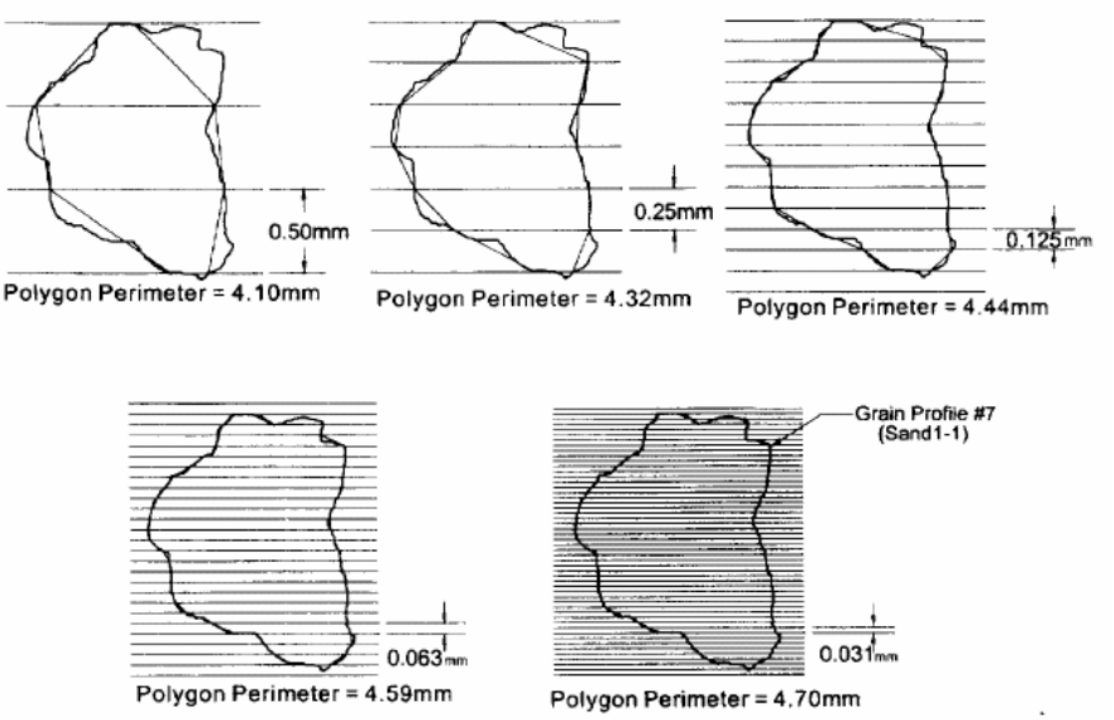

Figure 2.9 Fractal analysis of sand grains (Hyslip and Vallejo 1997).

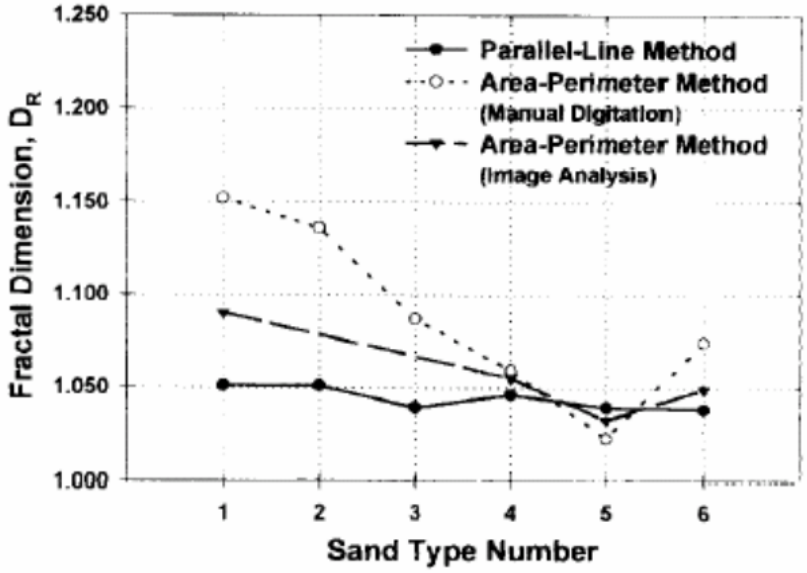

Figure 2.10 Fractal dimension versus sand roughness. Six sand samples (sand types 1-6) are examined ranging from rough (sand type 1) to smooth (sand type 6). (Hyslip and Vallejo 1997).

2.2.2 Methods to Determine Particle Size

In order to get a reliable picture of size of a particle its size parameters in all three dimensions has to be known. Therefore, particle size involves more than one parameter. Considering the highly irregular nature of soil particles, several researchers suggested different definitions and/or measurement techniques for the determination of particle size. Among the techniques to measure particle size are:

- Sieving
- Sedimentation
- Electrical sensing zone (ESZ) or Coulter counter
- Laser diffraction (LD)
- Dynamic image analysis (DIA)
- Single particle optical sizing (SPOS)
- Microscopy techniques

Every single one of these techniques originates from a different principle (or definition), and is applicable for particles of a certain range. The techniques are explained in the following paragraphs. It is important to note that all of these mentioned techniques give similar results for the spherical particles.

Sieving or sieve analysis is performed by a procedure, which involves passing the soil sample through certain number of sieves. Therefore, the particle size in this method is determined by the length of the holes of the sieves that the particles pass through. It is only useful for coarse particles (>63μm) (BS 1377-2:1990).

According to sedimentation methods (hydrometer or pipette or x-ray gravitational sedimentation i.e., sedigraph) the particle size is defined using a sphere having the same velocity with an equivalent diameter that settles in the same liquid. The calculation of the diameter is made using the Stokes law, which necessitates a spherical particle shape and a laminar flow. Usually, sedimentation methods are applicable for particles of size 0.1 – 100μm. However, in soil mechanics, pipette or hydrometer method is used for fine particles passing 63μm sieve (BS 1377-2:1990). From this, it is clearly evident that the

fine particles, for which the sedimentation is used, are platy. Also, it is known that in the case of platy particles, as the drag resistance increases, the settling of the particles slows down. This means that the size of platy particles will be underestimated using the sedimentation method. The effect will be more pronounced as the particles exhibit even more platy feature.

The size of the particle is given as the diameter of the particular particle reshaped into a sphere that has the same volume of the original particle according to the ESZ (BS ISO 13319:2000) method. The process starts by placing the particles in an electrolyte solution, and making the them flow through an opening with the use of electrical current. The passing particles displace an equal amount of electrolyte in volume, which in turn produces the voltage pulses. As per the Coulter principle, the particle volume that is displaced is directly proportional to the strength of the voltage pulse. The method can only be used for the particles that are between sizes 0.4 microns and 1200 microns.

An equivalent sphere for a given particle can be produced using the LD method (BS ISO 13320-1:1999), which is based on measuring the diffraction patterns. The principle behind the method is that, as the particle size decreases the diffracted light off of a given particle will be at a higher angle. The calculation is done with the assumption that the particle is a sphere. However, for elongated and platy particles, this causes an estimation of a highly concentrated volume (Hayton et al. 2001). Despite this, the calculations of size remain unaffected due to the reason that diffraction pattern does not have influence over a particle in the third dimension. The ratio between the actual volume concentration presented to the LD apparatus and volume concentration obtained from the apparatus may potentially provide a measure of form of particles. However, since the particles can be observed to have arbitrary orientations in a given cross-section, this can affect the results of the size analysis of particles given the turbulent flow. Additionally, assumptions for the visual properties of the particle can also be taken into consideration. Particle sizes between 0.1 – 2000μm can be analyzed using this method.

The DIA gives an estimated area equivalent circular diameter of a particle as the particle size (Xu et al., 2003). The particles are homogeneously dispersed in the medium, and circulated constantly. During the circulation, images of the particles are captured using a CCD camera, at a high rate. The diameter of each individual particle is then estimated from their projected areas. In the process each particle will be imaged multiple times but

in different orientations and thereby the particle orientation effect will be minimized. Particle sizes between 20 to 2500μm can be analyzed using this method.

The SPOS method (White, 2003) also provides the particle size in terms of estimated area that is equal to circular particle diameter, but uses a different principle than DIA. In this method, a laser beam is emitted across the flow path of the particles onto a detector through the sensor chamber. The particles are then made to pass through the sensor chamber under high-speed laminar flow conditions. The output voltage from the sensor is then recorded and sampled at higher frequency. If there are no particles along the flow path of the laser beam, then a steady baseline voltage, vb is observed, as the particles pass through the sensor they leave a shadow over the detector and a change in the output voltage. The magnitude of this change in voltage is proportional to the projected area of the particle. The particles pass through the sensor by intersecting their length, or width (whichever is larger) perpendicularly to the laser beam. The phenomenon that makes this possible is the fact that the flow being laminar. Since the orientation of particles happen arbitrarily, the results may be skewed. However, in comparison to the effects caused by the diffraction of laser, this is negligible. Therefore, the SPOS measurements are superior to those of LD. Also, the SPOS method covers a much broader array of sizes, which is between 1 – 5000μm.

The size as well as the shape of the particles can be assessed through the use of microscopes. However, in the literature they have been mainly used as a supplemental method rather than a main method since there are limitations involved with respect to the number of particles that can be evaluated efficiently in the case of coarse particles, and the resolution in the case of fine particles. There are a number of available microscopy methods and the sizes of particles that can be applied to it. Figures 2.11 and 2.12 shows the comparisons of particle size distributions obtained from the laser diffraction and sieve methods.

Among the particle sizing methods described above, the ratio of particle sizes obtained from ESZ and SPOS methods may perhaps provide a better estimate of particle form in three dimensions.

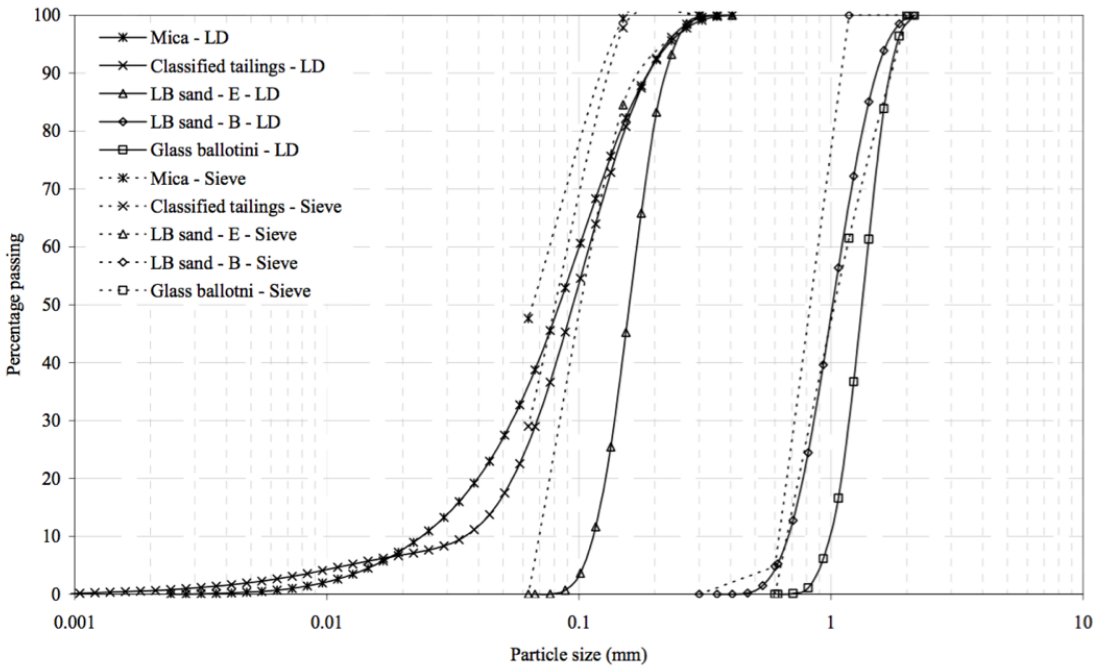

Material	Ratio of D_{50}(LD)/ D_{50} (sieve)
Glass ballotini	1.27
LB sand – B	1.22
LB sand – E	1.70
Classifies tailings	1.17
Mica	1.24

Figure 2.11 Comparison of particle size distributions obtained from the laser diffraction and sieve methods (Chandra, 2008).

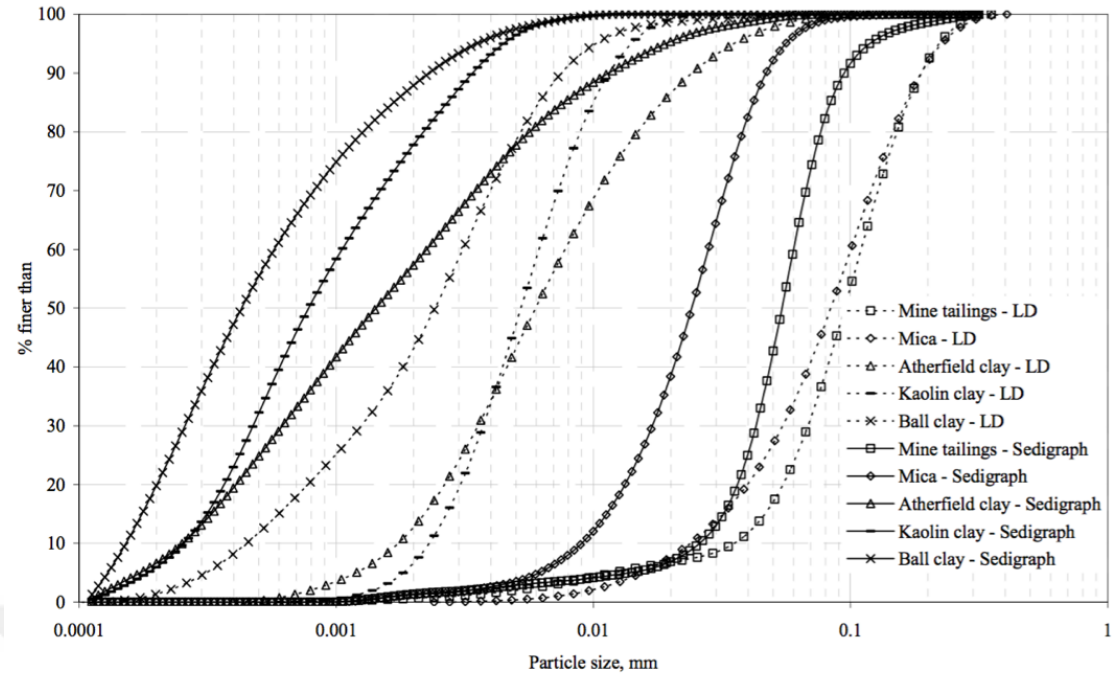

Material	Ratio of D_{50}(LD)/ D_{50} (sedigraph)
Classified tailings	1.76
Mica	3.46
Kaolin clay	6.58
Atherfield clay	4.26
Ball clay	5.95

Figure 2.12 Comparison of particle size distributions obtained from the laser diffraction and sedigraph method (Chandra, 2008).

2.2.3 Particle Forces

In order to investigate soil on micro scale a basis upon which particle forces are defined needs to be established. Santamarina (2001) divides particle forces in relation to the location of the generation mechanism into three broad categories. These are; forces due to applied boundary stresses, particle level forces and contact forces. Skeletal forces which are related with the particle forces are especially important. Recent advancements in numerical micro-mechanics (Cundall and Strack 1979) have enabled more methods to be developed to better understand the distribution and evolution of inter-particle skeletal forces in soils. Santamarina found that both normal and tangential forces develop at contact points of soil particles when an effective stress is applied at the boundary, and gave the following relation.

$$\underline{N} = \sigma' d^2 \left[\frac{\pi(1+e)^2}{12} \right] \tag{2.8}$$

Equation 2.8 states, considering the particles are spheres, and for randomly packed spheres, that the mean normal contact force N is proportional to the void ratio e.

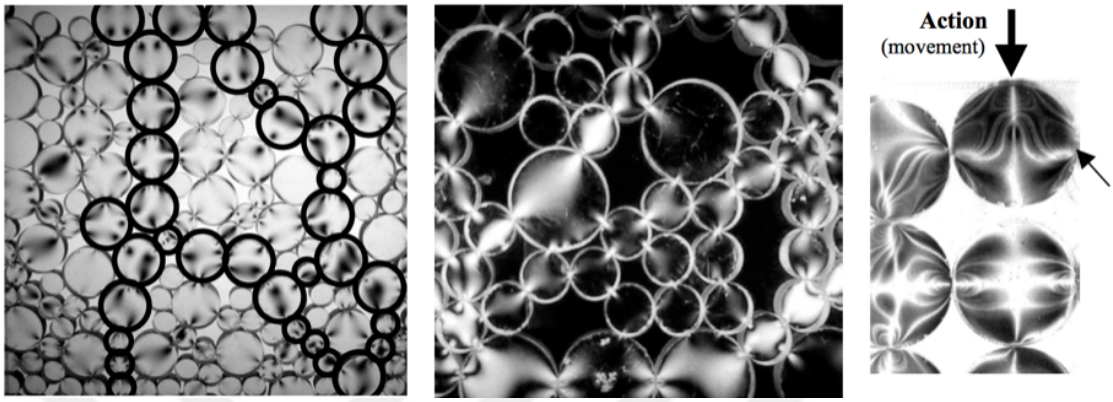

Figure 2.13 Skeletal force distribution and photo elastic disks.

Figure 2.13 shows that chains of particles form column like structures. These structures resist the applied boundary stress (Drescher and de Josselin de Jong 1972; Oda et al. 1985), and bear resemblance with fractals in structure. In the literature it is shown that there are many particles that are within the granular medium and act as movable particles that are outside of the force chain system and they do not carry skeletal load.

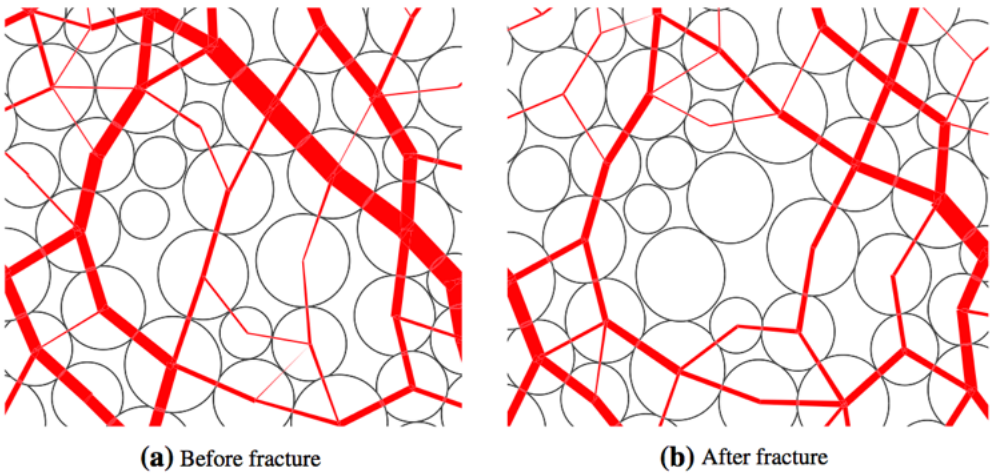

Figure 2.14 Force chains (Bi et. al, 2010).

Figure 2.14 shows how these force chains actually destruct and reconstruct. Thicker lines represent larger forces. Skeletal forces can also be investigated using DEM (Discrete Element Modeling).

2.2.4 Discrete Element Modeling

Because particles have highly irregular shapes and there is limited knowledge regarding 3-D discrete element modeling, traditionally 2-D analyses were utilized in studying the influence of particle shapes on mechanical response of cohesionless soil. Sukumaran et al. (2008) showed that DEM can be used in modeling particle shape in both two and three dimensions, and can give reliable results in comparison to experimental analyses. Figure 2.15 shows two samples of soil that they gathered in order to conduct a discrete element modeling of soil.

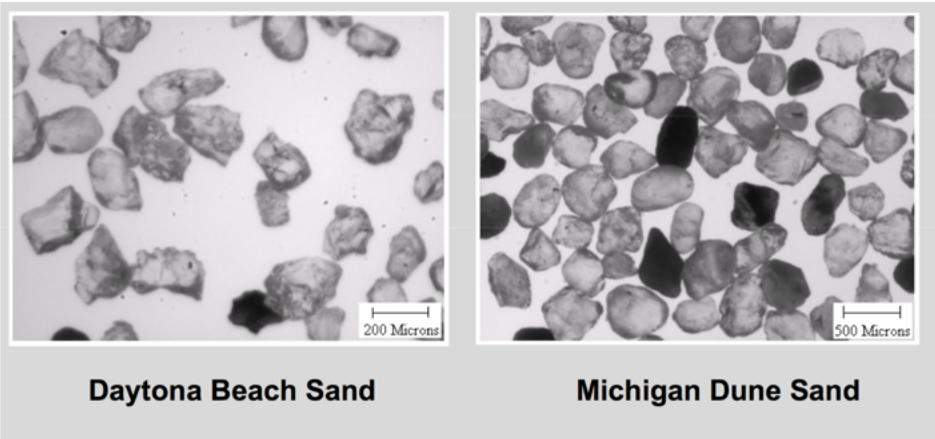

Figure 2.15 Sand samples taken for Discrete Element Modeling (Sukumaran et al., 2008).

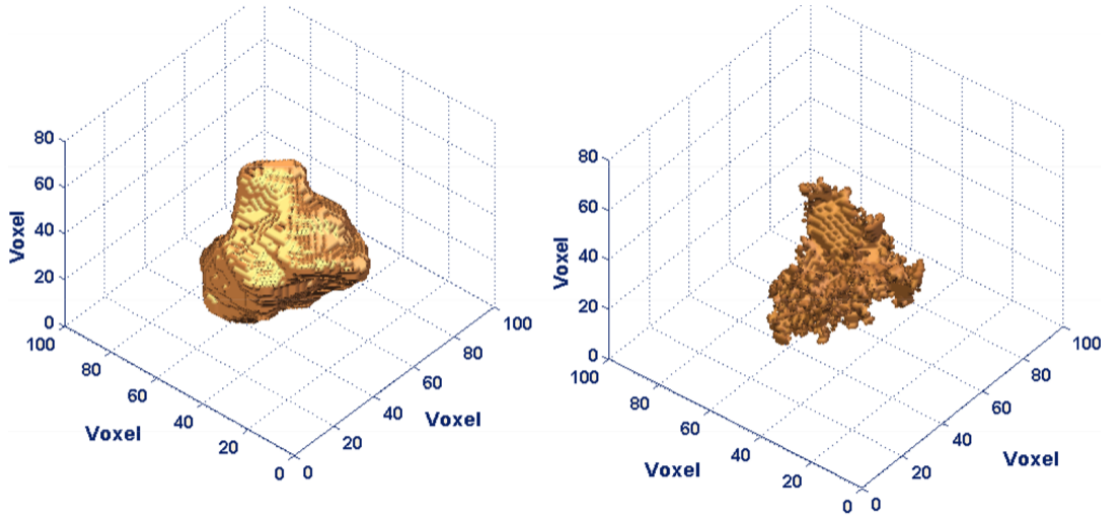

Figure 2.16 Daytona beach sand skeletonization process (Sukumaran et al., 2008).

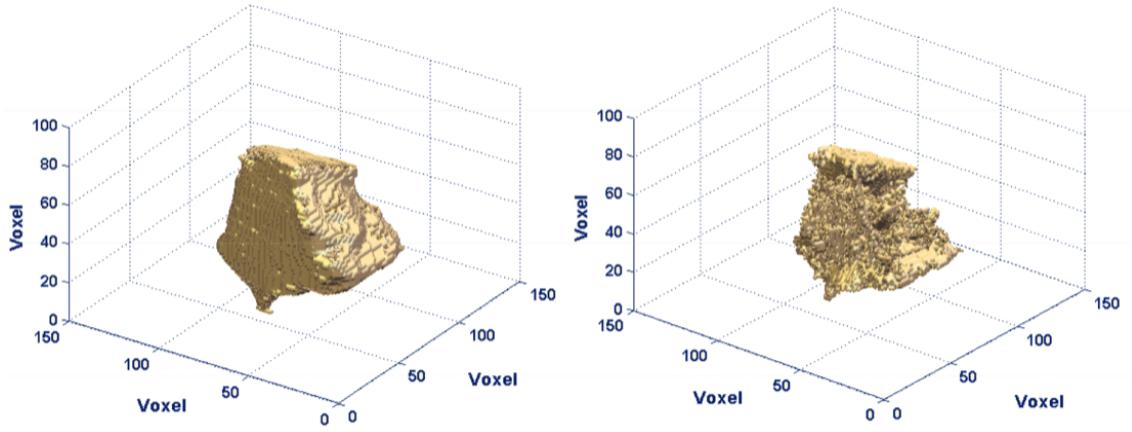

Figure 2.17 Michigan dune sand skeletonization process (Sukumaran et al., 2008).

Sukumaran et al. (2008) produced skelotonized 3-D models of two samples taken from Daytona Beach and Michigan as can be seen in Figures 2.16-2.17.

They calculated the number of spheres needed to capture the whole shape. At the end of the procedure about 95% of the volume was covered.

They performed a transformation on circular particles which were generated to a specific grain size distribution. An equivalent angular sand was achieved which was randomly rotated.

There are some recent studies that is specifically related with particle mechanics of soil that have enhanced our understanding of soil behavior. Some of the researchers was mentioned in the previous section. This section will look into results and conclusions of such studies.

Table 2.2 Results showing angle of internal friction (Sukumaran et al., 2008)

Material	2-D Simulation	3-D Simulation	Experimental values
Daytona Beach sand	27°	39° - 43°	37.4°
Rounded particles	17.2°	25° - 26.6°	24.4° - 27°

Sukumaran et. al (2008) studied DEM simulation of soil samples and circular disks. They performed simulated direct shear tests on models consisting of 800 particles where mean particle size was 0.375 mm, inter-particle friction coefficient was 0.5, porosity was 0.30, particle density was 2500 kg/m^3, and velocity was $5x10^{-3}$ m/step. Table 2.3 demonstrates that angle of internal friction values for 2-D and 3-D simulated soil particles fall in line with the experimental values. The experimental values that they had for rounded particles were from other studies (O'Sullivan et al., 2004; Philips et al., 2006).

Sukumaran et al. found that the algorithms that they used in the investigations could accurately model irregular particle shapes both in 2-D and in 3-D. They demonstrated that stress-strain and volumetric behaviors of simulated materials exhibited a behavior that is similar to that of angular and rounded particles. The results of their findings are shown in Table 2.3.

2.2.5 Stick-slip Behavior

Çabalar and Clayton (2010) investigated the drops and fluctuations in stress-strain relationships of sand grains. They studied the periodic arrangement of the grains and the motion that occurs. They also applied Gutenberg-Richter law in order to illustrate a relationship between the return period of these fluctuations and the deviatoric stress amplitude.

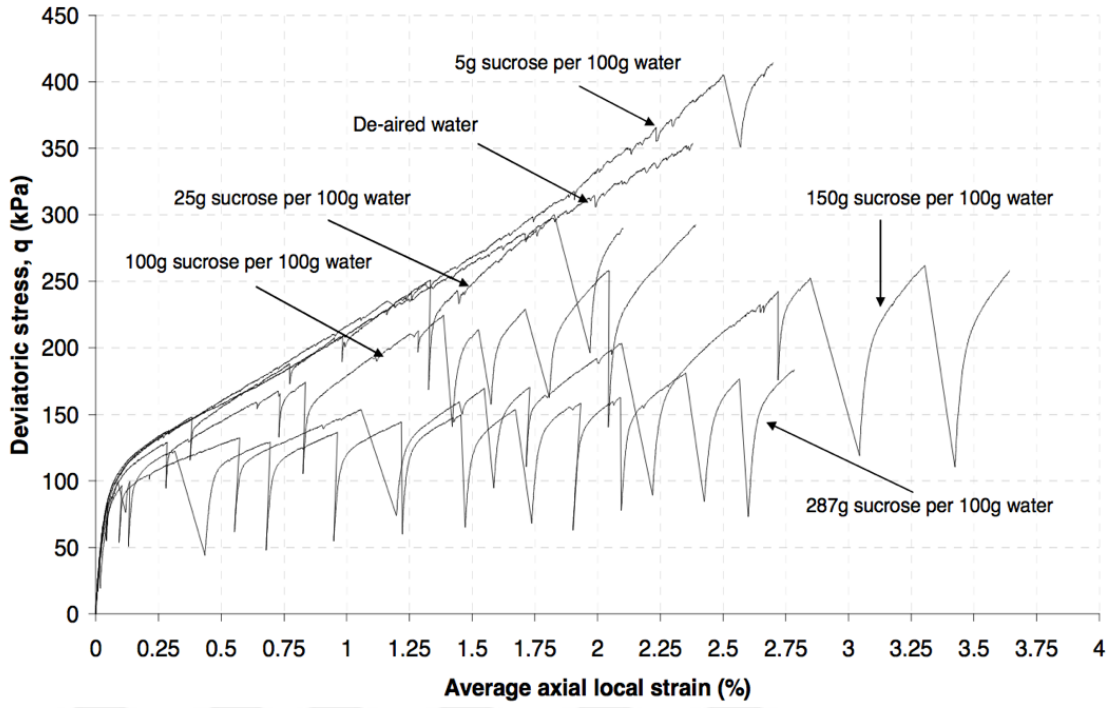

Figure 2.18 Stress-strain curves for clean Leighton Buzzard Sand and that with various pore fluids at 100 kPa effective consolidation (Cabalar and Clayton, 2010).

In Figure 2.18 we see these fluctuations developing, and they are more prominent with the addition of more sucrose. The Gutenberg-Richter (1956) formula that was utilize to provide a relationship between the frequency and the deviatoric stress amplitude, in this investigation is as follows.

$$\log N = a - bM \tag{2.9}$$

In equation 2.9, the constants 'a' and 'b' depend on the observation period, and on the properties of materials.

In conclusion, Çabalar et al. (2010) have shown that these fluctuations might occur due to the rate of loading, effective stress, characteristics of pore fluid, and that testing apparatus could also influence how these fluctuations develop. They investigated sticking and slipping phases individually. They concluded that Gutenberg and Richter law could represent the relationship between the frequency and the fluctuations in deviatoric stress.

2.2.6 Computer Program for Soil Classification

We have developed a simple soil classification program in order to help with the calculations. The program proved to expedite the soil classification procedure. The program is written for Visual BASIC for Applications and works with Microsoft Excel. Figure 2.19 shows an output of a sample data which was entered into the program. The program draws the grain size distributions of the desired soil samples (Figure 2.19) and it is also able to quickly identify soil classification given the parameters. These parameters include the ones related with the sieve analysis results as well as Atterberg limit test results for fine particles. Once these parameters are initially entered into the related fields in the provided sheet of the program, the procedure becomes very straightforward to follow and it allows users to easily see the results.

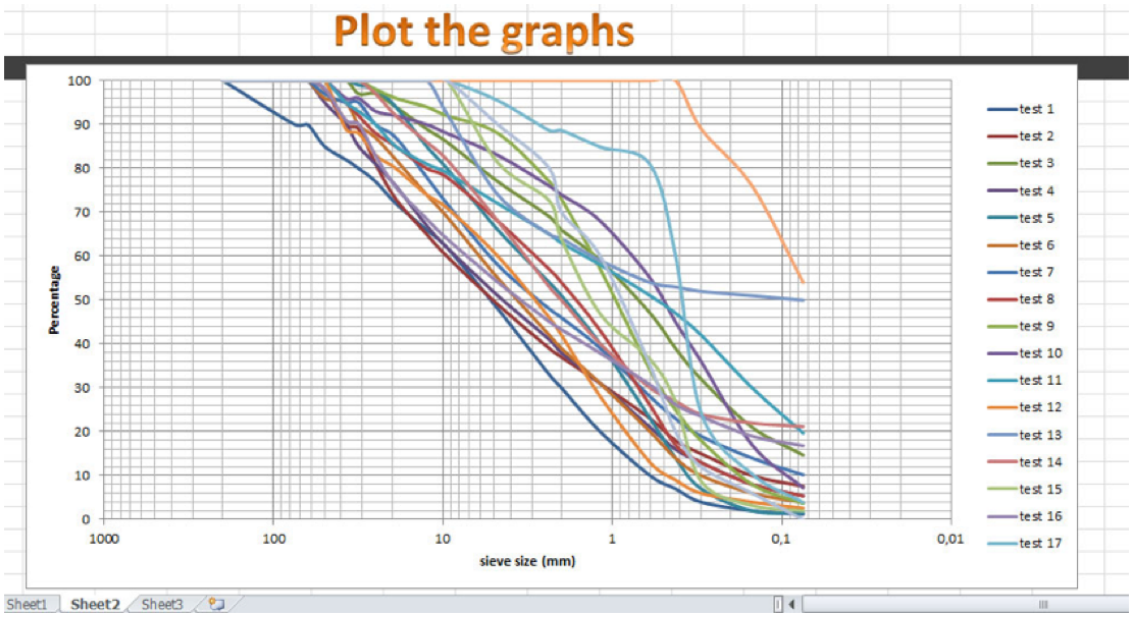

Figure 2.19 An output for the grain size distribution from the soil classification program (Işık, 2014a).

This program was actually a part of a small study that presented computer programs targeted for geotechnical engineering students, which are developed to work with sieve analysis and Standard Penetration Test (SPT) that calculate certain soil parameters. We argue that sieve analysis is a basic step and one that appears in almost all geotechnical engineering experiments including the SPT. And it is known that the process to acquire soil classification necessitates one to go through large amounts of data. Therefore this

computer program will be very helpful in during our works with which we aim to minimize errors, and expedite the laboratory experiments.

The spreadsheet application Microsoft Excel allows the sheets to be programmable by embedding codes within the sheet. The codes can be written in a language called Visual Basic for Applications (VBA) inside the editor. These codes require the Excel sheet in order to work and perform the various functions that can be changed. In order for the program to be able to run, macros have to be enabled in Excel. In the Excel workbook, some of the cells are interactive. The macros are an additional layer that work behind the scenes when the workbook is open. When the workbook is opened, the first section is the user interface that enables the interactivity on the sheets. Some of the constants such as sieve sizes, percentage values, specific density of soil are calculated initially by the program. The workbook is divided into 3 sheets for easy navigation. The functions are separated into these sheets. However, the formulas are not seen on the sheets, they can be accessed and changed through the script editor. The macros use these formulas in order to display the results on the sheets.

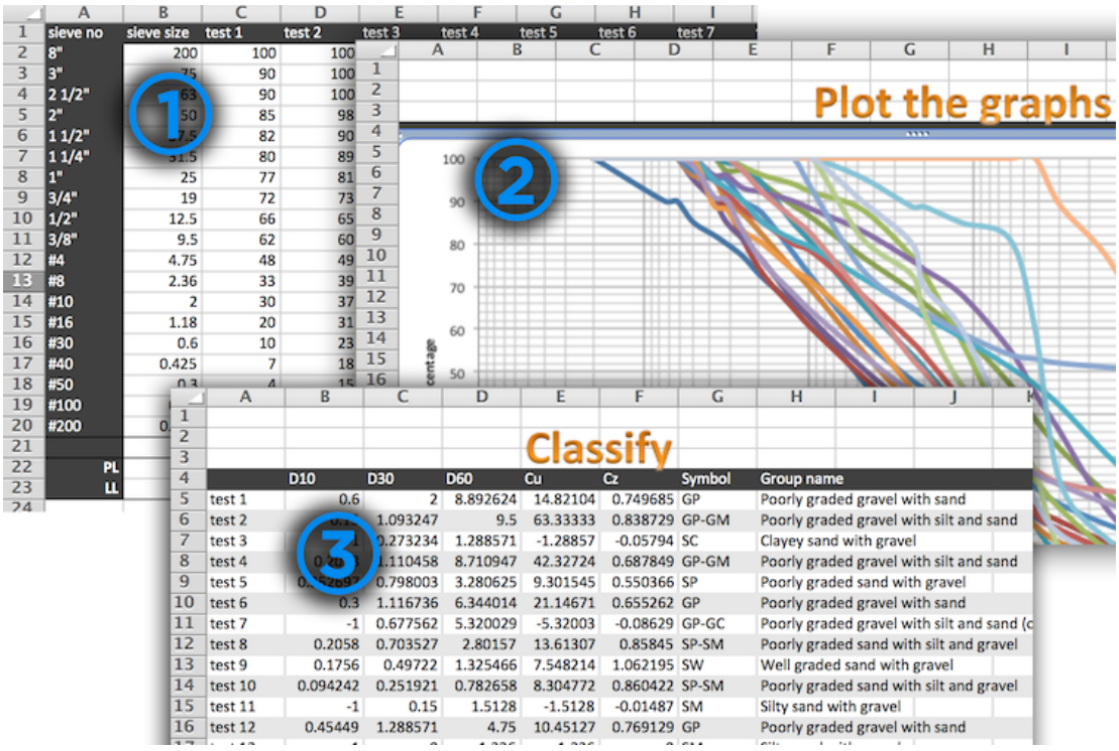

Figure 2.20 A break-down of the soil classification program (Işık, 2014a).

The first sheet is for the first phase of the particle size analysis, where individual sieve sizes can be seen and edited, percentage values can be entered to the corresponding sieve sizes as shown in Figure 2.20. The program also allows multiple test results to be entered on the same sheet separated by columns. Therefore, new columns may be added as needed, which will be automatically processed by the program. Identifying names may be given for the tests in order to differentiate them later during the classification. Results for the Atterberg limit tests can be entered in the same column, which makes the calculations straightforward and easy to follow.

In a geotechnical laboratory, the sieve analysis test is done using a variety of sieve sizes, which change depending on the specific standard. The presence of fine particles of soil require additional tests to be carried out, namely Atterberg limit tests. The user can enter the percentage values in the individual rows without including the percent size. The sieve sizes can be changed in millimeters.

In the sample Excel file (Işık & Cabalar, 2014a) the results of a series of tests are given where the first sheet is prepopulated with the values to be able to test the program. Some of these tests also contain fine particles for which Atterberg limit test results are provided in the respective rows. The parameters for the soil classification for these tests are calculated and provided in Table 3.1. In the second sheet, there is an empty page with a button titled “Plot the Graphs”. When this button is clicked the graphs for all the tests are plotted superimposed one upon another. The final segment of the program is the sheet 3, where the user can see the results of the calculations, symbol names for the samples, as well as their detailed group names. These 3 steps for a sample project of ten tests are illustrated in Figure 2.20. The outputs of the program are shown in Tables 2.4-2.5.

Table 2.4 Parameters obtained in the sample file

	D10	**D30**	**D60**	**Cu**	**Cc**
Test 1	0,600	2,00	8,89	14,8	0,75
Test 2	0,150	1,09	9,5	63,3	0,839
Test 3	-1,00	0,270	1,29	-1,29	-0,05
Test 4	0,210	1,11	8,71	42,3	0,688
Test 5	0,350	0,800	3,28	9,30	0,55
Test 6	0,300	1,12	6,34	21,1	0,655
Test 7	-1,00	0,68	5,32	-5,32	-0,08
Test 8	0,210	0,700	2,8	13,6	0,858
Test 9	0,180	0,500	1,33	7,55	1,062

Table 2.4 (Continued)

Test 10	0,090	0,250	0,78	8,30	0,86
Test 11	-1,00	0,150	1,51	-1,51	-0,01
Test 12	0,450	1,29	4,75	10,4	0,769
Test 13	-1,00	0	1,34	-1,34	0
Test 14	-1,00	0,600	3,20	-3,20	-0,11
Test 15	0,310	0,460	1,84	5,94	0,378
Test 16	-1,00	0,550	7,59	-7,59	-0,04
Test 17	0,140	0,320	0,420	2,95	1,68
Test 18	-1,00	0	0,090	-0,09	0
Test 19	0,250	0,510	1,18	4,74	0,884

Table 2.5 Symbol and group names from the sample file

	Symbol	**Group name**
Test 1	GP	Poorly graded gravel with sand
Test 2	GP-GM	Poorly graded gravel with silt and sand
Test 3	SC	Clayey sand with gravel
Test 4	GP-GM	Poorly graded gravel with silt and sand
Test 5	SP	Poorly graded sand with gravel
Test 6	GP	Poorly graded gravel with sand
Test 7	GP-GC	Poorly graded gravel with silt and sand (or silty clay and sand)
Test 8	SP-SM	Poorly graded sand with silt and gravel
Test 9	SW	Well graded sand with gravel
Test 10	SP-SM	Poorly graded sand with silt and gravel
Test 11	SM	Silty sand with gravel
Test 12	GP	Poorly graded gravel with sand
Test 13	SM	Silty sand with gravel
Test 14	SM	Silty sand with gravel
Test 15	SP	Poorly graded sand with gravel
Test 16	GC	Clayey gravel with sand
Test 17	SP	Poorly graded sand
Test 18	MH	Sandy elastic silt
Test 19	SP	Poorly graded sand with gravel

The sieve analysis program can be broken down into two main components: the component that (i) computes D10, D30 and D60 parameters, and (ii) the one that

generates group symbols and group names. The aim of the program is to reduce the workload when doing a simple soil classification.

In order to find the percent finer parameters (D10, D30 and D60), which indicate grain sizes, we need to look for the percent we are interested in on the x-axis, and find the y-axis component. On a typical grain size distribution graph, we would have a fitting curve passing through the data points. In the program, a Bézier curve is drawn between every data point. Therefore, we can easily find the desired intersection on our grain size distribution curve.

The second main component of the program is the algorithm by which the group symbols and group names are determined for each soil sample. In the algorithm, we first determine what percentage of fines there are in a sample being looked at. In the second step, we examine gravel and sand content of the sample. When there are fine grains above a certain percentage in a sample, the composition of fines is further analyzed using plasticity index and liquid limit parameters.

The algorithms of the program are straightforward which only require basic soil parameters to be known. The program relies on laboratory tests including sieve analysis and Atterberg limit tests. However, they do automate the tasks, which constitute the bulk of the process in both soil classification. Therefore, as well as expediting our laboratory related jobs, we also believe the programs help students of geotechnical engineering to perform more tests and focus on evaluating the results. On the other hand, since our approach still depends on laboratory tests, the quality and precision of the results will depend on the equipment and laboratory conditions.

2.3 Slope Stability Analysis Methods

Many of the engineering designs that are related with soil are found on inclined surfaces and some of them require working with inclined surfaces or slopes. It is necessary for the soil on these slopes to be in an equilibrium condition. In geotechnical engineering, slope stability analysis is conducted to evaluate how stable the soil on inclined surfaces to failure are due to sliding or collapsing.

Slope stability analysis is generally performed by the use of simple limit equilibrium techniques or computational analysis approaches which include finite element limit analysis and discontinuity layout optimization. There are even numerical methods that offer more complex solutions. The numerical methods can be categorized into three groups according to what modeling scheme they employ: (1) Continuum, (2) Discontinuum, (3) Hybrid.

The numerical techniques and applications that use continuum modeling generates a mesh from a given slope, and uses finite difference and finite element methods to discretize the soil mass into finite number of elements.

Discontinuum Modeling is more suitable for analyzing the behavior of rock/soil mixed slopes or aggregation of jointed distinct rock masses. In this kind of modeling, every single aggregate is treated individually where each particle or block is assumed to be subjected to external loads and that they can undergo displacements. Discontinuum methods also referred to as the Discrete Element Method (DEM). There are variations of this method among which include (1) Distinct Element Method, (2) Discontinuous Deformation Analysis, and (3) Particle Flow Codes.

There are also traditional methods of analysis and they use limit equilibrium methods.

2.3.1 Limit Equilibrium Methods

The LEM constitute the methods that have been used traditionally, which are the equations used in analyzing slope stability and are based on static equilibrium of forces and moments. The LEM is usually preferred because of its simplicity and the ease of application in the complex geometry slopes. The method is based on dividing the soil mass into slices, determining the forces acting on the individual slices, and solving the corresponding equilibrium equations. The factor of safety (FS) is calculated as a result of the equations, which can be defined as the ratio of the resisting forces or the shear capacity of the soil to the shear stress at the moment of failure. Numerous equilibrium methods have been devised for the analysis. Fellenius (1927) introduced the first method based on the assumption that the slip surface is round, which is called the Ordinary Method or the Swedish Method. This method ignored the normal and shear forces acting on the slices. Bishop (1955) developed this method further by introducing the normal forces present on the slices. The normal forces at the base of each slice is calculated by adding all the forces in the vertical direction. The normal force *N* is expressed as a function of the factor of safety and is calculated as shown in Equation 1.

$$N = \left[\frac{c'L\sin\alpha - uL\sin\alpha\tan\phi'}{F}\right] / \left[\cos\alpha + \frac{\sin\alpha\tan\phi'}{F}\right] \qquad (2.10)$$

In Equation 2.10, c' represents cohesion, u represents base pore water pressure, L represents base length, and F represents the factor of safety. As can be seen from the equation, the calculation for the factor of safety becomes non-linear. Janbu (1968) presented another method, in which assumed that the failure slope does not follow a circurlar path. Thereafter, several other researchers developed different methods each with slightly different assumptions for the slope stability system in question (Morgenstern-Price 1965, Spencer 1967, Sarma 1973).

The most commonly used LE methods are as follows:

(4) The Swedish Circle Method (also known as the Fellenius Method, or the Conventional Method)

(5) Bishop's Simplified Method

(6) The Spencer Method

(7) The Janbu Methods

(8) The Corps of Engineers Method

(9) General Limit Equilibrium Method (or the Morgenstern-Price Method)

Each of the limit equilibrium methods have 4 common aspects. (Duncan and Wright, 1980) They are:

(1) All of them use the same definition of Factor of Safety, which is as follows:

$$F = \frac{s}{\tau}$$

where s is shear strength of soil and τ is shear stress required for equilibrium.

(2) They all make the assumption that the strength parameters are not affected by the stress-strain behavior.

(3) They calculate normal stress on the base of each slice. It is found by the following equation:

$$s = c + \sigma_n + \tan\phi$$

where σ_n is the normal stress acting on the base of a slice, c is the coefficient of cohesion and ϕ is the angle of internal friction.

(4) The forces involved in equilibrium methods are statically indeterminate, therefore all methods employ assumptions to make up the balance between the number of equilibrium equations and the number of unknowns in the problem.

Table 2.6 describes forces equilibrium methods (e.g., Lowe and karafiath 1960; U.S.Army Corps of Engineers, 1970). This applies to any shape of slip surfaces and satisfies both horizontal and vertical force equilibrium. However this method does not consider moment equilibrium. Another method for slope stability analysis, for example Bishop's modified method (Bishop, 1955) doesn't satisfy horizontal force equilibrium and applies only for circular slip surfaces.

Table 2.6 Characteristics of Slope Stability Analysis (Duncan and Wright, 1980)

Method	**Characteristics**
Slope Stability Charts (Janbu 1968; Duncan et al, 1987)	Accurate enough for many purposes Faster than detailed computer analyses
Ordinary Method of Slices (Fellenius, 1927)	1. Only for circular slip surfaces 2. Satisfies moment equilibrium 3. Does not satisfy horizontal or vertical force equilibrium

Table 2.6 (Continued)

Bishop's Modified Method (Bishop, 1955)	1. Only for circular slip surfaces 2. Satisfies moment equilibrium 3. Satisfies vertical force equilibrium 4. Doesn't satisfy horizontal force equilibrium
Bishop's Modified Method (Bishop, 1955)	1. Only for circular slip surfaces 2. Satisfies moment equilibrium 3. Satisfies vertical force equilibrium 4. Doesn't satisfy horizontal force equilibrium
Forces equilibrium method (e.g. Lowe and Karafiath 1960; U.S.Army corps of Engineer, 1970)	1. Any shape of slip surfaces 2. Don't satisfy moment equilibrium 3. Satisfies both horizontal and vertical force equilibrium
Janbu's Generalized Procedure of Slices (Janbu, 1968)	1. Any shape of slip surfaces 2. Satisfies all condition of equilibrium 3. Permits side force locations to be varied 4. More frequent numerical problems than some other methods
Morgenstern and prices Method (Morgenstern & Price, 1965)	1. Any shape of slip surfaces 2. Satisfies all condition of equilibrium 3. Permits side force orientations to be varied
Spencer's Method (Spencer, 1967)	1. Any shape of slip surfaces 2. Satisfies all conditions of equilibrium 3. Permits side force locations to be varied

2.3.1.1 The Swedish Circle Method

The cross-sectional area of the sliding mass is partitioned into equal width slices. As can be seen in Figure 2.21, vertical and horizontal forces exist on each slice, and they can be found through the moment and force equilibrium.

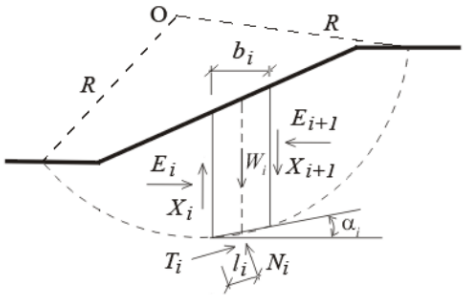

Figure 2.21 The Swedish Circle Method.

2.3.1.2 Bishop's Simplified Method

The Simplified (or Modified) Bishop's Method which was named after Alan W. Bishop of Imperial College, is an improvement over the Swedish Circle Method. The method makes the problem of stability of slopes statically determinate and more suitable for calculating by hand. It assumes that the forces acting on either side of the slice are horizontal.

2.3.1.3 The Spencer Method

Another limit equilibrium was proposed by Spencer (1967) which is based on dividing the failure surface into slices. In order for the method to work, the slope has to have a circular slip surface. The failure area is divided into parallel slices within which fixed normal and shear forces act. The slices also form a fixed angle of 9 degrees. This method was later improved by Spencer (1973) where a more reliable FOS is found when parallel inter-slice forces were used. The Spencer method can also be applied for surfaces that have an irregular shape (Wright 1969, Spencer 1973).

Figure 2.22 illustrates the slice forces acting throughout the given cross-sectional area. The factor of safety that does not need be individually calculated for each of the slices, since they are assumed to be all equal just like the previous LE methods. This also means that the failure of each of the slices happen at the same time. Therefore, an inter-slice force is required which will be responsible to carry the load from one slice to another. The angle of inter-slice forces from the horizontal are also fixed at an angle of 9 degrees. A single resultant force can be calculated that can substitute all the inter-slice forces, which is denoted by Q_F. This force acts through the center point of the bottom side of the slice and makes an angle of 6 with the horizontal.

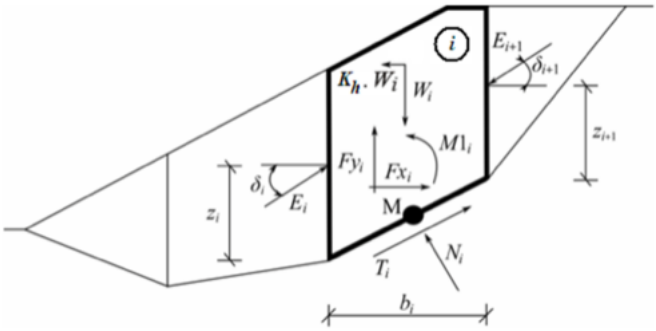

Figure 2.22 The Spencer Method.

2.3.1.4 Janbu's Direct Method

Janbu direct method (JDM) is constructed using slope stability charts, which utilizes dimensionless coefficients in order to calculate slope stability (Janbu 1954a). Since the method is based on chart, it becomes a relatively easy and an efficient method to carry out simple slope stability tasks, which can even have complicated features such as groundwater, cracks of tension, or surcharge. Effective stress as well as total stress analysis can be done using this method.

The FOS for cohesive soils such as clays are given by the following equation (Janbu, 1954a, 1996):

$$F = N_{cf}\frac{c}{p_d},\ \lambda_{c\phi} = \frac{p_e}{c}\tan\phi \text{ and } p_e = (1-r_u)p_d \tag{2.11}$$

where,

p_d = total stress,
p_e = effective stress,
N_{cf} = stability number computed with a dimensionless factor ($\lambda_{c\phi}$),
$r_u = u/\gamma z$ = pore pressure ratio

Figure 2.23 illustrates a cross section of a slope and its relevant dimensions for the JDM. The method starts by finding the rotation center which is denoted by X_0, Y_0. This is the coordinates for the critical slope circle. The equilibrium of moment of the shape is calculated with respect to this particular coordinate. It can also be given in terms of the angle of slope (β) and a coefficient represented as $\lambda_{c\varphi}$, which can be found in Janbu's slope stability charts. Using this method, the calculation of the FOS for slopes that have circular failure planes can be found efficiently and easily.

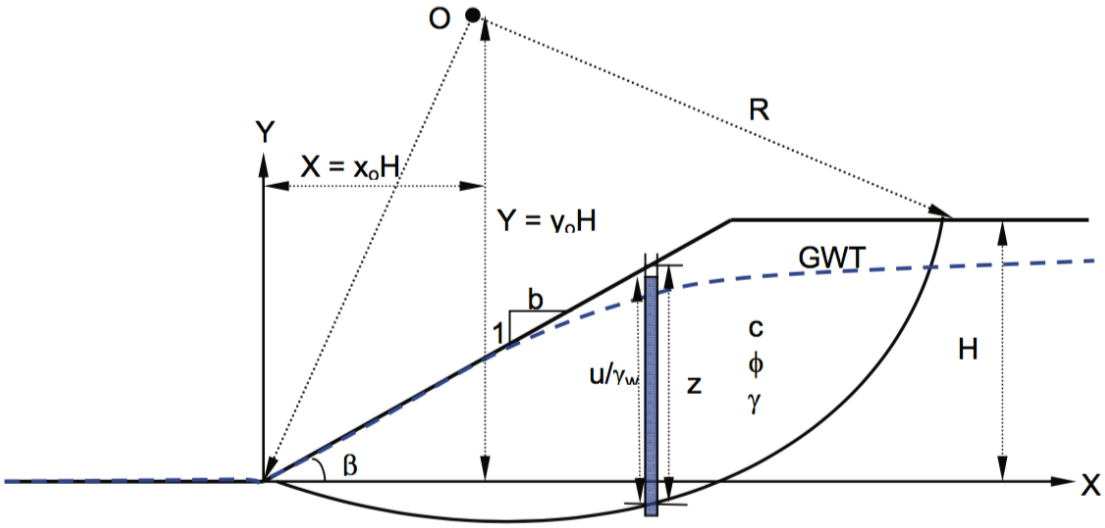

Figure 2.23 Cross section of the slope in calculation of the FOS for JDM.

2.3.1.5 Morgenstern-Price Method

Morgenstern Price Method is a slope stability analysis method that uses limit equilibrium based on dividing the sliding area into slices. The individual slice blocks satisfy the moment and force equilibriums. Each slice above the failure surface is produced by dividing the area into equal portions, where surface forces exist in each of these slices just like in the Spencer method. In order to calculate the forces acting on the slices, a number of assumptions were made, which are given as follows:

(1) The slices are divided vertically

(2) The vector that represents the center of gravity for a given slice passes through its center, which is represented by point M

(3) A slice has its normal force that acts at its center

(4) Each slice has a different inclination of forces that act between them, and at the end of the slip surface this value becomes zero

These assumptions also outline the differences between Spencer and the current method. The choice of inclination angles that are between the slices are calculated using a sine function. Although the choice of the shape for the function may have an effect on the results, this effect is insignificant and if the shape is chosen carefully, it can improve the results.

2.3.1.6 Lowe & Karafiath's Method

Contrary to other methods, Lowe & Karafiath's method (LKM) only satisfies force equilibrium during the calculation of FOS. Just like the methods that originated before it, LKM also makes the assumption that the inclination of the slope surface (β) is equal to the inclination of the inter-slice forces. In this method, inclination of the base of the slice is denoted by α, and the following relationship is given:

$$\theta = 1/2(\beta + \alpha) \tag{2.12}$$

where θ denotes resultant force derived from the inter-slice inclination. Therefore, the inter-slice force equation can be given as the following:

$$T = E \tan\theta \tag{2.13}$$

The LKM method can be summarized as follows

- Both shear and normal forces are considered with respect to the inter-slice forces.
- It only satisfies force equilibrium.
- Makes the assumption that the inclination is equal to inter-slice forces.

2.3.1.7 Corps of Engineers Method

Another method was developed in order to calculate FOS, which was similar to LKM. The Corps of Engineers method (1970) posits that there are two kinds of assumptions that can be made with regards to the inter-slice force resultant angle. The first one is to assume it to be parallel to the surface of the ground. The second one is to assume it to be same as the average slope angle, which can be calculated by considering the first and final points of the critical slope surface.

2.3.1.8 General Limit Equilibrium Method

This method is an improvement of Morgenstern & Price and Spencer methods, while also taking into account some of the other assumptions of previous methods (Krahn 2004, Abramson et al. 2002). A comparison of all the methods can be made using the GLE method as a benchmark, as shown in Figure 4.4. It can be clearly seen where the most probable FOS and moment equilibrium inclinations are particularly if the analysis is for a circular slip surface (Krahn 2004).

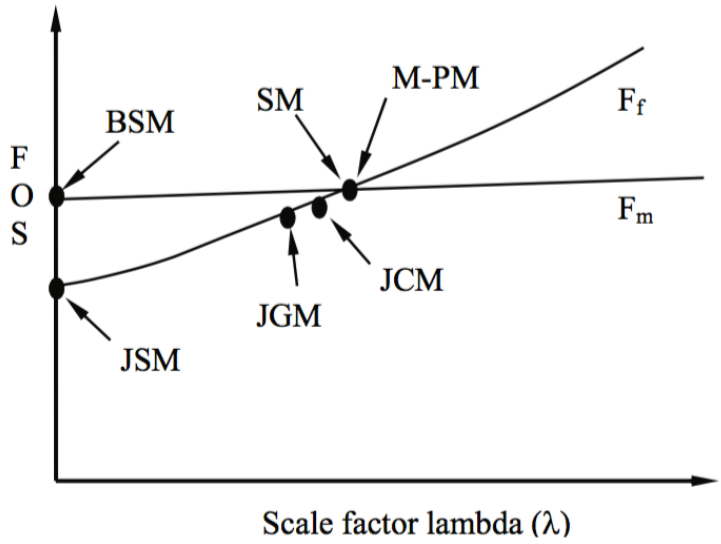

Figure 2.24 The most commonly used slope stability analysis methods compared (Fredlund and Krahn, 1977).

One of the important aspects of the GLE method is that it can compare FOS's using the same diagram. In Figure 2.24, it can be seen that for JSM and BSM the FOS is calculated when the scale factor coefficient (λ) becomes zero. If the graph is followed for MPM or SM, the FOS can be found using the intersection of these two methods. Janbu's general and corrected methods lie somewhere around the intersecting point (Fredlund & Krahn, 1977).

Using this method, it is possible to make slope stability analyses for circular slip surfaces as well as composite ones (Fredlund et al., 1981, Chugh, 1986). GLE method can be summarized as follows:

- Both shear and normal forces are considered with respect to the inter-slice forces.
- Force and moment equilibriums are satisfied in the equations.
- Function for an inter-slice can be selected.
- Easy and efficient comparisons of LE methods can be done

2.3.2 Numerical Methods

Numerical modeling starts by dividing the slope into a finite number of zones or elements. Forces and strains are then calculated for each element using the appropriate constitutive laws for the materials in the slope. The finite element approach is increasingly being used

in the analysis of slope stability problems in geotechnical engineering due of its advantages over the conventional limit equilibrium methods. The main difference between the FEM and the LEM is that FEM utilize constitutive law or stress-strain relationship. In this method, there are generally two approaches to a slope stability analysis. The first one is the gravity increase method, where the gravitational acceleration is increased until the slope becomes unstable and the equilibrium solution no longer exists (Chen and Mizuno, 1990). The second one is the strength reduction method, the shear strength parameters (c and ϕ) of the slope are reduced until the slope collapses and the equilibrium solution no longer exists (Zienkiewicz and Taylor, 1989). In this method, elastoplastic analyses are performed using different shear strength parameters obtained by dividing the actual shear strength parameters by a set of safety numbers. There are many geotechnical engineering software packages available that make the calculations easy. The most common numerical analysis methods available are Finite Difference methods (FDM), Finite Element Methods (FEM), Discrete Element methods (DEM), Boundary Element methods (BEM), and Discrete Fracture Network methods (DFN).

2.3.2.1 Constitutive Model Formulation

This method relies on formulations that uses shear strength equilibrium, hydraulic conductivity function and shear strength reduction. The principal of shear strength reduction technique in finite element analysis is to simultaneously reduce c and tan φ in small increments until failure occurs in the numerical analysis. If shear strength parameters at failure are cr and φr .The factor of safety (F.S.) can be defined as (Indra and Helmut F., 2011)

$$FS = \frac{\tan\phi}{\tan\phi_r} = \frac{c}{c_r} \tag{2.14}$$

2.3.2.2 The Random Finite Element Method

The Random Finite Element Method (RFEM) that combines random field theory with deterministic finite element analysis was developed by Griffiths and Fenton in the early 1990's and has been applied to a wide range of geotechnical applications. In a stability analysis, input to RFEM is provided in the form of the mean, standard deviation and spatial correlation length of the soil strength parameters at the point level, which may consist of several layers with different statistical input parameters. In the absence of site

specific information, there is an increasing number of publications presenting typical ranges for thestandard deviation of familiar soil properties, e.g. Lee et al.

In RFEM, local averaging is fully accounted for at the element level indicating that the mean and standard deviation of the soil properties are statistically consistent with the mesh density. Since the finite element method of slope stability allows mechanisms to seek out the most critical path through the soil, the methodoffers great promise for more realistic reliability assessment of slopes and other geotechnical applications. (Griffiths and Fenton 2000).

2.3.3 Computer Programs Developed/Used for Stability Analysis

Recent advancements in computer and software technologies provide geotechnical engineers with powerful and fast computing tools. The Shear Strength Reduction (SSR) technique, which is employed in many computer software programs for slope stability analysis, is used to calculate factors of safety for slopes. With the method, it is possible to predict stresses and deformations of support elements, such as piles, anchors and geotextiles, at failure. Aside from the advantage of computer programs' capability of being fast and accurate, they also present the failure mechanisms visually, which helps to evaluate slopes in a more realistic fashion.

For the purpose of this thesis both limit equilibrium methods and numerical methods will be tested and compared using computer programs. Although limit equilibrium methods are not intended to be used with the help of a computer, we developed a special program in order to quickly and efficiently compare and present the results from both methods.

2.3.3.1 The SlopeH Software

SlopeH is a software we developed using Visual Basic for Applications, which is embedded in Microsoft Excel. Therefore, it can be used with the convenience of the popular spreadsheet program.

2.3.3.2 The PLAXIS Software

PLAXIS is a software program developed in 2004 by the joint cooperation of universities in the Netherlands and Norway, and it is owned by PLAXIS B.V. Company (PLAXIS 2004). It is programmed in such a way to be able to solve a variety of problems regarding geotechnical engineering, which includes slope stability, and calculations for steady state groundwater. The program also includes some important finite element analysis methods

and the graphical interface is divided into four sections. The four sections of the graphical interface are inputs, outputs, calculations, and plots of curves. In the curve plot section, the graphs of FOS vs displacements can be generated.

The soil layers were setup using the basic soil properties for a sand sample. In order to generate the finite element mesh, a plane strain model was used, which was chosen to be of triangular element with 15 nods. In addition to this, undrained conditions were also tested, using steady-state groundwater calculations in order to generate the pore water distributions. For all the slope stability analyses, the selected material model was Mohr-Coulomb.

The Mohr-Coulomb model that was selected in this software is applicable for the perfectly plastic assumption of soil mechanics. Therefore, this model utilizes the elastic parameters, as well as the plastic parameters. In addition to its yield function, this model also has a potential function based on the plastic theory, where the angle of dilation is related with the plastic nature of soil. 6 yield functions and 6 plastic functions are given in order to formulate the soil according to this particular model.

2.3.3.3 Visual Slope V 6.0

Visual Slope uses convenient drawing procedures similar to AutoCAD to help users establish analytical models, which allows a detailed and accurate modeling of a complicated project. Visual Slope also includes a database that allows users to easily store and reuse commonly used material properties. No matter how complicated the problem is (such as one that involves different design modules), Visual Slope only uses one simple input file, which makes communication among the users much easier. .

2.4 Correlating Soil Properties by Standard Penetration Test

Standard Penetration Test (SPT) is a geotechnical test that is widely accepted for measuring soil properties. Its experiment procedures are given in ASTM D1586 standard, as well as BS EN ISO 22476-3 and AS 1289.6.3.1. The procedure begins with an open-ended tube, which usually has a diameter of 5 cm that is being blown into the soil. The tube is penetrated into the ground by using a hammer that weighs 140 pounds. The tube is inserted in 6-inch layers. The resistance of the soil that is called the N-value is defined as the number of blows it takes to drive the tube through one of the layers. After the completion of a layer, the soil sample is taken out and classification procedure is started. For each layer the same process is repeated.

The resistance of the soil has a more direct relationship with the relative density of the soil, rather than any other soil property. There have been many formulas devised that can correlate some of the soil parameters by using the N-values. Many factors contribute to these blow counts or the N-values, therefore they have to be taken into account. There are certain multipliers in order to arrive at the N_{60} value.

$$N_{60} = N_{field} C_E C_N C_B C_S C_A C_{BY} C_C \tag{2.15}$$

In Equation 2.15, N_{60} represents 60% of the hammer energy that is being transferred. N_{field} signified the unmodified blow count that was measured in the field. The other terms are the correction factors, which are factor for energy, rod length, diameter of the borehole, hammer cap, hammer blow frequency, and hammer cushion, respectively.

In most of the correlation formulas N_{60} value was used. In the literature there are also calculations that use a different value of N, however in the present study the correlations were calculated by using the N_{60} values. Soil shape, internal friction angle and N60 can be calculated by just measuring the corrected blow count.

Table 2.7. Relationships between SPT-N and internal friction angle (McGregor and Duncan, 1998).

Soil type	Φ' (°)	Reference
Angular and well graded	(12N60) 0.5 + 25	Dunham (1954)
Rounded and well graded, or angular and uniformly graded	(12N60) 0.5 + 20	Dunham (1954)
Rounded and uniformly graded	(12N60) 0.5 + 15	Dunham (1954)
Sandy	(12N60) 0.5 + 15	Ohsaki et al. (1959)
Coarse	3.5(N60) 0.5 + 20	Muromachi et al. (1974)
Sandy	(15N60) 0.5 + 15 > 45 (N>5)	Japan Road Association (1990)
Sandy	(20N1,60) 0.5 + 20	Hatakana and Uchida (1996)

Several formulas for correlation for the internal friction angle were presented in Table 2.7. The last formula utilizes a different N type that is shown as $N_{1,60}$. This means an N value that is normalized by an equivalent geological pressure of 100 kPa, which can be calculated by using Liao and Whitman's (Liao, S. S. C., Whitman R. V., 1986) equation.

One reason why SPT has become a popular field test is that it can also be used to estimate the liquefaction potential of soils. Rauch (1997) presented a Fortran application that can estimate the liquefaction resistance of a soil deposit by interpreting the SPT blow counts. He came up with a formula that can measure the cyclic resistance ratio.

$$100CRR_{M=7.5} = \frac{95}{34 - (N_1)_{60}} + \frac{(N_1)_{60}}{1.3} + \frac{1}{2} \tag{2.16}$$

In Equation 2.16, the cyclic resistance ratio is referred to by CRR. Its subscript is "M=7.5", which signifies that this particular formula is calculating the CRR for a magnitude 7.5 earthquake. Different values can be used in place of this by multiplying it by a scaling factor.

Zekkos (2001, 2004) also wrote a computer program based on SPT correlations, which can be used to design shallow foundations. The design used in the program makes use of the statistical method created by Burland and Burbdige (1984).

2.4.1 Computation of Correlation Formulas

Several factors contribute to the calculation of the correlation formulas, which are the soil type in the experiment, and the other factors related with the specific equipment that is being used. The type of the soil is determined by taking the sample that is obtained from each of the 6-inch layers. In order to classify the soil, the previously defined computer method was utilized. Algorithm of the computer applications for the SPT were analyzed and they were developed for 2 platforms: (i) For Visual BASIC for Applications in Microsoft Excel, and (ii) Objective-C for the iOS platform.

2.4.2 The Program in VBA in Microsoft Excel

The Excel program for SPT correlation have similarities with the sieve analysis program, which also is divided into two sheets for user input and the output sheet for displaying the calculations. Multiple columns were used to represent different tests in order to simultaneously calculate and present the related values. More tests can be added or removed. Likewise, layers can also be added or removed depending on the kind of experiment being done. The dark colored rows present the type of information to be given related with the corresponding column. In each of the cells the information can be entered or left empty, depending on how relevant it is for the current calculation.

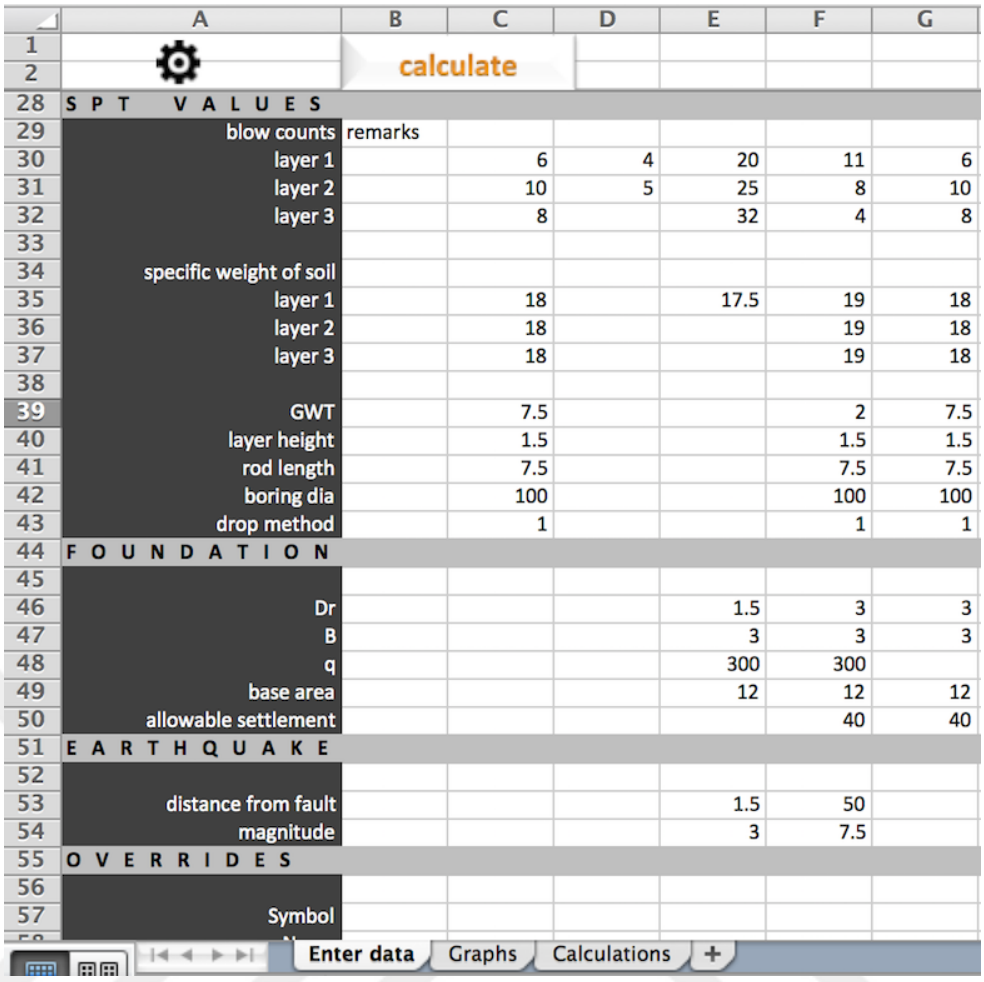

Figure 2.25 User interface of the SPT correlation analysis program in Excel

A sample sheet and its usage are demonstrated in Figure 2.25. In this figure, there is a button which is assigned to a code that estimates several soil properties using the inputs given by the user. These calculations are then displayed on the second sheet in the Excel workbook. The program can also calculate these values using the formulas developed by different researchers. Any of the formulas can be chosen in order to display as can be seen in Figure 3. For instance, the setting for the shear wave velocity could be changed, and a different formula by another researcher can be chosen for comparison. In the Excel program, the results can be seen with the sample data. The code that does SPT correlations are outlined by Pseudo-code 2.1

begin

<1> Declare a variable type to hold the properties

<2> Define constants of g and atmospheric pressure

<3> Read inputs

<4> Find corrected N-values from CE, CB and CR constants

<5> Calculate soil properties using chosen formulas

<6> Display results

end

Pseudo-code 2.1. Main steps of the program (Işık, H., 2014c).

2.4.3 The Mobile Application: SPT Rocks

The Mobile application developed for the SPT correlation (Işık, H., 2014c). uses the same algorithm, which was previously discussed, and it is adopted for the current platform. It is more user friendly, which has a graphical user interface designed to make the inputs straightforward. This makes the program easier to use and faster to provide results. This program has also a separate functionality, it is able to plot the SPT graphs and give graphical representation of the changes of the soil properties within each of the layers. Figure 2.26 presents the data entering procedure of the program.

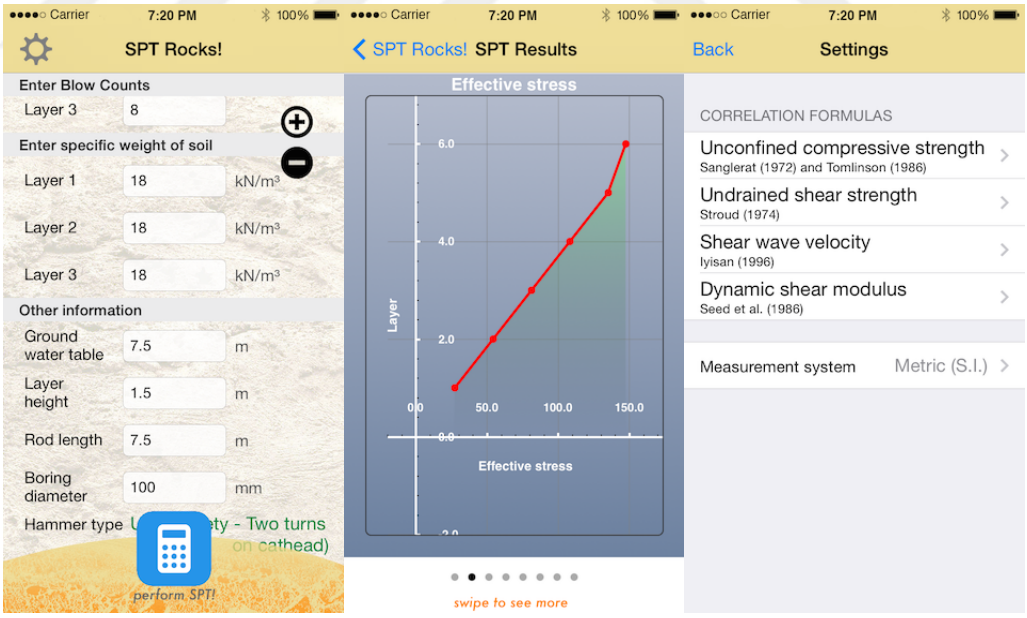

Figure 2.26 User interface of the SPT correlation analysis program on the mobile platform

The algorithm and the steps taken to implement the code into the program is outlined in Pseudo-code 2.2. This program is developed in an object-oriented language; therefore, it uses classes in order to calculate the SPT correlations.

<1> Get the inputs entered by the user

<2> Declare a designated array for the stress variable to

perform iterations on it

<3> Begin loop for each layer

<4> Calculate stresses and effective stresses

<4> Calculate the correction coefficients and corrected

N values

<4> Correlate the soil properties using chosen formulas

<5> End loop

<6> Return results

Pseudo-code 2.2. Pseudo-code demonstrating how the program (Işık, H., 2014b) computes SPT correlations.

CHAPTER III

MATERIALS AND EXPERIMENTAL STUDY

The materials used in this study are 2 different types of natural and manufactured sands, During the slope stability experiments, Round River Sand (RRS), Angular Crushed Sand (AGS) were used. These sands were used in both uniform and well-graded gradations to be able to see the effect of gradation. 45% relative density were chosen for both samples in the experiments. The uniform samples were prepared by sieving each type of sand uniformly within 25-31 mm size range. This chapter presents the details of a series of comprehensive laboratory tests to investigate the effect of various shapes and sizes of sands on the stability of slopes. The chapter also gives detailed explanation of the shape analysis that was carried out and a computer application that was developed to assess shape and size characteristics of soil. Furthermore, a basic design, construction, and characterization of a large-scale slope-box model and the remote data logging system is presented.

3.1 Material Properties

3.1.1 Round River Sand

RRS is a naturally found river sand which was collected from Aksu River in southern part of Turkey. It is commercially available and was supplied from a mining company in the southern region of Turkey. The specific gravity (Gs) of the RRS samples were 2.65.

3.1.2 Angular Crushed Sand

ACS is a commonly found sand used in highways and roads, which is also referred to as chalk rubble, which is commercially available and was supplied from a mining company in the southern region of Turkey. The specific gravity (Gs) of the ACS samples were 2.1.

Particle size distribution graphs were obtained after the sieve analysis procedure and the results were shown in Table 3.1. The relative densities of the samples were calculated to

be 45% for each of them, and they were also confirmed during the large-scale soil box experiments in the laboratory. All of the experimental studies were conducted with the dry sand conditions.

Table 3.1 Properties of the sands used in the experimental program

Experiment no	Sand type	Relative density	Gradation
1	Rounded river sand	45%	Well graded
2	Angular crushed sand	45%	Well graded
3	Rounded river sand	45%	Poor graded
4	Angular crushed sand	45%	Poor graded

4 experiments were carried out with sands with the properties shown in Table 3.1. The void ratios of these sands are shown in Table 3.2.

Table 3.2 The void ratios of the sands used in the experimental program

Sand type	State	emax	emin
Rounded river sand	Loose	0.23	0.16
Rounded river sand	Compact	0.672	0.498
Angular crushed sand	Loose	0.91	0.963
Angular crushed sand	Compact	0.552	0.687

3.2 Evaluation of index properties

The first set of tests are geared towards a complete experimental index analysis. This analysis included relevant tests to evaluate the distribution of grain size, and specific gravity, for the RRS and ACS samples.

3.2.1 Particle size analysis

The procedure of analyzing the size of particles is done through a standard that verifies the outcomes to assess whether they are in compliance with the standard or not. At the end of the analysis a certain gradient distribution is produced which specifies the particles by their size. This data is very useful in determining the properties of soil. The particle size characteristics of the samples used in this study were determined according to the standard test method called ASTM-D422. Sand samples of sizes between 0.075-4.75 mm were subjected to sieve analysis test, while sizes smaller than 0.075 mm were subjected to hydrometer analysis in order to find out the particle size distribution. Figure 3.1-3.2 present the particle size distribution graphs of RRS and ACS samples.

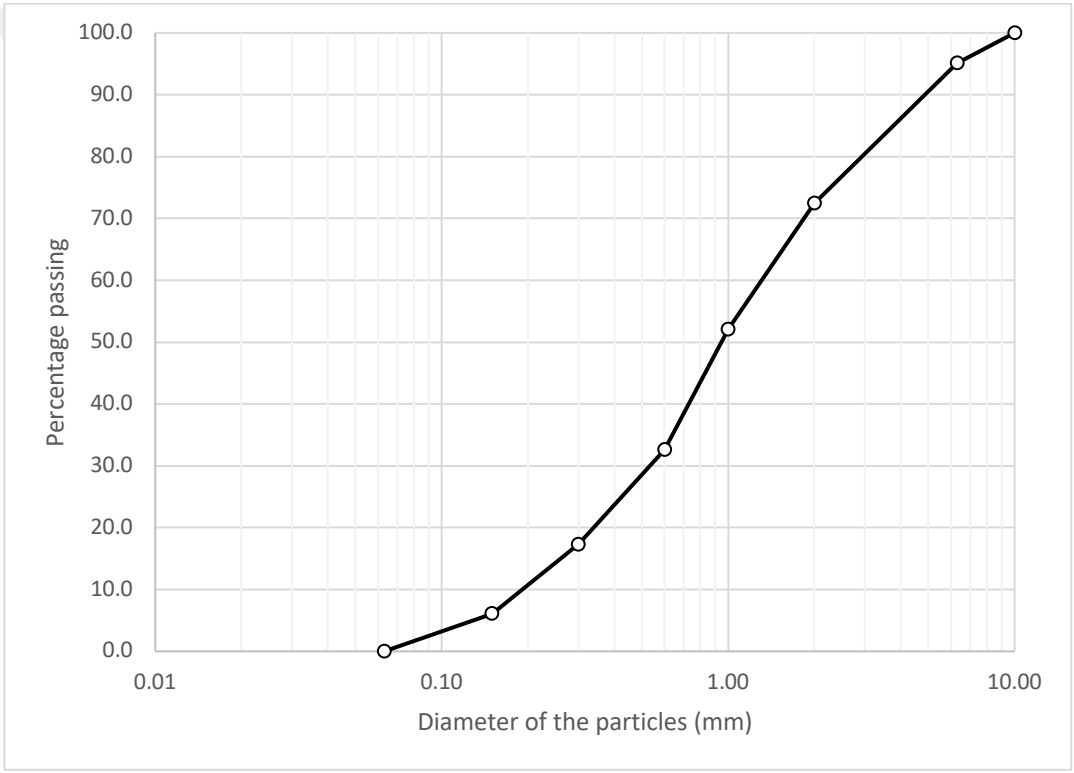

Figure 3.1 RRS sample particle-size distribution curve.

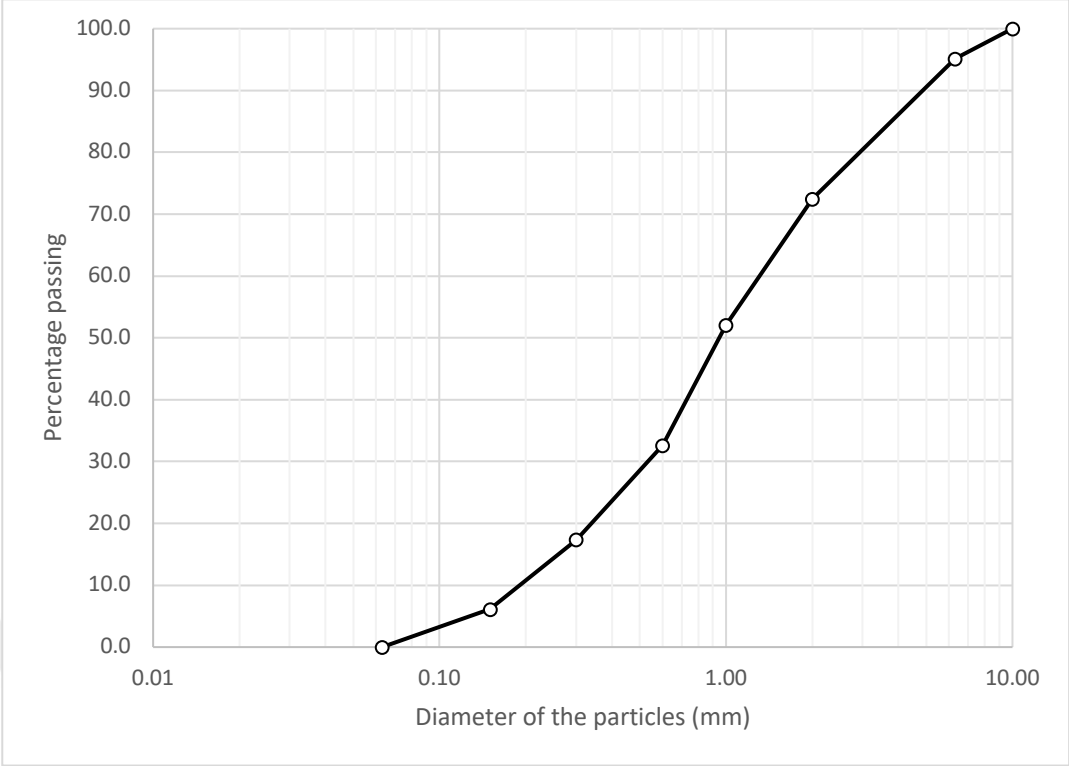

Figure 3.2 ACS sample particle-size distribution curve.

3.2.2 Specific gravity

Specific gravity of a certain material is calculated by taking the ratio of the weight of the material to the weight of water that occupies the same volume. From the perspective of geotechnical engineering, this property makes it possible to determine the void ratio of soil which will be necessary for the particle size distribution analysis. The value of the specific gravity is typically found between the ranges of 2.65 and 2.75 for geological materials (Blight 2010).

The specific gravity values for the RRS and ACS were calculated in the same fashion as explained in ASTM D854 (see Figure 3.7). Table 3.6 shows the specific gravities of RRS, ACS samples used during the experimental study.

3.2.3 Particle Shape Analysis

Particle shape is an inherent soil characteristic that has a significant bearing on strength and packing behavior of soils. Particle shape is examined independent of its size. Mainly two parameters are of importance in this chapter. Those two parameters are sphericity, which gives a numerical value for the overall shape, and roundness, which defines how

round or angular of the edges or corners of a certain particle is. Other morphological features would be roughness and texture, but since they express smaller surface details, they are not within the scope of this study. The parameters of angularity or sphericity, roundness, etc. have always been subjective and not a precise enough definition can be found that can characterize a given particle directly through its shape as the main input. Given that angularity is usually the main factor that plays a role in the packing density of a uniformly distributed soil, a definition for the parameter can be made through this relationship (Mora et al., 2000).

3.2.3.1 Preliminary Analysis of Basic Shapes using ImageJ Software

There are many commercial and open-source image analysis programs available. There are ones that are being developed by the researchers of certain universities to serve their specific needs. There is Icy, an open source bioimage informatics, which is created by the Quantitative Image Analysis Unit at Institut Pasteur, or STatistical IMage ANalyse (STIMAN) software for Windows, developed by soil scientists at Moscow State University. There are also researchers making use of programs and plugins written for engineering software packages like Matlab and Mathematica (Kieran et al., 2013). While they are all powerful alternatives, the software of choice for our analysis is ImageJ, which is a Java-based image processing program developed at the National Institutes of Health.

ImageJ is a public domain program and it is platform independent, meaning that it can run under any machine not being dependent on operating system. Furthermore, because of the way that the program is designed, developers and researchers can implement their

own plugins and macros in order to extend the functionality. The fact that ImageJ is open source makes it possible for others to create their own distributions based off the original program but almost as a completely separate program. In our analyses, we chose Fiji, which comes bundled with plugins specifically related with image analysis and has a comprehensive documentation.

Preliminary particle shape analysis was done with four basic shapes as shown in Figure 3.3.

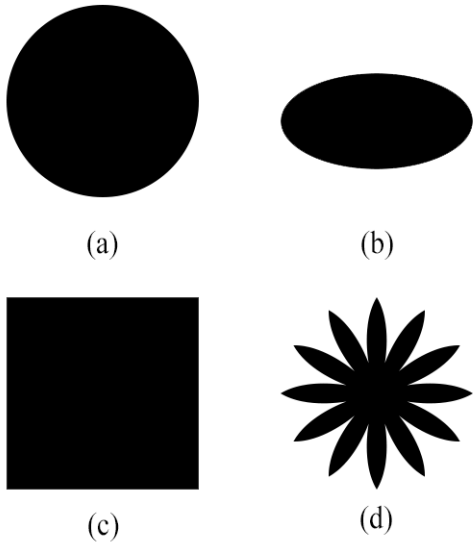

Figure 3.3 Basic shapes used in the preliminary shape analysis a) A1 b) A2 c) A3 d) A4.

These four basic shapes were circle, ellipse, square and a flower shape. They were labeled A1, A2, A3 and A4 respectively. These test images were created in Adobe Photoshop CC 2014.

Table 3.3 Shape analysis results using the four basic shapes

	Area	**Perimeter**	**Width**	**Height**	**Circularity**	**AR**	**Roundness**	**Solidity**
A1	31436	661.169	200	200	0.904	1	1	0.991
A2	15704	508.032	200	100	0.765	1.999	0.5	0.987
A3	40000	797.657	200	200	0.79	1	1	1
A4	16446	1674.871	198	198	0.074	1	1	0.555

Table 3.3 shows the shape analysis results of the four basic shapes. The measurements were made using pixel values, meaning each pixel accounts for a value of 1 in the calculation of width or height.

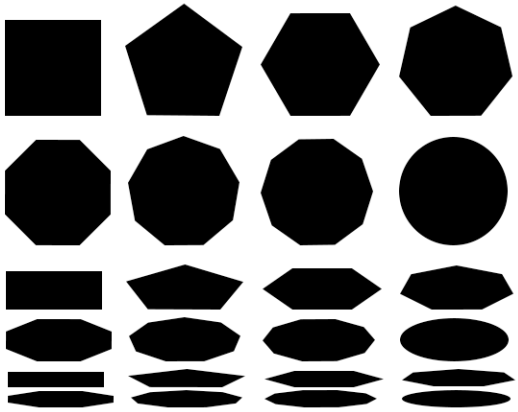

Figure 3.4 Polygons with increasing number of edges and with different aspect ratios.

In Figure 3.4 is shown polygons with increasing edges and ellipses. The figures are composed of 3 sets with varying aspect ratios. Every polygon or ellipse image was let to have approximately the same area to each other. Heights were then calculated according to the given area. The slight differences in the areas are due to the rounding off errors and rather small pixel size chosen for the widths, which is 100 pixels. Shape analysis results for these shapes are shown in Table 3.4.

Table 3.4 Shape analysis results for idealized geometries of various forms shown in Figure 3.2

Shape	Area	Perimeter	Circularity	Roundness	Aspect Ratio
Rectangle	10000	397.657	0.795	1	1
Pentagon	9844	395.404	0.791	0.993	1.007
Hexagon	9942	387.019	0.834	0.997	1.003
Heptagon	10009	385.747	0.845	0.999	1.001

Table 3.4 (Continued)

Octagon	9988	362.676	0.954	1	1
Nonagon	9998	379.161	0.874	0.998	1.002
Decagon	10002	378.09	0.879	0.997	1.003
Ellipse	10025	371.747	0.912	0.999	1.001
Rectangle	4000	277.657	0.652	0.4	2.5
Pentagon	3956	285.622	0.609	0.405	2.468
Hexagon	3998	283.037	0.627	0.401	2.496
Heptagon	3999	282.309	0.631	0.4	2.5
Octagon	3996	274.61	0.666	0.4	2.499
Nonagon	4035	278.894	0.652	0.403	2.484
Decagon	3963	274.551	0.661	0.395	2.53
Ellipse	3983	270.894	0.682	0.399	2.509
Rectangle	1600	229.657	0.381	0.16	6.25
Pentagon	1596	255.154	0.308	0.165	6.077
Hexagon	1578	257.497	0.299	0.159	6.294
Heptagon	1563	246.326	0.324	0.157	6.358
Octagon	1546	239.355	0.339	0.155	6.453
Nonagon	1575	242.326	0.337	0.158	6.336
Decagon	1624	244.326	0.342	0.162	6.178
Ellipse	1594	240.326	0.347	0.161	6.219

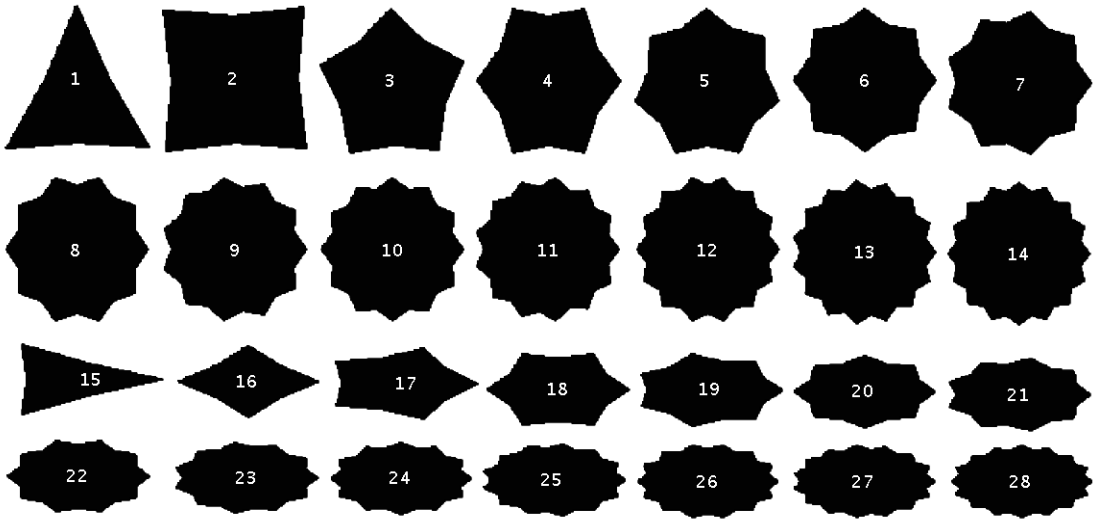

Figure 3.5 Idealized geometries with increasing number of corners.

Another set of example images were generated as shown in Figure 3.5. Figures were numbered 1 through 28. These figures are chosen because they have concave protrusions, which mimic the angular edges and surface features of real life sand particles. We can manipulate the images to our liking, make the indents smoother, or make more indents. The shapes were set to have about same lengths and heights. Therefore, the more indents a shape has, the less angular it is supposed to be, since increasing indents will get smaller in comparison to the overall size and they will act as a "texture" of that shape. The results of shape analysis for the geometries in Figure 3.3 are given in Table 3.5.

In the current implementation of ImageJ software that we are using, there are parameters called circularity and roundness. Circularity is calculated according to the following:

$$4\pi \times \frac{[Area]}{[Perimeter]^2} \tag{3.1}$$

with a value of 1.0 representing a perfect circle. As the value approaches 0, it points to an more elongated shape. It is said in the ImageJ user guide that the values may turn out to be not valid when the particle sizes get very small. The reason for that could be due to pixeallation effect. Since the numerical analysis works with digital images that are represented by pixels, the image can only get so small until the pixels start to interfere with calculations. Therefore, the images need to be at an optimum resolution

in order for the program to work to its fullest capacity. Another parameter that is given by the software is called roundness and its calculated according to the following formula:

$$4 \times \frac{[Area]}{\pi \times [Major\ axis]^2} \tag{3.2}$$

where the term Major axis the longer axis of the best fitting ellipse to the shape.

The roundness definition differs from the conventional one used by geotechnical engineers. Rather than defining how round or smooth a particle is, this parameter gives a ratio of the area of the shape to the area of a circle whose diameter is the major axis of the best fitted ellipse. This means that the parameter will give values close to 1 when the width and height of the image are about the same. When the aspect ratio increases the roundness parameter of ImageJ should decrease.

Figure 3.4 shows a visual chart of roundness and sphericity values. As can be seen in the figure, as the rough corners get smoother the particle is defined to be rounder. It is calculated by dividing the average radius of inscribed circles to the radius of the largest inscribed circle as given by the Equation 3.3.

$$Roundness = \frac{\sum r_i / N}{r_{max-in}} \tag{3.3}$$

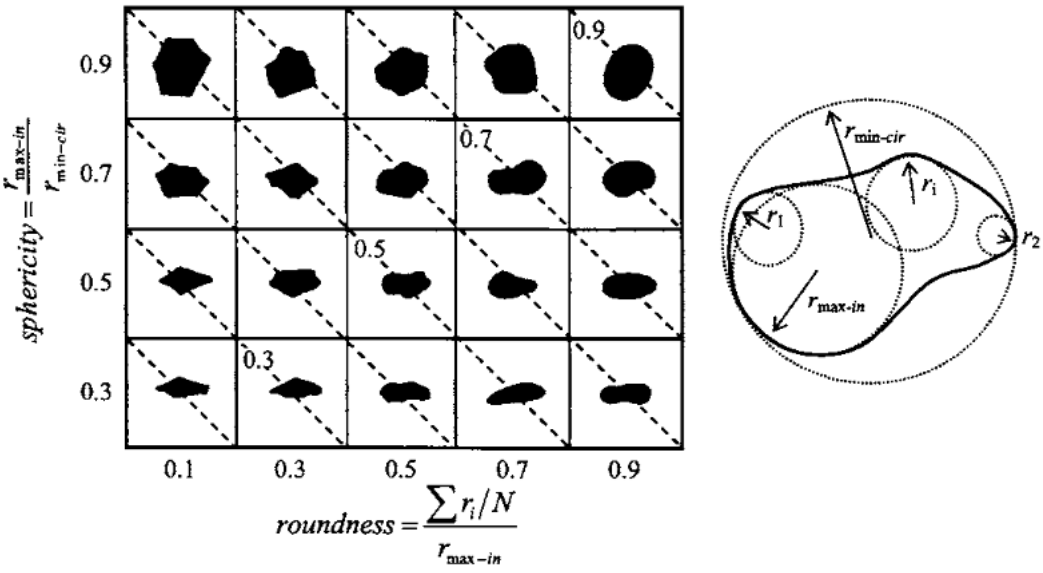

Figure 3.6 Particle shape determination—sphericity *S* and roundness *R* chart (Cho et al., 2005).

The roundness parameter R used in this study is calculated using the equation of Takashimizu and Iiyoshi (2016):

$$R = C_I + (0.913 - C_{AR}) \tag{3.4}$$

where C_I is the circularity calculated using ImageJ software. C_{AR} is the circularity calculation related with the aspect ratio, and it is given by the following formula.

$$\begin{aligned} C_{AR} = {} & 0.826261 + 0.337479 \cdot AR_I - 0.335455 \cdot {AR_I}^2 + 0.103642 \cdot {AR_I}^3 \\ & -0.0155562 \cdot {AR_I}^4 + 0.00114582 \cdot {AR_I}^5 - 0.0000330834 \cdot {AR_I}^6 \end{aligned} \tag{3.5}$$

AR_I is the aspect ratio obtained from ImageJ. It is the ratio of the major and minor axes of the best fitted ellipse of the particle.

Table 3.5 Shape analysis results for idealized geometries of various forms shown in Figure 3.3

	Area	**Major**	**Minor**	**Angle**	**Circularity**	**AR**	**Roundness**	**Solidity**
1	4477	80.828	70.523	89.996	0.486	1.146	0.873	0.886
2	8666	105.042	105.042	32.005	0.66	1	1	0.9

Table 3.5 (Continued)

3	6166	90.504	86.746	90.029	0.7	1.043	0.958	0.889
4	6739	99.371	86.347	89.95	0.704	1.151	0.869	0.891
5	6632	92.978	90.818	89.477	0.743	1.024	0.977	0.895
6	6243	89.173	89.139	90	0.742	1	1	0.892
7	6670	92.91	91.406	178.932	0.737	1.016	0.984	0.894
8	6839	95.561	91.122	90	0.742	1.049	0.954	0.897
9	6772	93.402	92.315	0	0.724	1.012	0.988	0.896
10	6613	91.76	91.76	0	0.724	1	1	0.897
11	6806	93.542	92.64	2.47E-12	0.704	1.01	0.99	0.895
12	6871	94.795	92.288	90	0.698	1.027	0.974	0.895
13	6826	93.382	93.071	0	0.671	1.003	0.997	0.891
14	6754	92.746	92.721	78.141	0.661	1	1	0.898
15	2185	80.45	34.581	0	0.388	2.326	0.43	0.875
16	2228	74.946	37.851	0	0.508	1.98	0.505	0.875
17	3021	90.467	42.518	0	0.569	2.128	0.47	0.88
18	3281	85.442	48.893	0	0.656	1.748	0.572	0.887
19	3280	92.17	45.31	179.965	0.626	2.034	0.492	0.887
20	3148	88.999	45.036	0	0.651	1.976	0.506	0.893
21	3382	92.967	46.318	0	0.639	2.007	0.498	0.895
22	3387	91.118	47.328	0	0.653	1.925	0.519	0.894
23	3350	93.423	45.656	0	0.611	2.046	0.489	0.894
24	3330	91.674	46.25	0	0.629	1.982	0.505	0.89

Table 3.5 (Continued)

25	3448	93.508	46.949	0	0.63	1.992	0.502	0.901
26	3464	92.242	47.814	0	0.627	1.929	0.518	0.897
27	3446	93.296	47.029	0	0.609	1.984	0.504	0.899
28	3416	92.944	46.796	0	0.618	1.986	0.503	0.901

3.2.3.2 Shape Analysis of Sand Particles

Sample images were taken at the Scanning Electron Microscopy facility at the University of Gaziantep. The produced images all have the same resolution. The first step was to scale the images by taking into account their magnification factors. Figure 3.7 shows the images used in this process.

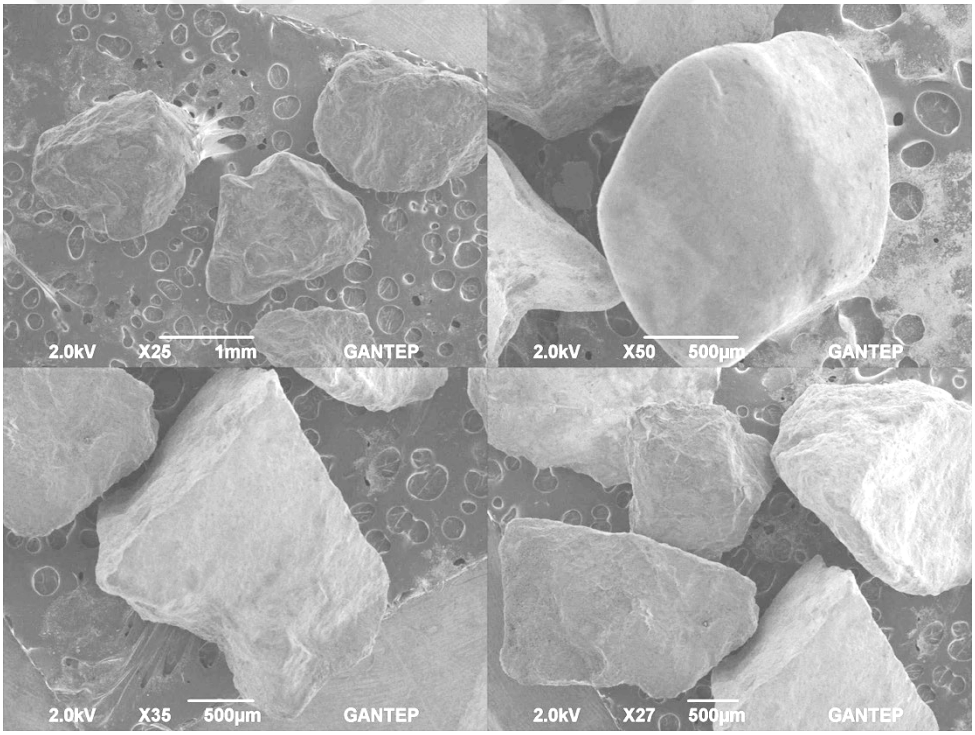

Figure 3.7 SEM images of two types sand particles obtained from Gaziantep.

Next step is to create a binary image of out of these images to be able use them in our image processing software. A binary image is the one where black pixels represent the soil particles and white pixels are background. Figure 3.8 shows the result after this process has been carried out. This image will serve as the basis for shape analysis calculations. In Figure 3.9, the process of finding the maximum inscribed circles for

the calculation of roundness can be seen. The parameters found for the calculations are given in Table 3.6 and Table 3.7.

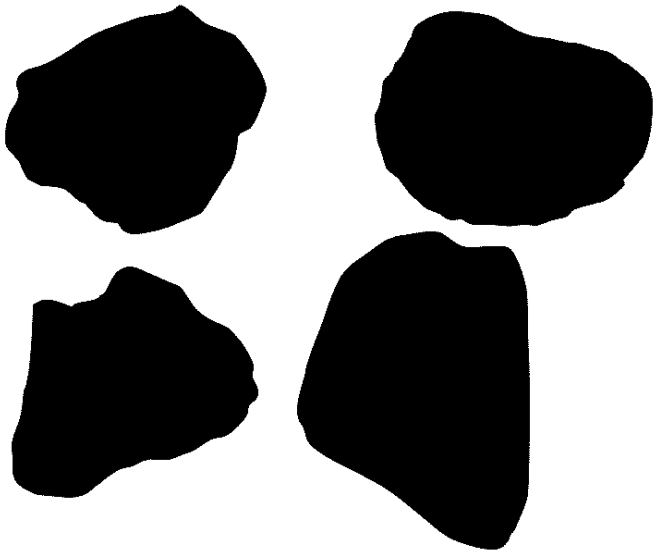

Figure 3.8 Sand particles after being reduced to 8-bit binary form.

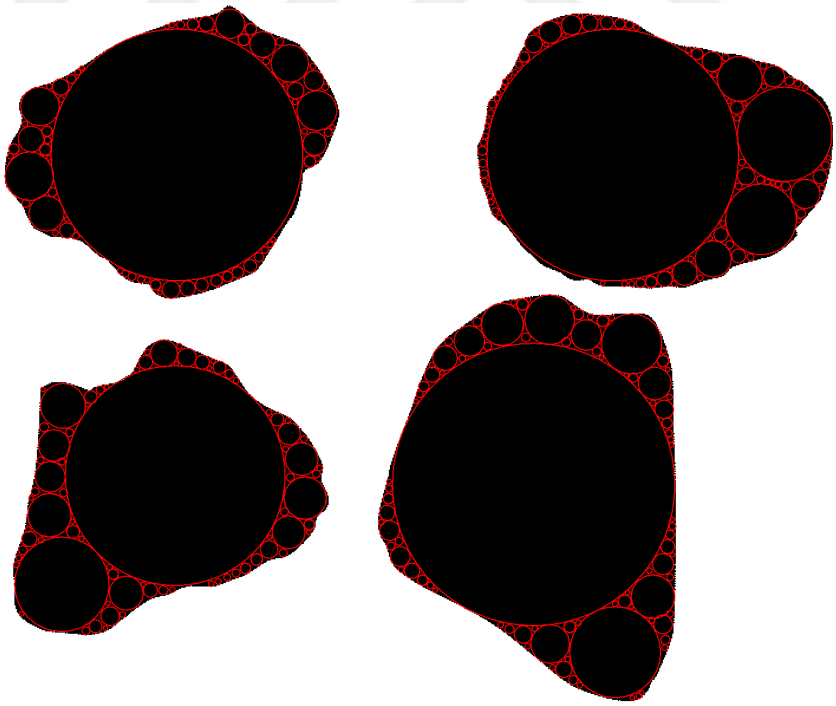

Figure 3.9 Sand particles after being processed to find their maximum inscribed circles.

Table 3.6 Maximum inscribed and minimum circumscribed circle measurements for the sand particles

Sand	Max inscribed circle	Min circumscribed circle
S1	214	290
S2	214	303
S3	187	289
S4	240	357

Table 3.7 Shape analysis results using the sand particles.

	Area	Perimeter	Width	Height	Circularity	AR	Roundness	Solidity
S1	47338	876.389	283	248	0.775	1.234	0.81	0.967
S2	53181	917.418	301	233	0.794	1.351	0.74	0.976
S3	44889	895.377	267	250	0.704	1.303	0.768	0.934
S4	65118	1045.117	252	344	0.749	1.334	0.749	0.979

3.2.3.3 Fourier Shape Analysis of Sand Particles

A convenient way to characterize particle shapes in more detail is by a Fourier mathematical technique. For instance, the *(R, θ)* Fourier method is in the following form

$$R(\theta) = a_0 + \sum_{n=1}^{N} (a_n \cos n\theta + b_n \sin n\theta) \tag{3.6}$$

where *R(θ)* is the radius at angle θ, *N* is the total number of harmonics, *n* is the harmonic number, and *a* and *b* are coefficients giving the magnitude and phase for each harmonic. The lower harmonic numbers give the overall shape; for instance, the sphericity is expressed by the first and second harmonics. The coefficient values for higher-order descriptors generally decay with increasing descriptor or harmonic

number, which expresses smaller features (i.e. texture) (Meloy, 1977). Further discussion on particle shape characterization is given by Barrett (1980), Hawkins (1993), Santamarina et al. (2001), and Bowman et al. (2001).

This method is seen to be utilized in a wide range of disciplines, and in the case of geotechnical engineering it, the focus seems to be the determination of roughness and texture of soils. There is a drawback with the usage of this method which presents itself when the outline of the particle has such features that requires it to be redrawn using the same coordinates. This problem is apparent when the particles have concave features. Another drawback is that there should be a certain precision taken into consideration when calculating the center of this outline, which can get more difficult as the shape assumes more complex features (Bowman et al., 2000).

The way to overcome this problem is through Complex Fourier Analysis or Fourier Descriptor Method. This method makes use of the following equation:

$$x_m + iy_m = \sum_{n=-\frac{N}{2}+1}^{N/2} (a_n + ib_n)\left[\cos\frac{2\pi nm}{M} + i\sin\frac{2\pi nm}{M}\right] \tag{3.7}$$

The radius values for the previously analyzed sand particles were found and plotted in a curvature vs point graph as can be seen in Figure 3.10. The Fourier descriptors were found as shown in Table 3.8, which will be helpful in determining the various properties related with shape.

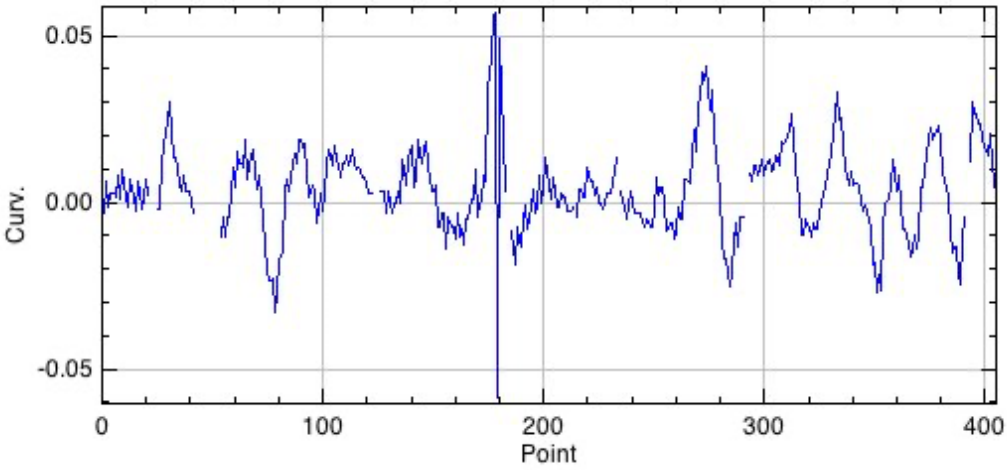

Figure 3.10 Curvature values obtained using Fourier Analysis on sand particles.

Table 3.8 Fourier descriptors for the sand particles

Number of Steps	ax	ay	bx	by
1	302.448	289.079	0.000	0.000
2	5.631	114.604	130.515	-17.747
3	4.297	4.071	-5.244	5.135
4	0.982	-0.661	-4.570	0.151
5	-1.192	2.687	2.487	3.577
6	-2.332	2.631	3.022	-1.374

3.2.3.4 Correlation of Shape Parameters to Soil Properties and Shear Strength

There are a number of laboratory studies that focus on the influence of the particle size on basic soil properties. A variety of studies exist that explain this relationship that soils have in terms of different mechanisms. Many of them focused primarily on two aspects, namely: The contact behavior of particles between each other and the resulting breakage (Santamarina and Cho 2004).

A correlation between sphericity and void ratio was established according to several researchers, which suggested that there is an inverse relationship between the minimum and maximum values of void ratio and sphericity (Holubec and D'Appolonia 1973, Youd 1973, Cho et al. 2006). Sphericity is an important parameter that plays a role in determining the void ratios (Rousé et al. 2008). The researchers also found that maximum void ratio was affected more than the minimum void ratio with respect to sphericity and circularity. This finding suggests that a larger response to the change in the maximum void ratio will be observed as the roundness of the particle is changed. Following empirical relationships were developed by Cho et al. (2006):

$$e_{max} = 1.3 - 0.62R \tag{3.8}$$

$$e_{min} = 0.8 - 0.34R \tag{3.9}$$

$$e_{max} = 1.6 - 0.86Sp \quad (3.10)$$

$$e_{min} = 1.0 - 0.51Sp \quad (3.11)$$

3.3 Development of a Novel Shape Parameter

Estimation of shape parameters have been an interesting topic since there soil particles can be represented and found in a variety of ways, and there have been a number of methods presented by researchers regarding this subject. The shape of soils in terms of micro characteristics is concerned is usually categorized into 3 parameters: (1) sphericity, which is sometimes also called form, (2) angularity or roundness, and (3) roughness or texture (Barrett 1980, Bowman et al., 2001, Sukumaran & Ashmawy, 2001, Santamarina & Cho, 2004). Using these parameters, the soil particles can be defined numerically which can in turn modeled using computer algorithms. Commonly used terms with respect to particle size in geotechnical engineering is form, roundness, and roughness.

One of the terms regarding the particle shape is called form, and it defines the general outline or characteristics of the particle from a broad perspective, which can be given either in 2 dimensions or 3 dimensions. Experimental and theoretical studies have been presented in this topic by numerous researchers (Wadell, 1933; Wadell, 1935; Zing, 1935; Krumbein & Sloss, 1963; Hawkins, 1993; Podczeck, 1997; Sukumaran & Ashmawy, 2001; Hentschel & Page, 2003; Alshibli & Alsaleh, 2004; Cho et al., 2005). One of the interesting methods that was used in the literature is Fourier transform. Wettimuny & Penumadu (2004) used inverse Fourier transformation in order to reconstruct boundaries of sand particles, which they presented as a method to estimate the shape of sand particles. Several other studies were done using 2 dimensional outlines of particles based on Fourier series of lower order harmonics (Ehrlich & Weinberg, 1970; Ehrlich et al., 1980; Clark, 1981; Santamarina et al., 2001) or Fourier descriptor methods (Clark, 1981; Thomas et al., 1995, Bowman et al., 2001). The convenience of the Fourier methods relies on the fact that the outline of the particle can be accurately reproduced mathematically based on the degree of the harmonics.

However, one drawback of this method is that it is usually computationally expensive to extract the shape that defines the particle that is being assessed.

The second parameter is called roundness, which defines irregular features of surface of a particle. The traditional definition given by Wadell (1933) is found by finding the average of corner radiuses and dividing them by the radius of the outlining circle for the particle. One caveat of this definition lies in the fact that the definition of the corners is subjective, which can change the calculations dramatically. To overcome this issue, comparison charts that are designed to visually aid the experimenter have been proposed by different researchers (Powers, 1953; Krumbein & Sloss, 1963; Cho et al., 2005). The disadvantages of using charts to examine the shape is that they will provide slightly different results depending on the person, and that they only provide limited options to choose from. The angularity parameter that was presented by Lee (1964) estimates the roundness better in comparison to Wadell's roundess. However the procedure still depends on defining corners, which makes it have the same weakness as the previous definitions. In order to resolve this issue, an alternative way would be to get rid of corners altogether, in which case Fourier series could be taken advantage of. Nonetheless, the difficulty this time will be extracting certain shape parameters that can be used to perfectly identify the physical behavior of soil. In the recent years there have been an increasing focus on using the method of Fourier transform in order to characterize some aspects of soil and also for shape retrieval, however roundness have not been addressed directly (Thomas et al. 1995, Santamarina & Cho, 2004, Wettimuny & Penumadu, 2004, Tralic et al., 2011, Sayinci et al., 2015, Koo & Kim, 2016, Demir et al., 2019).

The improvement in the image analysis methods meant that shape descriptors can be given more complex definitions in order to produce more efficient models. A formula was put forward by the researchers Yudhbhir and Abedinzadeh, for roundness which considers the count of average tangents, or how many protrusions a particle has along its boundary, and the particle perimeter (Knodel et al., 1991). Sukumaran and Ashmawy (2001) also developed a method, which is based on calculating the differences of the inner angles of the polygon drawn inside the circle with regards to particle outline itself. The researchers also presented their own shape factor denoted by SF, which is based on capturing the differences between the particle outline and

circle with a minimum diameter that surrounds it. Sezer (2008) took advantage of digital imaging techniques in order to evaluate roundness and form of sand particles. In his research, some approximations were made in order to make the calculations. Among these approximation methods were line sections, counting of boxes, and fractal area and perimeter. Roussillon et al. (2009) developed a method that automatically computes pebble roundness with a 92% correlation rate compared to Wadell's roundness. Zheng and Hyrciw (2015) also presented a method in which they computed the values of sphericity and roundness traditionally defined by Wadell. Later, Koestel (2017) developed a computer algorithm that processes X-ray soil images 3-dimensionally.

In this part of the study, the objective is to present a novel shape parameter that accurately and efficiently describes soils based on image analysis and computer methods. Fourier transform was used in order to develop the computer application that is used. The present study is thought to be the first in the literature that takes advantage of Fourier transform for shape generation and definition of a shape parameter. The comparisons to Wadell's original roundness values were made by using the computer method provided by Zheng and Hyrciw (2015). This method was chosen since it presents an algorithm that defines the corners which is an important aspect of Wadell's roundness calculation. The corners were found by taking the outline of the particle shape and dividing it into segments in order to find the maximum divergence through iteration. The value that is called maximum divergence is defined as the maximum differential value between the approximated straight line and the curve in a given segment. Using these values, the beginning and end of a certain corner can be approximated. The advantage of the current study is that it presents the shape factor consistently and it is especially more precise for round particles. The new shape parameter is called Isik Cabalar shape factor and denoted by ICF.

3.3.1 Definitions of Roundness and Sphericity

Wadell (1932) defined roundness as the ratio of the average radius of curvature of the corners of a soil grain to the radius of the maximum inscribed circle as shown in Figure 3.11.

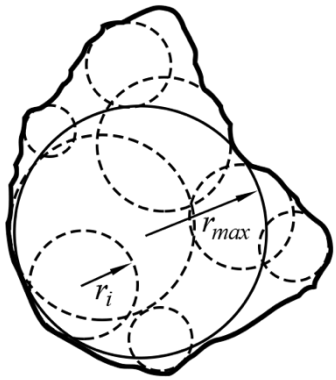

Figure 3.11 Two-dimensional soil grain image showing the radius of the corners (r_i) and the maximum inscribed circle (r_{max}).

Therefore, the Wadell's Roundness (Wadell, 1932) can be described as follows:

$$R = \sum_{i=1}^{N} \frac{r_i}{r_{max}} \tag{3.12}$$

The term r_i in Equation 3.12 is the ith element of the radius of an inscribed circle that is drawn around the corners. The maximum radius for these circles is given by the term r_{max}. This equation represents the most commonly used traditional definition for roundness, which is applicable in a wide range of different disciplines (Eisma, 1965; Edil et al., 1975; Frossard, 1979; Vepraskas, 1987; Sagga, 1993; Sukumaran & Ashmawy, 2011; Chapuis, 2012; Shin & Santamarina, 2013; Kandasami & Murthy, 2014). A new shape parameter denoted as SF was defined (Sukumaran & Ashmawy 2001) which is parallel to the traditional definition of roundness and is calculated using the following equation:

$$SF = \frac{\sum_{i=1}^{N} \left|\alpha_{i,particle}\right|}{\sum_{i=1}^{N} \left|\alpha_{i,flat\ sheet}\right|} \tag{3.13}$$

where difference between the the internal angle measurements of the slices and the circle surrounding them is given by the term $\alpha_{i,particle}$, whereas $\alpha_{i,flat\ sheet}$ represents the angle values for a corresponding flat particle. Another shape factor was also defined in the same study called the angularity factor and represented as AF, which is calculated as follows:

$$AF = \frac{\sum_{i=1}^{N}\left(\beta_{i,particle} - 180\right)^2 - \sum_{i=1}^{N}\left(\beta_{i,circle} - 180\right)^2}{3 \times 180^2 - \sum_{i=1}^{N}\left(\beta_{i,circle} - 180\right)^2} \quad (3.14)$$

Recently there is a growing trend in the soil shape research to use computer algorithms and image processing in order to generate more efficient and consistent ways to describe soil characteristics (Wettimuny & Penumadu, 2004; Tralic et al., 2011; Roussilon et al., 2009, Zheng & Hryciw, 2015; Koestel, 2017). One of the methods taken advantage of with regards to this topic is Fourier transformation, which is also a focus area of the current study. Different than the recent studies, the focus is given to define an overall particle shape factor that characterizes the soils instead of the traditional roundness, which is also comparable to it.

3.3.2 Fourier Transform and Representation of Contours

The first step in the procedure is to obtain the scanning electron microscope images of the samples and transfer them into an image processing program. These images are then converted into monochrome colors by using certain threshold criteria, where the blacks are used for the background, while the whites are used to represent the 2-dimensional version of the individual particles. This way each pixel corresponds to a numerical value that defines the shape in a mathematical form. The contour of the areas can be written mathematically using complex numbers in the sequence of z(n) = x(n) + jy(n) where n can be any number from 0 to N-1 with a contour of N number of points. This computation can be made simpler by using a reference point in order to measure the distances. The reference point can be anywhere on the cross-sectional area of the shape; however, center of mass is chosen in the calculations in order to be consistent as shown in Equation 3.14.

$$\bar{x} = \frac{1}{N}\sum_{n=0}^{N-1} x_n \, , \bar{y} = \frac{1}{N}\sum_{n=0}^{N-1} y_n \quad (3.15)$$

The contour signature of the shape can be given by the following equation.

$$d_n = \sqrt{(x_n - \bar{x})^2 + (y_n - \bar{y})^2} \quad (3.16)$$

which contains important information about the characteristics that the contour such as texture, roughness (Zhang & Lu, 2005). The usage of complex equations prevents the problem of where more than point is represented by the same signature, an issue that was prevalent in concave shapes (Bowman et al., 2001). The average of the contour points is useful in differentiating shapes in a single parameter and is given by the following equation:

$$d_{ave} = \frac{d_n}{N} \tag{3.17}$$

3.3.3 Materials for the Calculations of the Shape Factor

In the calculations for the shape parameter, six types of artificial and natural sands, fly ash pellets and mica were used. The sand samples were prepared in uniformly graded particle size distributions and they are Crushed Stone Sand (CSS), Narli Sand (NS), Thrace Sand (TS), Leigthon Buzzard Sand (LBS), Touyoura Sand (TYS), and Ottawa Sand (OS).

In the southern part of Turkey, around the city of Gaziantep NS was collected around River Aksu. CSS samples were obtained from a commercial company Set/Italcementi Group located in the same area in Turkey. TS sample is a kind of sand that is also found in a river bed which can be found in Thrace region of Turkey, which is located in the north west. Another natural sand sample was LBS, which was obtained from the company David Ball Group, Cambridge, in the UK, conforming to the standard BS 1881-131:1998. The archives of Alshibli (2021) were used for the remaining samples of OS and LBS. OS sample is composed of round sand, which is made up of almost entirely of pure quartz minerals. TYS is also a natural sand, which can be seen in Toyoura area that gives its name, located in Yamaguchi region of Japan. The artificial samples are mica and FAP, which are obtained commercially in Gaziantep. The specific gravity (G_s) of the NS, TS, LBS, OS, and TYS samples were 2.65. The G_s values of CSS, mica, and FAP were 2.68, 2.88, and 2.12 respectively. Figure 3.12 shows the SEM images of the materials that were used.

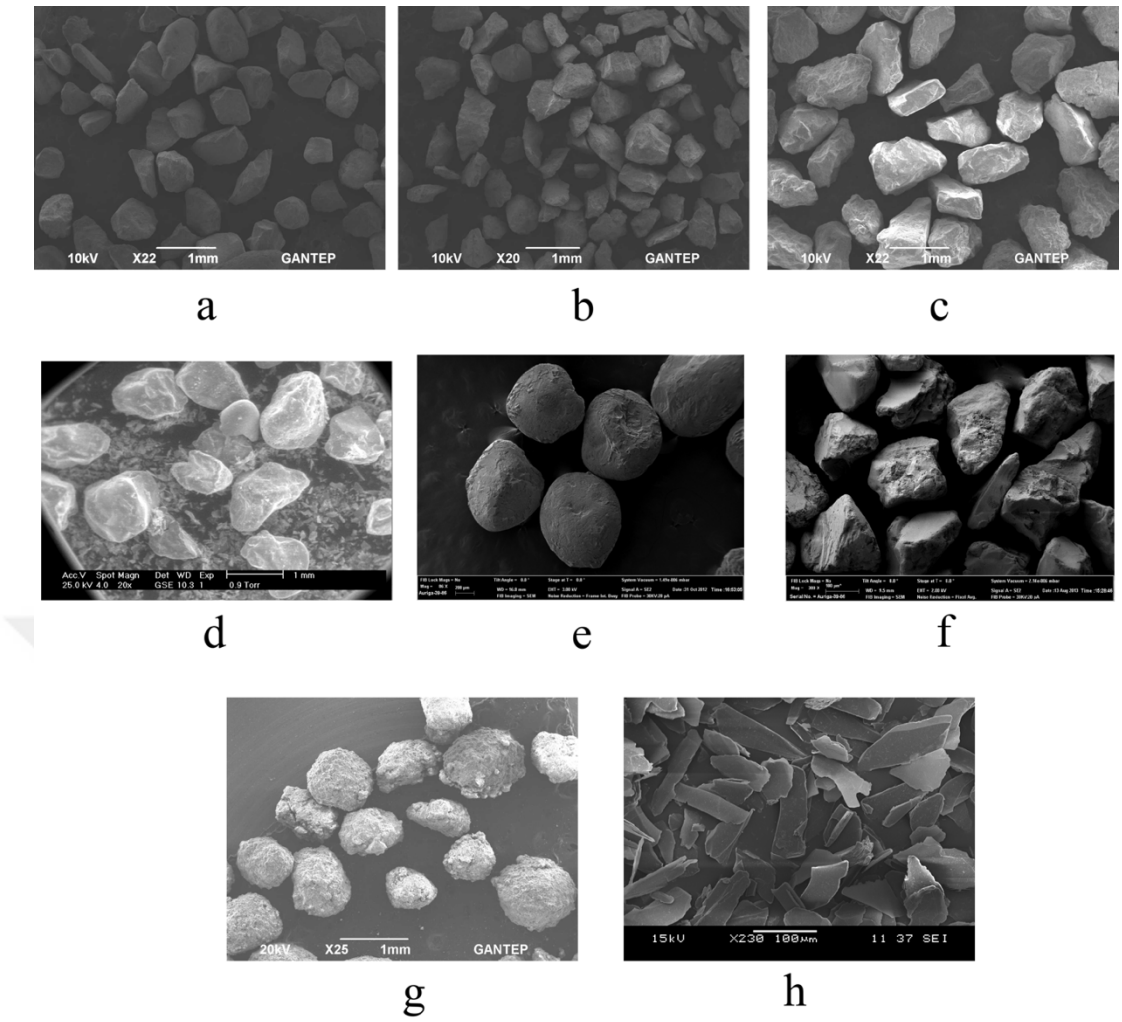

Figure 3.12 Scanning Electron Microscope (SEM) Pictures of the samples used: (a) Narli Sand, (b) Crushed Sand, (c) Trakya Sand, (d) Leighton Buzzard Sand, (e) Ottowa Sand, (f) Toyoura Sand, (g) Fly ash, (h) Mica.

3.3.4 Computation of the ICF Shape Factor

This section explains the computational algorithm procedure that is used to develop the shape parameter which uses the Fourier transformation (FT). FT is a mathematical representation of curves in a finite series of sinusoidal functions that decomposes functions and are applied to waveform in music or images (Folland, 1992). The procedure starts by obtaining a sample image and transferring it into an image editing software. The software changes the colors of the image into a monochrome system, which will be easier to identify the contours of the shapes in the computer program as shown in Figure 3.13.

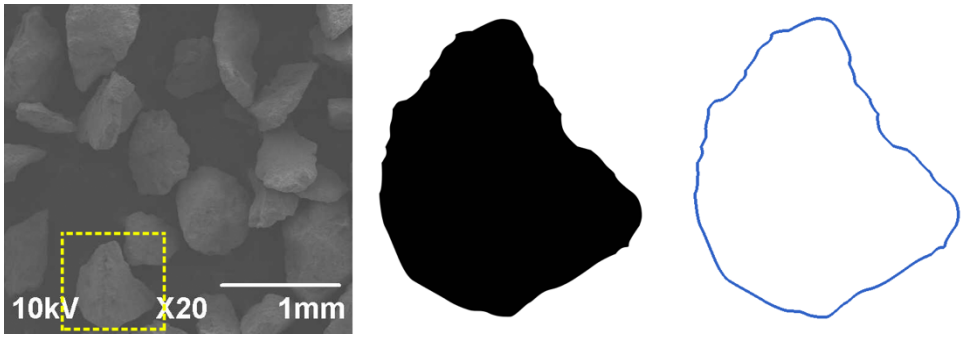

Figure 3.13 Contouring process for a sand grain.

The Fourier transform of the contour whose representation is a sequence of z(n) can be described as follows

$$Z_k = \frac{1}{N}\sum_{n=0}^{N-1} z_n e^{\frac{-2j\pi nk}{N}} \tag{3.18}$$

In Equation 3.18, k = -N/2, ..., -1, 0, 1, ..., (N/2)-1.

A new contour function is generated using the inverse Fourier transformation. Some statistical moments related with the new function need to be defined. These moments are found by scanning the boundary of the shape, which is described as follows

$$m_p = \frac{1}{N}\sum_{n=0}^{N-1} {z_n}^p \tag{3.19}$$

In Equation 3.19, the order of the moment is represented by the term p, and the number of points that the shape boundary has in total is denoted by n. The second term and the 10th term of the inverse of Fourier transform were included in the calculation in order to define a value named total moment.

$$m = m_2 + m_{10} + d_{2,max} \tag{3.20}$$

In Equation 3.20, signature value of the contour calculated by using the 95 percentiles of the first two harmonic terms is denoted by m_2, while the same signature value for 10 terms is denoted by m_{10}, and finally the maximum number of any signature value for a given boundary using 2 terms is represented by $d_{2,max}$. A coefficient was calculated that will be useful for defining the final shape factor using these values as follows

$$f = logratio\left(\frac{m}{d_{ave}}\right) \tag{3.21}$$

As can be seen in Equation 3.21, a new function was defined named logratio, which takes $\frac{m}{d_{ave}}$ as an argument. The input argument taken by the function is represented in the logarithmic scale in base 10, which is mapped into the range of numbers between 0 and 10. Therefore, while the values of the logarithm of the term goes from 0 to 1, the function is designed to give an output value between 0 and 10. Table 3.9 shows the logarithmic mapping of the logratio function.

Table 3.9 Application of logarithmic mapping

r1	r2
0.0	0.0
0.1	0.04
0.2	0.09
0.3	0.14
0.4	0.19
0.5	0.26
0.6	0.34
0.7	0.43
0.8	0.55
0.9	0.72
1.0	1.0

The values that appear on the left column that are represented by r1, are sample input values which are given in increments of 0.1. The column on the right-hand side, with the title r2, shows the outputs generated using these values. The relationship between each row in the table presents how the logratio mapping works. When taken a closer examination, it can be concluded that the r2 values start slowly, then get closer to the input values as they are increased. After the logarithmic mapping was applied, it was observed that as the complicated features of a contour increase the ratios do not follow a similar pattern. In other words, instead of having a linear correlation, they have a logarithmic correlation which is a better descriptor for the changes that occur in the features of a shape.

In Equation 3.21, the f value gives information about how the contours are able to conform to their Fourier transformed counterparts. It also has a close relationship with the traditional roundness that can also describe irregularity. The optimum number of

harmonic terms were found to be 10 when taking into account the factors such as the pixel density and image dimensions. The canvas that the image is displayed on the editing software was chosen to be 300 x 300 pixels. All of the images acquired by the SEM were scaled to fit this size, which provides a comfortable viewing perspective across a variety of screen sizes. It was observed that including more than 10 harmonic terms reaches a diminishing returns threshold, where contribution of the additional terms will not have any significant influence on the result. Using more terms with this particular method would be related with detailed characteristics of the particle such as smoothness or texture, which is not addressed in the current study. Finally, the ICF is calculated as

$$ICF = 1 - f \tag{3.22}$$

Figure 3.12 displays a critical step of the shape calculation procedure where the retrieved outlines of the particles are overlapped on the original shape contour. For each of the images, Fourier transformed contours are shown by thick lines. The deviations from the original contours can be seen as vertical lines between the two overlapping images. They are used to calculate the distance moments. The image on the left-hand side shows a procedure done with 2 harmonic terms, while the one on the right-hand side is a procedure done with 10 harmonic terms.

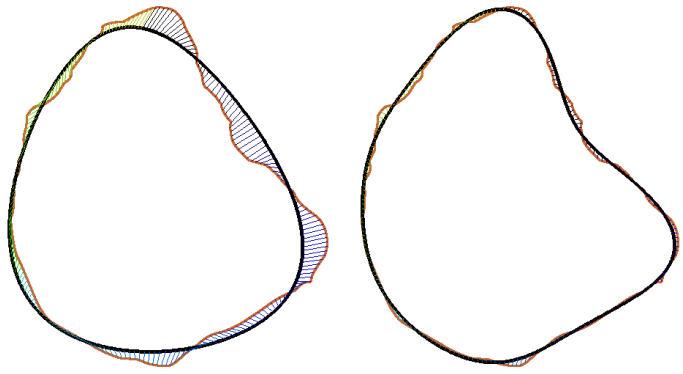

Figure 3.14 Shape retrieval and outlining process for a sand grain.

Table 3.10 shows the calculated shape factor and the related parameters for the sample image shown in Figure 3.14.

Table 3.10 Crushed sand sample calculations

Shape	m_2	m_10	d_max	d_ave	Area	ICF
Crushed sand sample	10.400	1.586	12.804	62.986	12251	0.34

3.3.5 Outline of the Program

The computer program that makes the calculations is developed in Python, which is an object-oriented programming language which supports an abundance of artificial intelligence and image recognition libraries specifically developed for it (Kuhlman, 2011). The program is written in a modular and an easy-to-follow fashion, which can be divided into three compartments: (1) The first segment in the program imports the dependent libraries for image recognition and mathematics, and defines the constants, (2) the second segment is where the main algorithm, display and output functions can be found, (3) and the last segment is related with the input functionality through which user interactions can take place.

The users can easily tweak and change some of the parameters related with the particles, such as the number of harmonics. The display options include the rows to be separated by tab characters, which can be useful when exporting the data into a spreadsheet. Additionally, the details of the calculations can also be viewed. Pseudo-code 3.1 displays an outline of the steps taken by the program.

begin

<1> Import the libraries

<2> Define constants related to output and harmonics

<3> Get the shape folder and begin the shape analysis for those shapes

<4> Depending on what TABBED_INFO_STYLE was chosen, print the first line

<5> Begin loop for each shape in the shape folder

<6> Get the grayscale image

<7> Find the contour and store it

<8> If SHOW_IMAGES is true

<9> Show the image with contours

<10> End if

<11> Calculate the area of the original shape

<12> Turn the contour into complex tuples

<13> Calculate the Fourier transform and store it in the complex number formats

<14> Begin loop for each harmonic within the predefined constant start and end values

<15> Calculate the inverse harmonic transformation according to the current harmonic value

<16> If SHOW_IMAGES is true

<17> Show the image generated by the inverse harmonic transformation

<18> End if

<19> End loop

<20> Calculate the signature value using the harmonic contour

<21> Calculate the distance moments between the original image contour and the harmonic contour and store it as

mx

<22> Calculate the distance moments between the original image contour and the harmonic contour using the lower harmonic value and store it as mxb

<23> Find the 95 percentile values for mx and mxb

<24> Sum the maximum distance, mx, and mxb values and store it as value1

<25> Calculate a number using the logarithm function and store it as value2

<26> Divide value2 by the average signature value and calculate the ICF

<27> Display the results according to the chosen style

<28> End loop

end

Pseudo-code 3.1. Main steps of the program.

3.4 Test Facility and Slope Box Modeling

The test facility and the arrangement of the slope model box is illustrated in Figure 3.15-3.17.

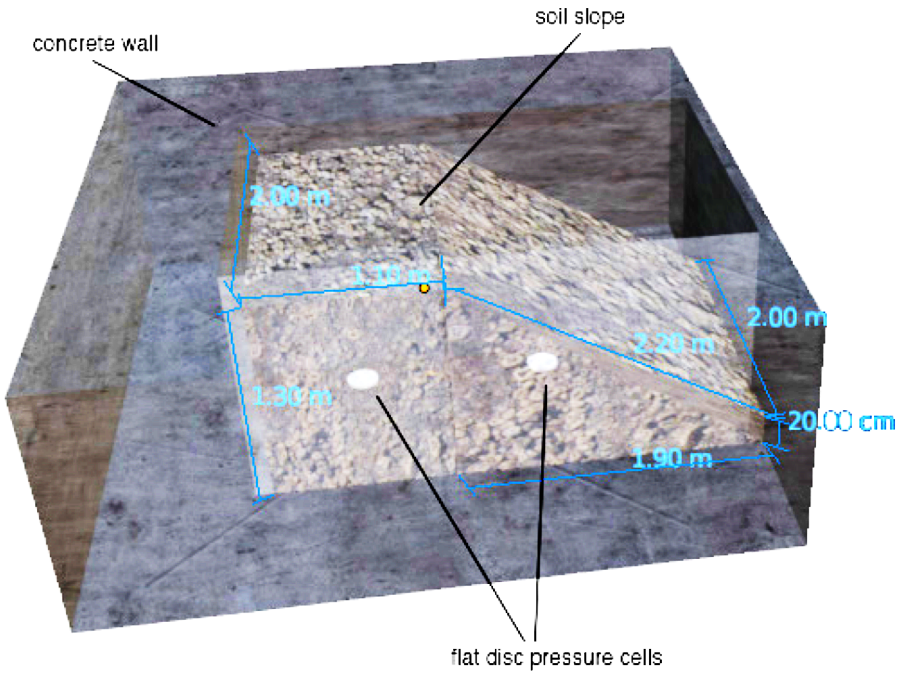

Figure 3.15 General arrangement of the slope box facility.

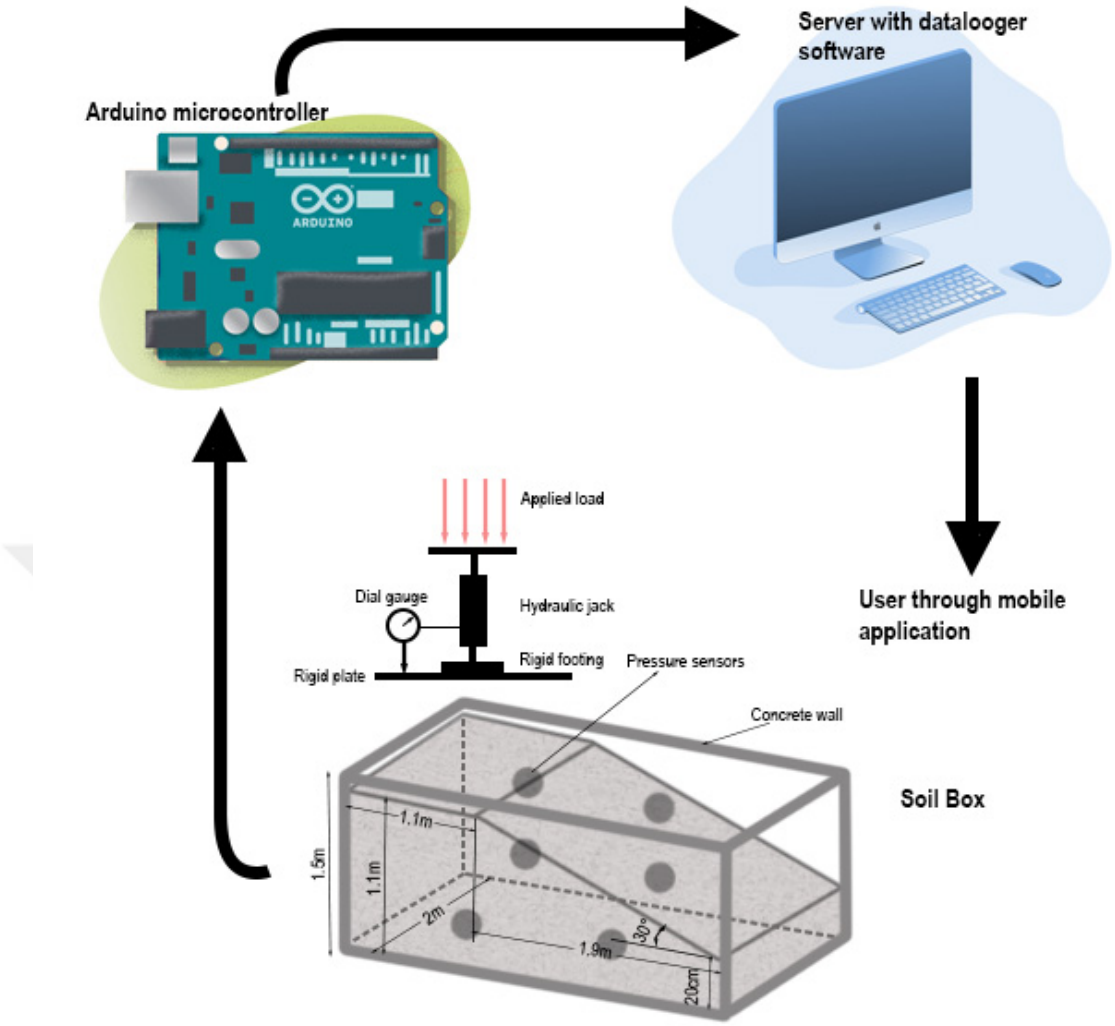

Figure 3.16 Schematic view of the data logging system.

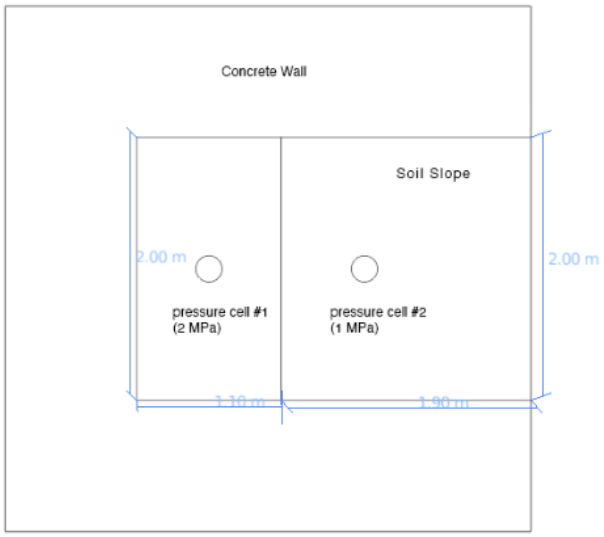

Figure 3.17 Top view of the slope box facility.

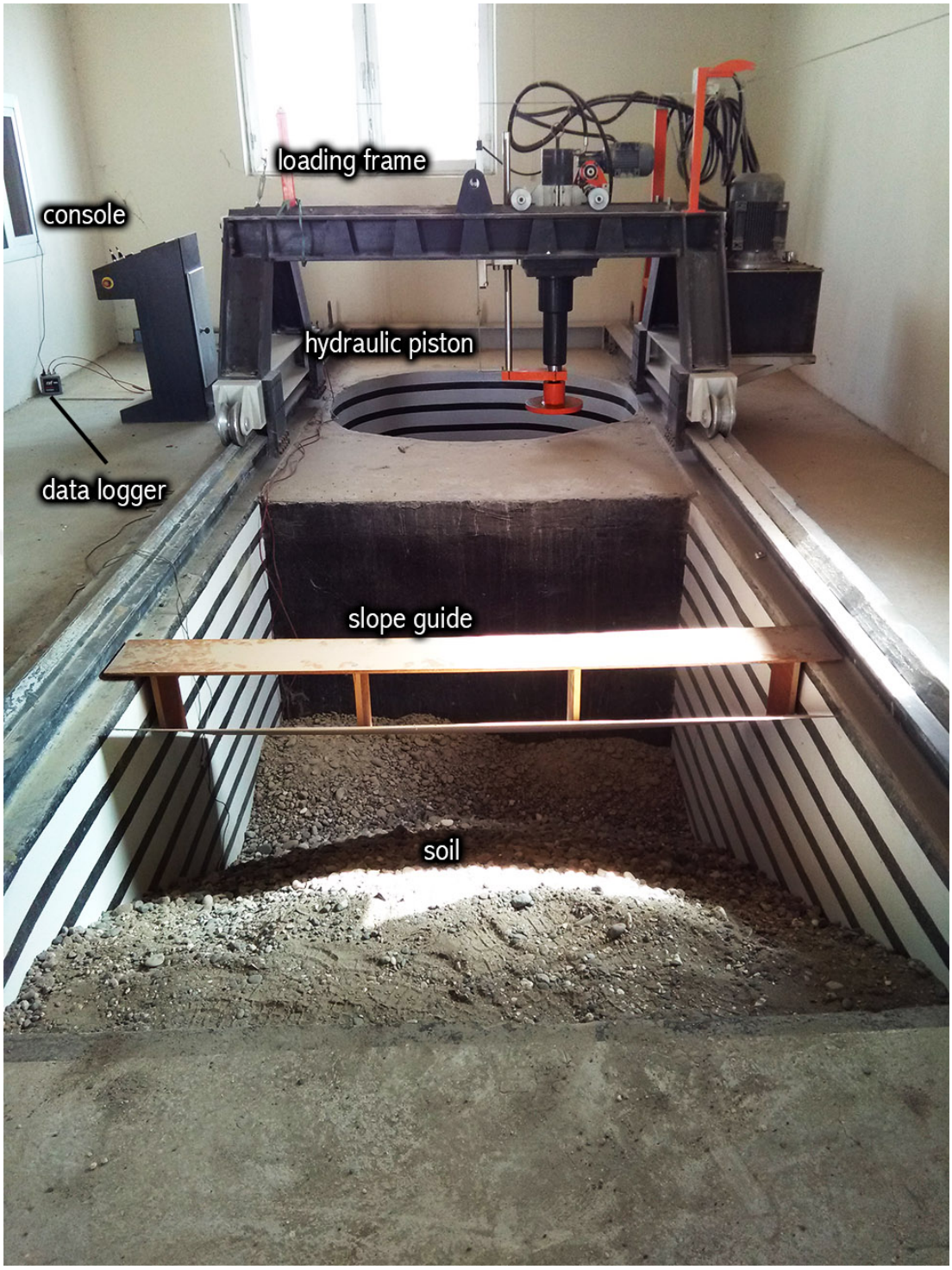

Figure 3.18 A picture of the slope box facility in the laboratory.

The slope box is made up of concrete as can be seen in Figure 3.18. The inside dimensions of the box are 2m X 3m in top view and is 1.5 m deep. The dimensions and the arrangement of the pressure cells are also illustrated in Figure 3.4. On the slope box, there is also a moving apparatus, on which a pressure cell and a hydraulic piston is attached as can be seen in Figure 8.5. The apparatus is controlled by a computer and

is able to move horizontally through the rails installed on the sides of the box. The bottom of the box was filled with a 10-cm layer of clay in which the flat disc load cells were embedded. They kept fixed in that position throughout the series of experiments that were performed.

Figure 3.19 A 3D rendering of the slope apparatus.

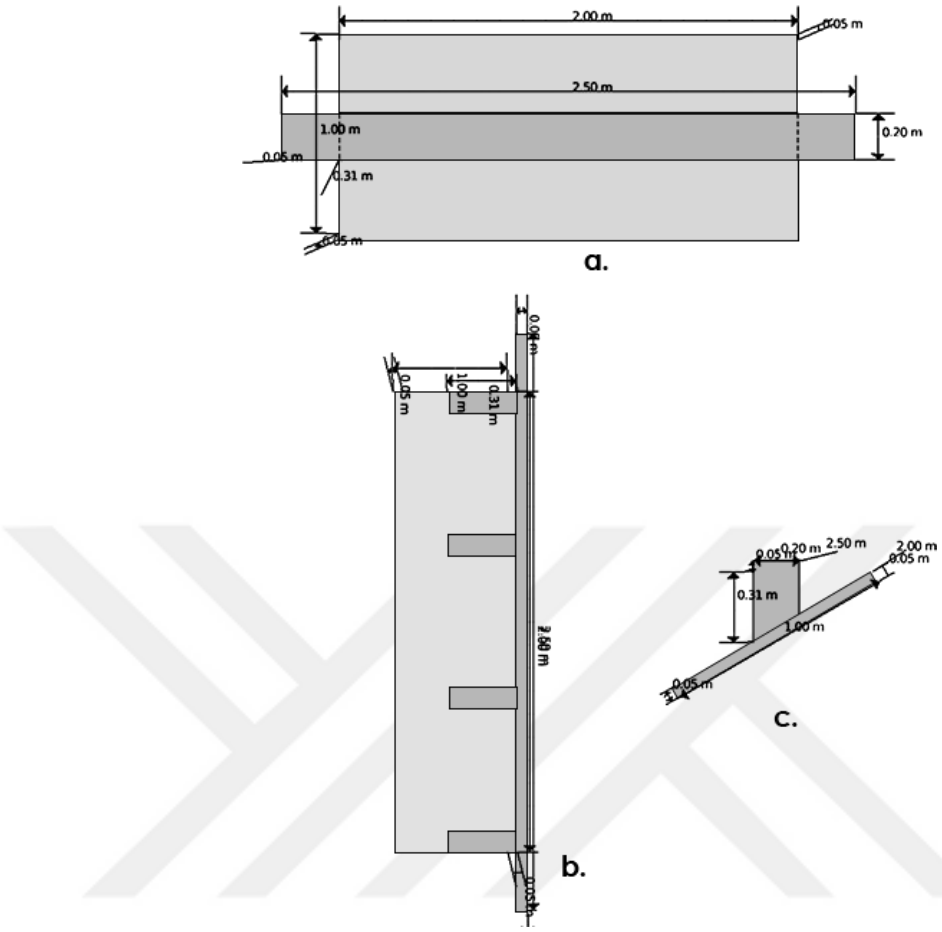

Figure 3.20 (a) Top, (b) Anterior, and (c) Lateral view of the wooden apparatus.

There is a wooden apparatus shown in Figures 3.19 and 3.20 that allows to give the slope the angle as can be seen form the figure. The soil can be filled slowly in order to produce a loosely packed slope. The apparatus has a designed slope of 30 degrees; however, it is possible to increase or decrease the angle by placing an object at the side extensions.

To perform these experiments in this particular setup, at least one technical personnel should be available to be able to operate the moving mechanism and apply loads. After each experiment, the soil needs to be replaced. However, since the data logger system is connected through the web server, the researchers or students performing the experiment can easily observe and evaluate the experiment away from the laboratory without the need to travel there.

3.5 Monitoring System Implementation

The monitoring setup consists of a laboratory computer, a data logger made with an Arduino circuit board, and the Geo Data Logger computer application (What is Arduino?, 2018). An Arduino circuit board with an HX711 module was used to make the transducers communicate to the computer. Arduino is an open-source electronics platform based on easy-to-use hardware and software. An HX711 module is a circuit board, which is also a load cell amplifier that is capable of transferring the analog readings from the transducers into digital signals. 4 button shaped transducers with a maximum capacity of 2 MPa were hooked up to 4 individual HX711 units, which were then connected to the Arduino circuit board. The Arduino board makes it easy to customize and create circuit boards for specific needs. That is why this particular approach was chosen.

3.5.1 Application Interface

A data logger software called “Geo Data Logger” was programmed in JavaFX to be compatible with multiple platforms (Duke, J., & Rushforth, K., 2021). By using a gradle build, the source codes can be bundled and packaged to be run in any platform, including Linux, macOS, Windows, iOS, and Android (What is Gradle?, 2022). The program is able to connect to 4 transducers at once while simultaneously plotting the inputs on graphs. The program stores the data it receives from the transducers while simultaneously connecting to the Gaziantep University web server and uploading the data. The program can also be run on mobile platforms. In this way, the users can login to the program and observe the experiments and download the data from the experiments. The reason that the program code was written in JavaFX is that it is open source, it can be used to build for desktop, mobile and embedded systems built on Java. It is also an efficient toolkit for Java which can be used to build feature rich applications focused on graphical user interface (GUI). Also, since the application is going to be used for education purposes the graphical user interface plays an important role. In recent years, GUI applications have been attracting interest from many researchers and engineers. With the help of new and modern toolkits and platforms, the interest is aiming towards producing even better looking and user-friendly engineering applications.

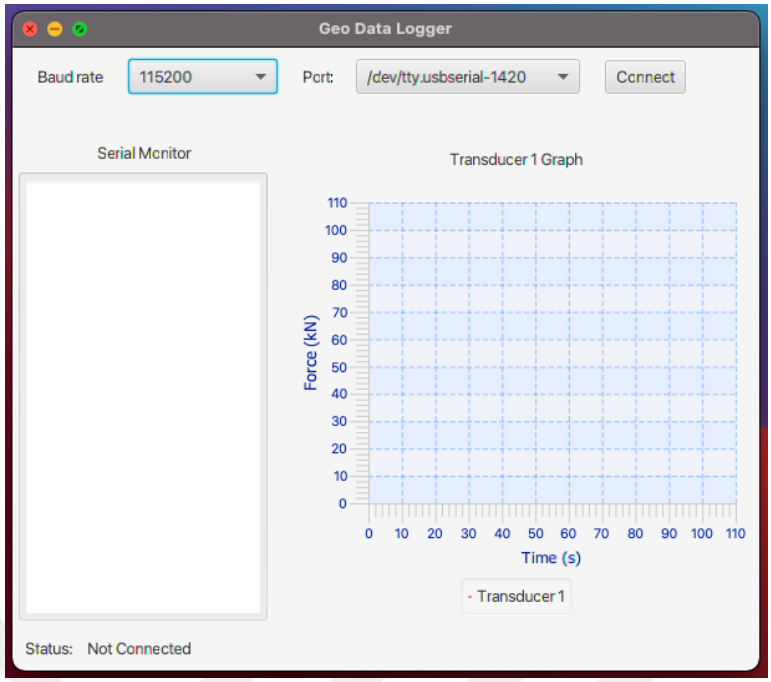

Figure 3.21 A screenshot of the Geo Data Logger software showing the main window.

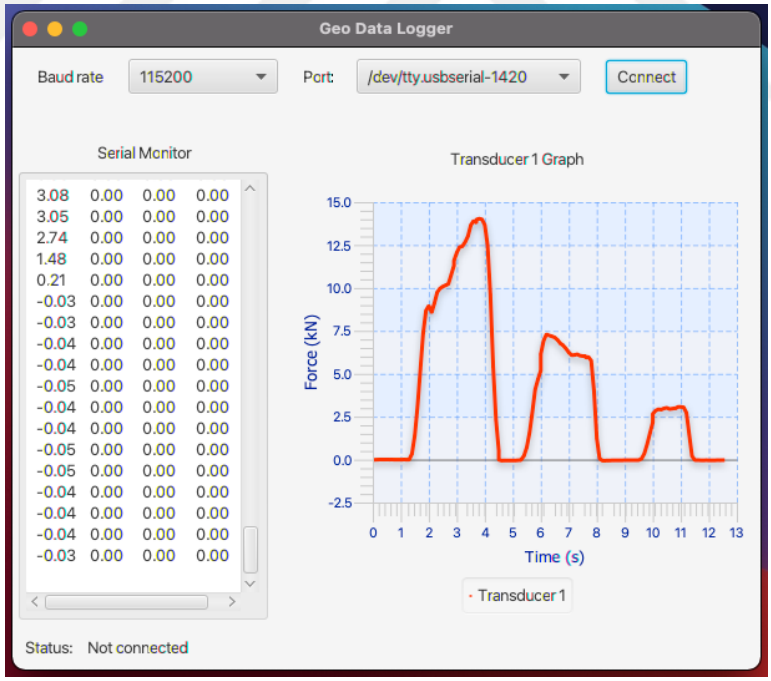

Figure 3.22 A test run showing the plotted graph.

When the application first opened, the user is presented with the main window in which there are three sections as shown in Figure 3.21. The first section is at the top that displays the Baud rate and port information and a connect button. In electronics,

baud rate is the number of signal or voltage level changes per second. In other words, it is the rate at which the information is transferred in a communication channel. Unit of baud is bauds per second. For example, a baud rate of 115200 means 115200 signal level changes are occurring within each second. The number is set to 115200 by default. It was configured this way, since the Arduino board that was used in this study supports this setting, and it also allows for a fluent and fast exchange of data between the transducers and the Arduino board. Right next to that there is a combo-box which displays currently connected ports on the computer. By port, it is meant a peripheral port or a connection on the computer that allows access to external devices such as printers, modems, external hard drives, etc. In this case, the connected port box should show the port number of the Arduino which is assigned by the operating system used in the computer. The Connect button attempts to connect to the specified port that is displayed to the user, and starts reading signals from the data logger. If somehow the connection is not established an error message will be shown. This might be because there could be other devices connected to the computer. Therefore, the user can simply choose a suitable port name from the combo-box until there are no error messages.

The second section of the main window is a text field that displays the digital values currently being read. The numbers are displayed in a 4-column fashion, each column representing one transducer. This field can be used for debugging purposes, in case there is anything wrong with the transducers. It can also be used to extract the exact values of the readings as the experiment is running.

On the right-hand side of the window is the third section. It displays graphical plots of the transducer readings. By default, the values are displayed Force (kN) versus Time (s). The axis names can be changed in the settings menu of the program. Figure 3.22 shows a sample output of a test. On the right-hand side, the program automatically plots the graphs in real time.

There is also a calibration menu, where the user can easily calibrate the transducers. During the calibration mode, the values are displayed live, so that any change made in the constant instantly reflects to the reading values, which makes it very easy and efficient to complete the calibration. There is a tick box which allows the scrolling to

stop in order to read the values easily and adjust the specified calibration constant accordingly.

The program is able to export the reading data into an Excel file. After every experiment, there will be an Excel file created by the program. Even if the connection is lost the file will be saved. Therefore, there will be no loss of data in case of any electrical shortage or software problems.

3.5.2 Remote Access Implementation

The data logging system was designed to be remotely with a mindset to make it possible with the least physical interaction possible. Therefore, an ultra-high-definition camera with a resolution of 3840 x 2160 at 30 frames per second was installed on the site pointing directly at the soil slope. This camera is always connected to the internet, and it is possible to observe the laboratory through the video footage provided by the camera.

The Geo Data Logger software has a remote component which is programmed as a mobile platform to be run on Android and iOS devices, as well as desktop computers. The remote interface provides access to live experimental data and the live video footage. While the experiment is running the computer at the laboratory constantly feeds the server with new data. As the new data becomes available it can be seen on the mobile app in real time.

In the mobile application, the user is able to either view live data or look at past experiments. On the top part the video footage shows the live feed from the laboratory. The users are able to see the technical personnel operating the pistons and how the experiment is being performed in real time. The program is also able to export the received data into an Excel file. The experiment data is always saved on the main computer at the laboratory, therefore there will be no loss of data.

3.5.3 Program Code

The JavaFX program for data logging and monitoring can be broken down into three components; the first component (i) connects to the transducers through the data logging Arduino device, the second one (ii) interprets the data using the calibration constants, and the third one (iii) communicates to the web server and uploads the data

and graphical plots. The aim of the program is to reduce the workload and make it easy to work with the experimental data.

Pseudo-code 3.2 gives the analysis of the computer code that runs the data logging system during the experiments.

begin

<1> Read the calibration constant stored.

<2> Read the available ports and display them

<3> When the button is clicked connect to the port

<4> Read the values and display them in columns

<5> Create the plots and display them

<6> Write on Excel file

<7> Upload the data to the server

end

Pseudo-code 3.2 Main steps of the Geo Data Logger program.

3.5.4 Calibration of the Pressure Cells

We have two flat disc pressure cells and four button type pressure cells to be used in the slope model. The calibrations were done in the laboratory using a UCT equipment.

Table 3.11 Calibration data points for Pressure Cell #1

Test 1	Test 2	Test 3	
3 VW 2 (kPa)	3 VW 2 (kPa)	3 VW 2 (kPa)	Utest (kN)
50	51.43	51.57	0
70.84	71.7		0.345
74.6	81.6	75	0.5
111.09	109.47	112.76	1
130.74	129	133.46	1.5
162.39	162.87	167.218	2

Table 3.11 (Continued)

184.86	187	192.034	2.5
222.65	214	220.24	3

Table 3.12 Calibration data points for Pressure Cell #2

Test 1	Test 2	Test 3	
1 VW 1 (kPa)	1 VW 1 (kPa)	1 VW 1 (kPa)	Utest (kN)
-82	-84.73	-84.75	0
-13.46	-8.1	-7.5	0.5
52.06	59.93	60.38	1
127.25	137.41	137.8	1.5
207.75	193.46	194	2
267.95	254.89	256.29	2.5
333.22	321	323	3
404.51	394.69	398.18	3.5

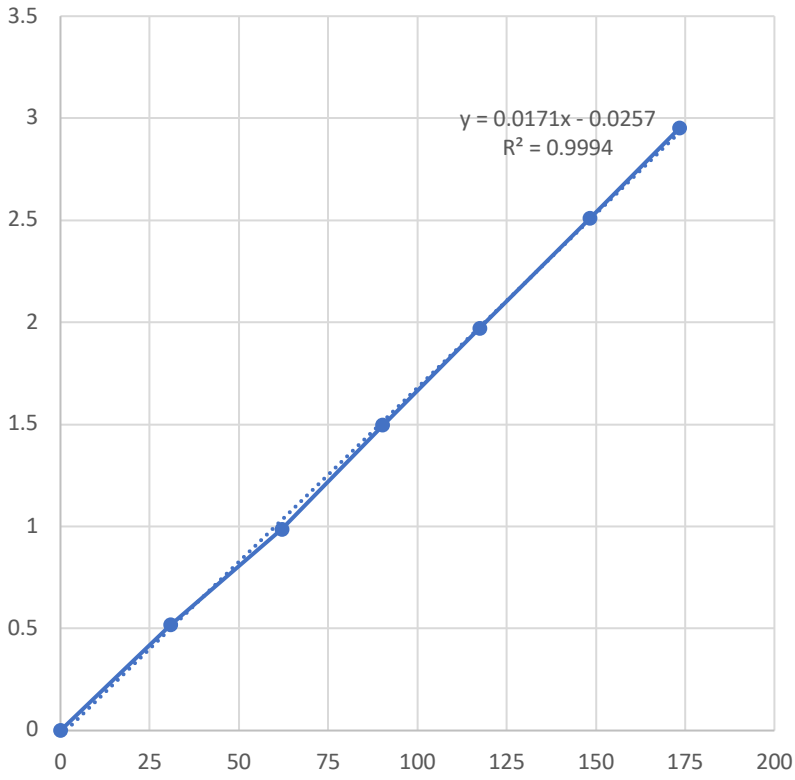

Figure 3.23 Calibration graph for Pressure Cell #1.

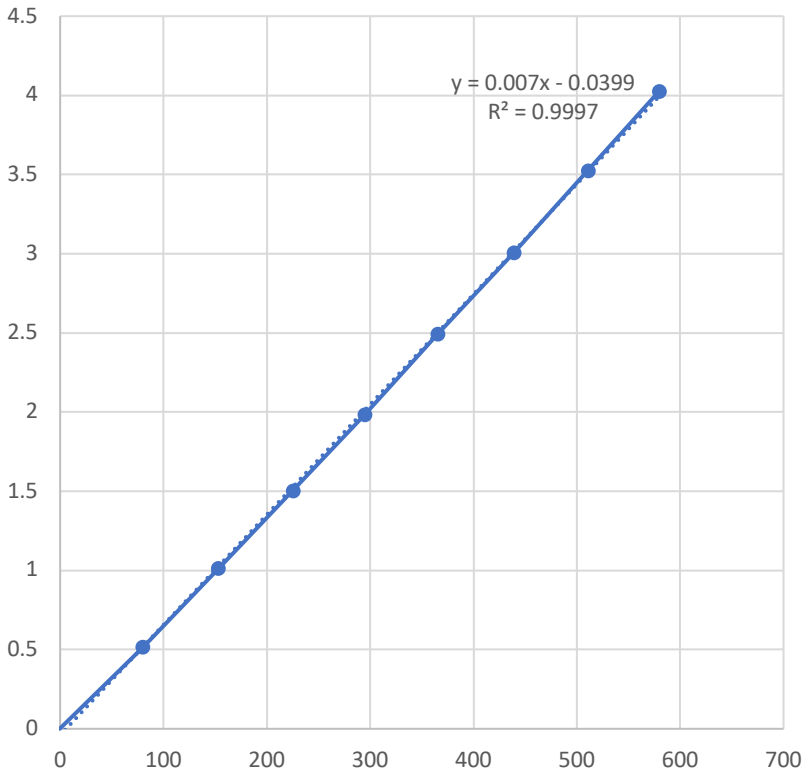

Figure 3.24 Calibration graph for Pressure Cell #2.

As can be seen from Table 3.11 and Table 3.12, the calibrations were done using 3 tests with the UCT equipment. The results from these tests showed significant correlation between the raw data inputs form the data logger versus the kPA readings from the UCT equipment as can be seen in Figures 3.23 and 3.24.

CHAPTER IV

RESULTS AND DISCUSSION

This chapter presents the results and interpretation of the shape and size analyses, series of slope stability experiments that were carried out in the large-scale slope box model, and discusses the effects of shape and size of soil grains to the slope stability.

4.1 Shape Factor Study Results

Sample calculations were done using simple shapes that were drawn on computer and also using the images of sand samples.

Figure 4.1 Sample angular shapes.

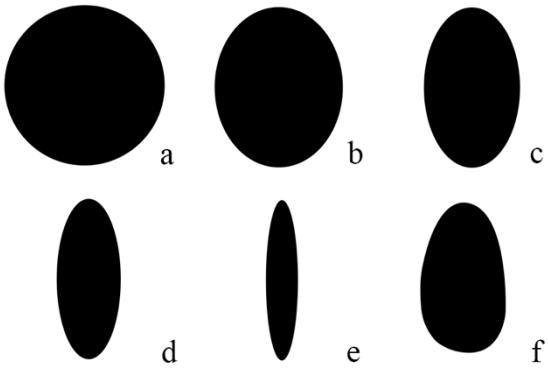

Figure 4.2 Sample rounded shapes.

Figure 4.1 shows angular samples and Figure 4.2 shows rounded samples that were produced in an image editing program. These will be the reference images to check the calculations against. The calculations for the generated simple shapes provide a basic understanding of how the shape factor works as can be seen in Table 4.1.

Table 4.1 Calculations for the simple shapes

Shape	m_2	m_10	d_max	d_ave	Area	ICF
Triangle	42.951	5.635	52.000	113.896	36231	0.05
Rectangle	29.117	7.123	33.897	165.218	83646	0.32
Star10	5.726	8.788	7.041	133.138	55654	0.61
Circle (a)	0.000	0.000	0.0	125.398	49427	1.0
Rounded1 (b)	2.599	0.586	2.615	112.459	39583	0.83
Rounded2 (c)	5.968	0.586	7.041	98.605	29756	0.65
Rounded3 (d)	11.527	0.822	12.117	84.459	19875	0.44
Rounded4 (e)	13.967	2.828	17.090	71.582	9932	0.28
Egg (f)	7.897	0.822	9.142	91.461	25303	0.56

The 95-percentile value regarding the distance moments was a critical value that was found through an extensive test of the program. The triangular shape that was defined to be the most angular shape as seen in Figure 4.1. The roundness of the corners was better able to be represented instead of using an average signature moment. Additionally, with these parameters the shape factor becomes close to 0. Table 4.1 illustrates this situation with a triangle shape that has an ICF value calculated to be 0.05. For this reason, and also since the shape has the minimum corners to be represented in the Fourier transformation, the shape was chosen as a calibration. The variations between the values of m_2 and m_{10} are not do not affect the overall result.

The advantage of this is that as the particles assume a more angular shape, the ICF value responds slowly but increases more linearly as the angularity decreases.

The shape factor was designed to be easily computed and comparable to the commonly used traditional value defined by Wadell (1933). AF and SF shape factors presented by Sukumaran and Ashmawy (2001) was designed in such a way that the values mostly lie between 0% and 100%. In a similar fashion, the range of the ICF values are between 0 and 1. 1 represents a perfect circle, while 0 represents the most angular sand shape. Even though theoretically this value can get values smaller than 0, it is worth noting that for practical purposes it is highly improbable for the value the reach negative numbers. These numbers represent highly irregular shapes which will have roundness of 0.

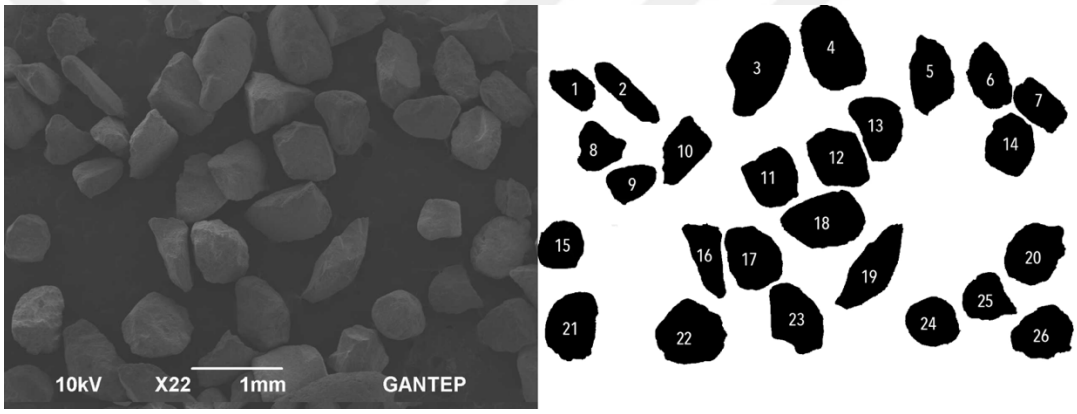

Figure 4.3 An SEM picture of the NS sample and after it is digitally processed.

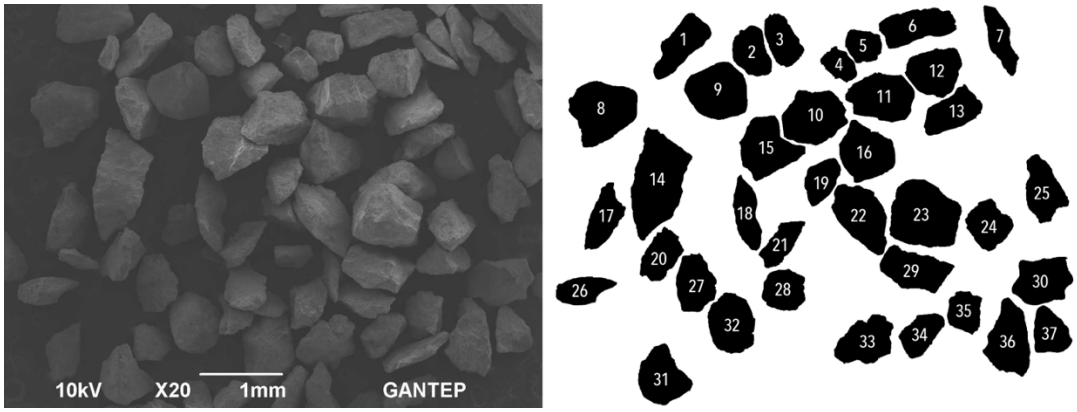

Figure 4.4 An SEM picture of the CSS sample and after it is digitally processed

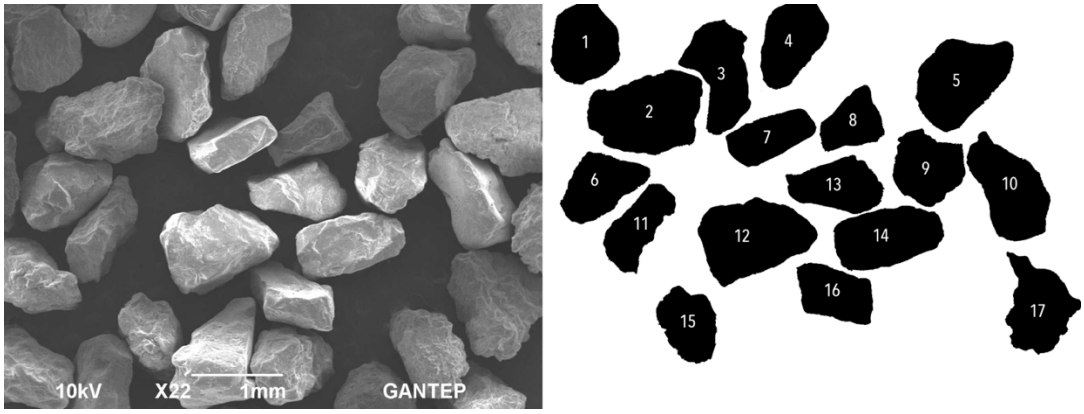

Figure 4.5 An SEM picture of the TS sample and after it is digitally processed.

Figures 4.3, 4.4 and 4.5 show Scanning Electron Microscope (SEM) pictures of NS, CSS and TS samples and processed versions of the grains for each of the sample set. The individual particles were numbered to easily reference them in the tables. Each numbered particle shape was then drawn separately within dimensions of 300 x 300 pixels, where 1 mm of length corresponds to 220 pixels.

Table 4.2 Calculation of ICF for the NS sample

Shape number	m_2	m_10	d2_max	d_ave	Area	ICF	R
1	0.82	3.59	4.43	51.52	7804.5	0.59	0.4982
2	1.75	5.76	8.04	65.07	9783.5	0.5	0.4547
3	2.71	11.36	14.92	89.74	23870	0.41	0.611
4	1.75	5.57	7	87.71	23391	0.61	0.5576
5	3.06	6.92	10.81	71.27	14908.5	0.44	0.3587
6	1.75	5.38	8.34	63.44	12093.5	0.5	0.4725
7	1.75	3.59	4.85	59.29	10459	0.59	0.4834
8	2.19	8.57	9.32	55.45	9572	0.37	0.3668
9	0.82	4.13	4.49	51.84	8217.5	0.58	0.5896
10	1.59	8.18	9.87	65.07	12195	0.43	0.3819
11	1.75	5.79	8	67.41	14172	0.51	0.4258
12	1.75	2.81	5.77	72.5	16275	0.64	0.4152
13	1.59	10.39	11.16	68.83	14411	0.4	0.4113
14	1.86	3.4	5.3	65.8	13521	0.61	0.5146
15	0.82	0	1.71	57.78	10485.5	0.86	0.531
16	3.06	12.65	15.02	66.15	11378.5	0.29	0.2264
17	1.59	4.02	6.05	72.84	16434.5	0.61	0.4689
18	1.41	6.93	9	81.83	20332.5	0.54	0.4956
19	2.8	10.68	16.59	81.42	16731	0.36	NaN
20	3.24	3.77	5.3	72.82	16355	0.6	0.5135
21	1.75	6.3	7.37	72.97	16525.5	0.54	0.3889
22	2.19	4.13	6.4	79.09	19626	0.61	0.4553
23	2.83	6.93	7.17	73.85	16467	0.51	0.4812
24	0.82	0.26	2.21	61.86	11965.5	0.83	0.8646

Table 4.2 (Continued)

25	1.75	9.13	10	58.17	10451.5	0.37	0.5509
26	2.83	4.08	4.85	68.03	14409	0.59	0.4712

Table 4.3 Calculation of ICF for the CSS sample

Shape number	m_2	m_10	d_max	d_ave	Area	ICF
1	2.71	11.1	12.46	63.33	10690	0.32
2	1.75	5.73	6.4	52.31	8363.5	0.47
3	0.82	3.14	5.77	51.85	7939.5	0.57
4	1.75	1.29	2.07	39.37	4702.5	0.66
5	0.82	1.53	2	42.36	5593	0.72
6	2.71	10.39	13.11	65.96	11998.5	0.34
7	2.19	7.77	9.87	55.68	7266.5	0.38
8	2.62	13.06	15.88	77.17	18431	0.33
9	0.82	3.34	3.6	71.19	15824	0.7
10	2.83	4.58	7.17	71.02	15718.5	0.55
11	3.06	6.02	6.7	68.89	14659	0.51
12	1.75	5.03	5.77	61.98	12016	0.55
13	1.75	6.34	9.87	58.59	9909	0.42
14	5.44	18	20.5	94.01	24380.5	0.28
15	2.59	19.48	24.73	69.03	14722	0.15
16	2.59	8.46	11.55	66.6	13800.5	0.39
17	2.01	8.55	12.8	57.83	8839.5	0.33
18	1.75	8.53	11.03	57	7993	0.36
19	0.82	4.38	6.18	47.48	6715	0.5
20	2.71	3.81	6.66	53.18	8418.5	0.49
21	2.71	4.58	7.37	49.15	6453	0.43
22	2.71	7.91	11.55	71.48	14844.5	0.42
23	2.71	5.53	7.04	83.73	21824.5	0.58
24	1.59	6.34	8.6	54.11	9156	0.43
25	2.68	9.46	10.23	60.99	10673.5	0.37
26	1.59	6.71	10.13	50.41	6955.5	0.37
27	2.19	4.13	5.63	58.56	10361	0.55
28	1.59	0.63	2.07	51.56	8374.5	0.76
29	2.71	11.09	15.25	65.16	12476	0.3
30	4.67	5.58	6.4	64.12	12657	0.48
31	1.59	10.4	12.8	62.99	12269	0.34
32	2.19	1.27	3.06	64.35	12880.5	0.72
33	3.97	6.93	8.6	62.02	11761	0.42
34	1.46	4.53	5.44	49.54	7341	0.51
35	1.75	2.6	4.43	46.19	6657.5	0.57
36	3.69	10.58	11.28	69.16	13903.5	0.36
37	1.59	5.38	6.4	50.2	7704	0.47

Table 4.4 Calculation of ICF for the TS

Shape number	m_2	m_10	d_max	d_ave	Area	ICF
1	1.75	5.71	7.37	89.53	25001.5	0.6
2	5.8	13.97	16.63	117.65	42018	0.42
3	4.59	31.33	38.42	98.16	28084.5	0.11
4	1.59	8.57	10.65	89.41	23903	0.51
5	3.59	16.91	17.56	108.07	34999	0.38
6	2.71	14.94	16.1	86.52	22341.5	0.35

Table 4.4 (Continued)

7	1.75	9.71	11.28	79.92	18214.5	0.45
8	2.71	12.65	16.38	71.74	15374.5	0.3
9	3.06	14.02	19.74	85.68	23075.5	0.31
10	4.99	16.41	19.19	104.21	31196.5	0.35
11	4.24	17.48	23.84	82.69	18935	0.22
12	5.01	18.87	22.02	114.33	39675	0.34
13	3.59	10.49	14.72	87.17	21814	0.4
14	2.71	10.39	12.46	102.08	30390.5	0.49
15	4.22	5.53	9.56	78.46	18989.5	0.49
16	2.71	8.87	11.16	81.81	19833	0.46
17	6.65	26.54	29.13	95.88	26753	0.16

In order to make the evaluations regarding the particle shapes, 3 sand samples were initially selected. Figures 4.6-4.8 displays the comparisons of these samples with regards to Wadell's roundness values (R). Table 4.2-4.4 shows the numerical values of the shape factors associated with the numbered particles. The R values were calculated using a computer program developed for MATLAB (Zheng and Hryciw 2015). The researchers were able to compute the corners using a parameter called the maximum divergence. The definition given for this important parameter is the maximum differential value between the approximated straight line and the curve in a given segment. However, since the corners are not identified in Fourier transformation methods, dealing with the maximum divergence becomes unnecessary for the current study. During the computation of R values, some of them were not able to be identified due to their small sizes.

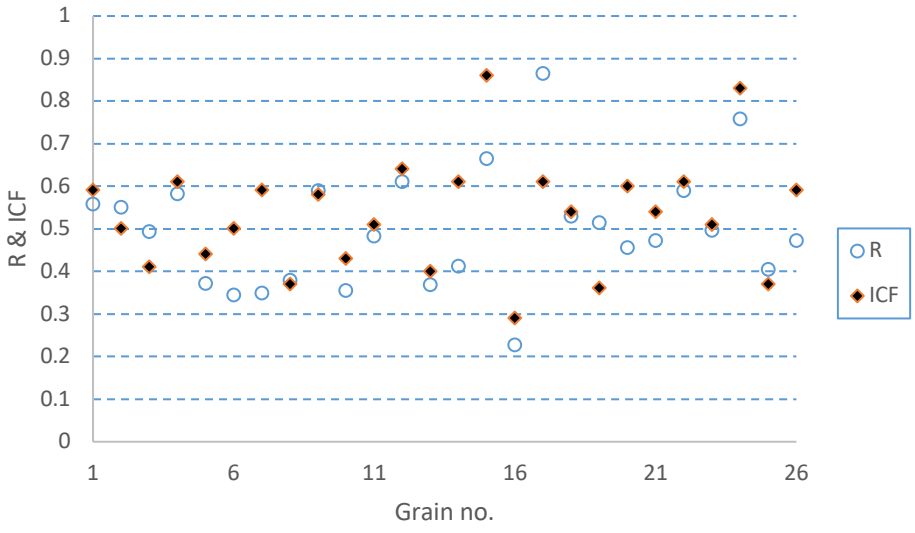

Figure 4.6 NS sample ICF and R values.

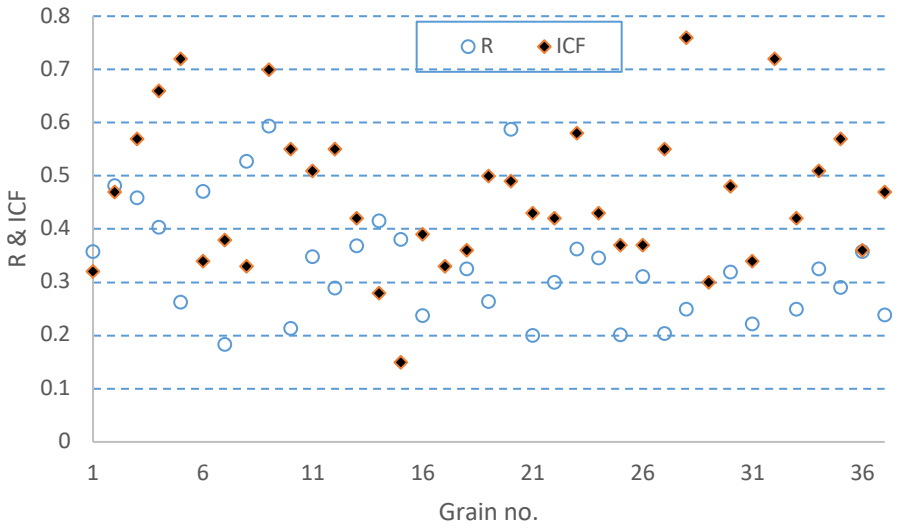

Figure 4.7 CSS sample ICF and R values.

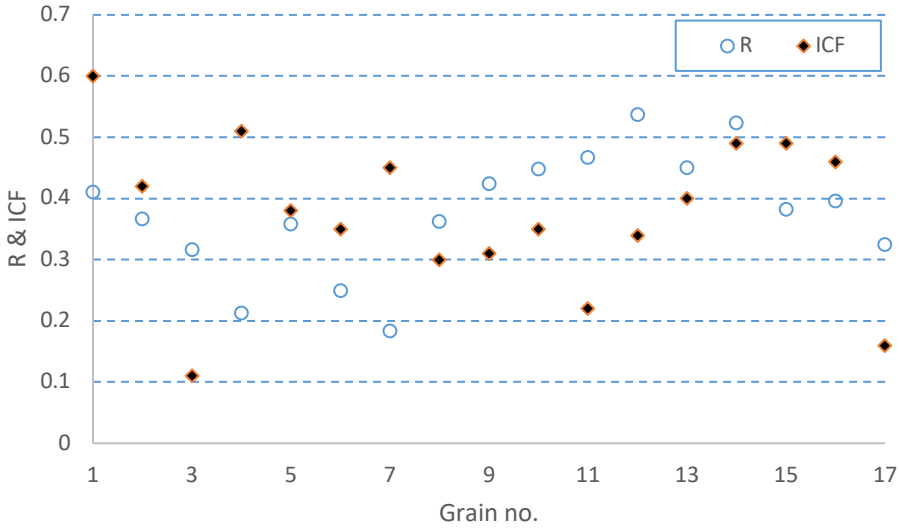

Figure 4.8 TS sample ICF and R values.

In the TS samples, the average value of the R was found to be 0.38, whereas the average ICF value was computed as 0.37. This sample was the one where the values had the highest correlation. Comparatively, in the NS sample there was also a high correlation where the average R value was 0.50 with respect to the ICF value which was 0.53. The standard deviation for the samples were calculated to be 0.13. And finally, for the CSS sample, the average value of the R was computed to be 0.33, whereas the average ICF value was found to be 0.46. Some conflicting results were also observed for the particles where the dimensions that correspond to the pixels were

small. When these particular shapes were retraced in order improve the pixel density, it was observed that the values of R and ICF match closer, as shown in Figure 4.9.

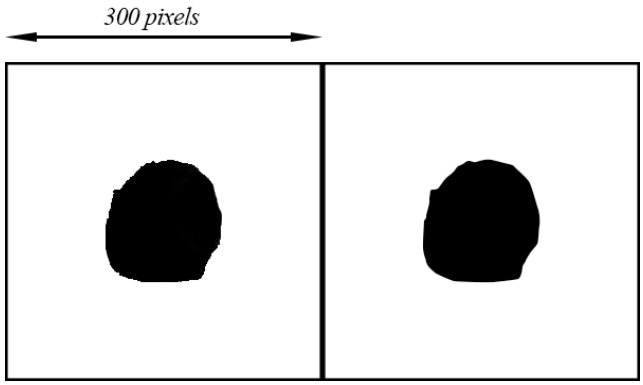

Figure 4.9 The image on the left is NS sample grain number 15, and the one on the right is the redrawn image.

The roundness values for some of the particles belonging to the NS sample were recalculated and shown in Table 4.5. The new values corresponding to the previous ones can be seen.

Table 4.5 Recalculation of some R values for the NS sample

Shape number	Old R	New R	ICF
4	0.3889	0.5824	0.61
5	0.2565	0.371	0.44
6	0.2264	0.3435	0.5
9	0.2852	0.5896	0.58
10	(NA)	0.3547	0.43
11	0.3846	0.4821	0.51
15	0.3105	0.6643	0.86
16	0.4258	0.2264	0.29
18	0.3231	0.5288	0.54
24	0.3587	0.7575	0.83

The average values of roundness and ICF for the CSS sample were found and the ratio was calculated to be 1.09. This ratio for the NS sample was found to be 1.14, whereas the TS sample had a value of 1.06. A high correlation was seen between the R and ICF for the TS, CSS, and NS samples. However, because of the particular nature the crushed sand the particles have irregular characteristics, which led to slightly larger differences for these particular group of sands.

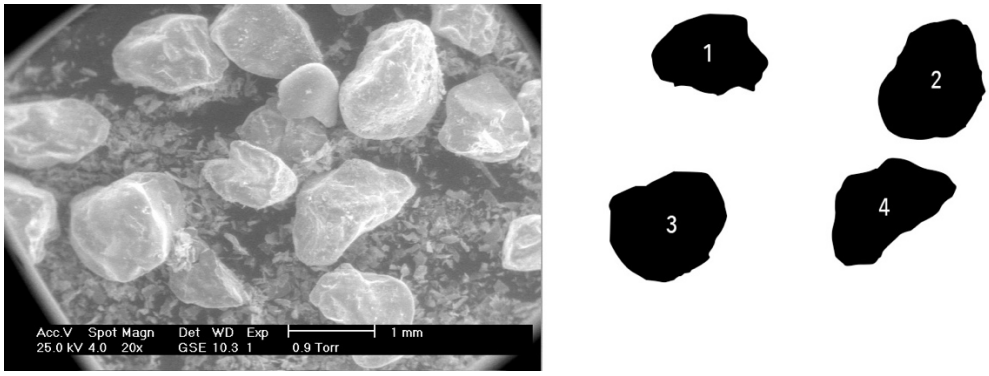

Figure 4.10 An SEM picture of the LS sample and after it is digitally processed.

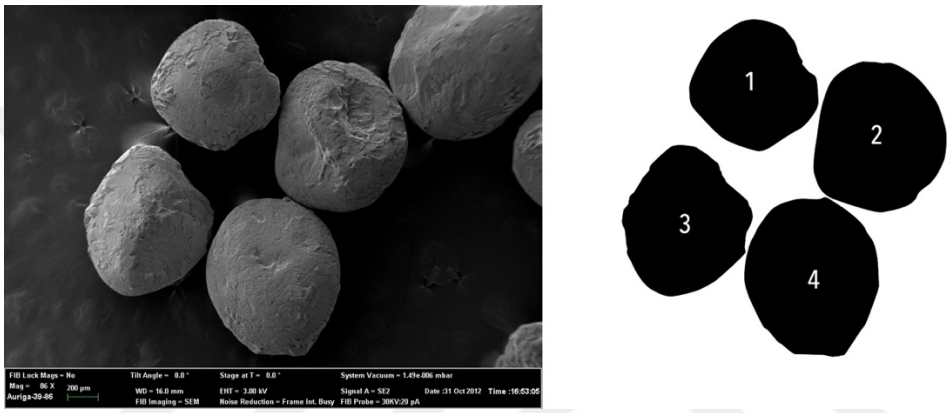

Figure 4.11 An SEM picture of the OS sample and after it is digitally processed.

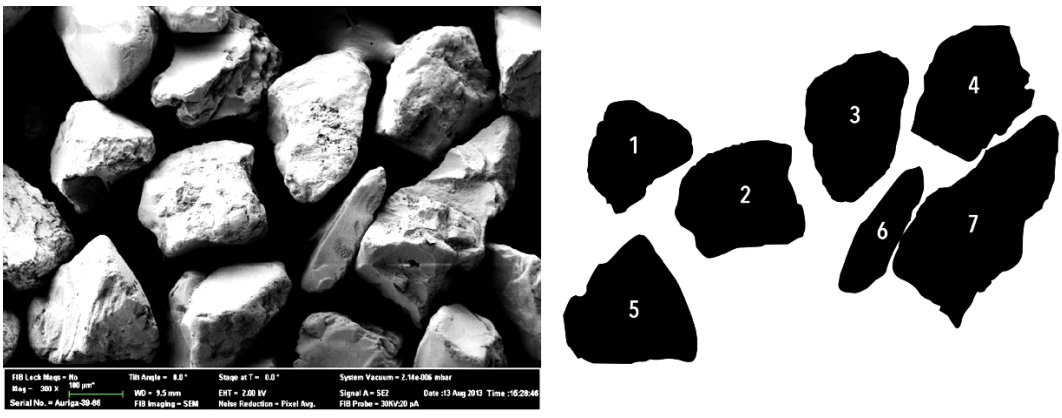

Figure 4.12 An SEM picture of the TOS sample and after it is digitally processed.

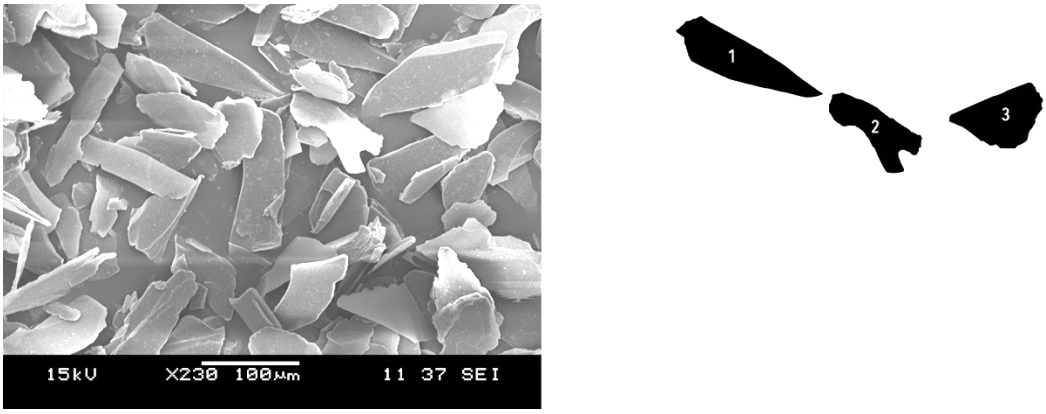

Figure 4.13 An SEM picture of the mica sample and after it is digitally processed.

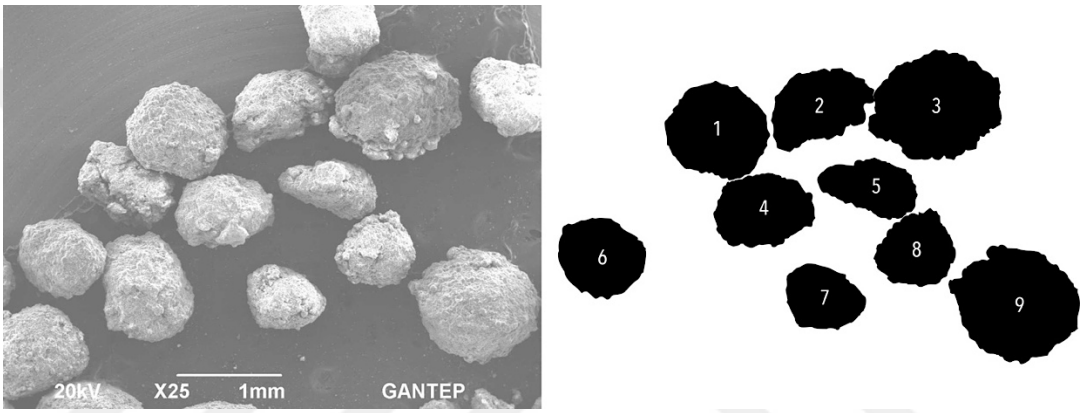

Figure 4.14 An SEM picture of the fly ash sample and after it is digitally processed.

An intensive series of tests were carried out to evaluate the method for different particles. Figures 4.10-4.14 show SEM pictures of LBS, OS, TYS, mica and FAP samples and processed versions of the grains for each of the sample set.

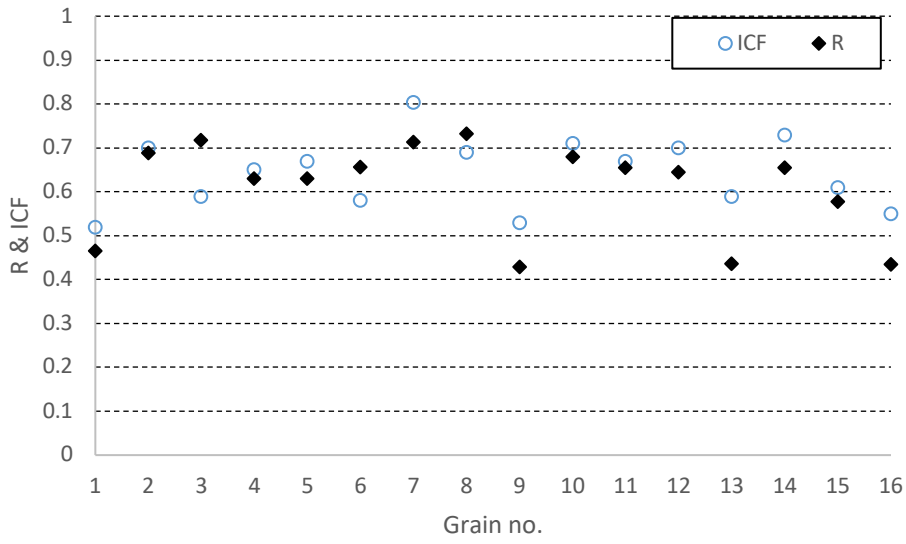

Figure 4.15 Ottawa sand sample ICF and R values.

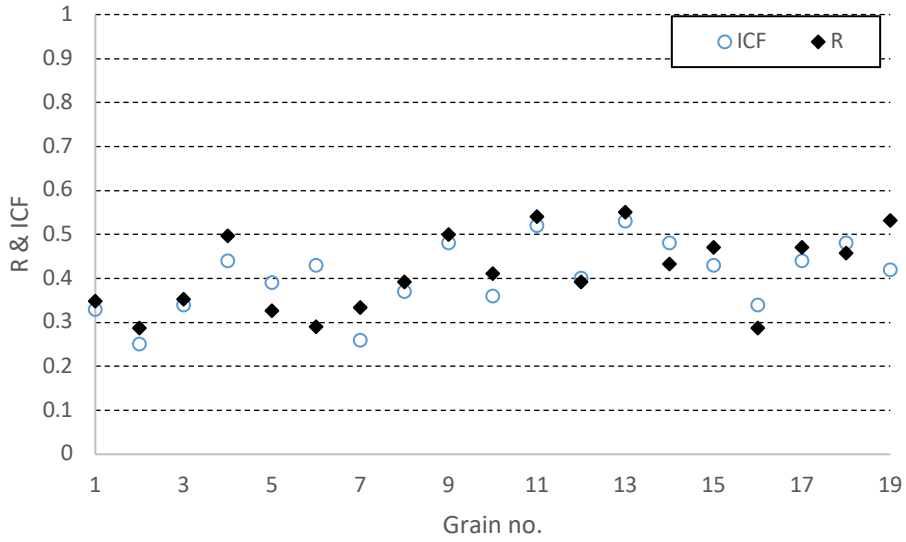

Figure 4.16 Toyoura sand sample ICF and R values.

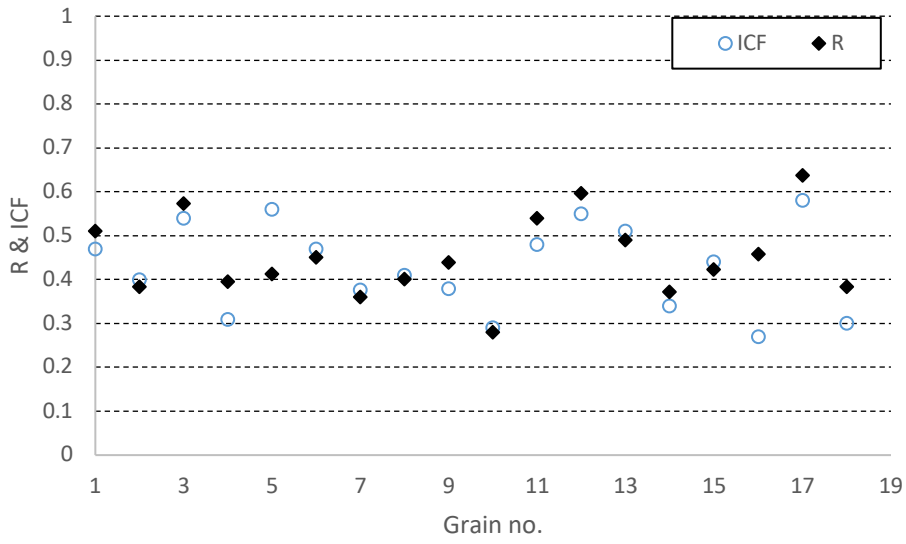

Figure 4.17 Leighton Buzzard sand sample ICF and R values.

Figures 4.15, 4.16 and 4.17 demonstrate the comparison between R values obtained through the method of Zheng et al (2015) and the ICF values. The results seem to indicate that the ICF method produces consistent and similar results with the traditional R values.

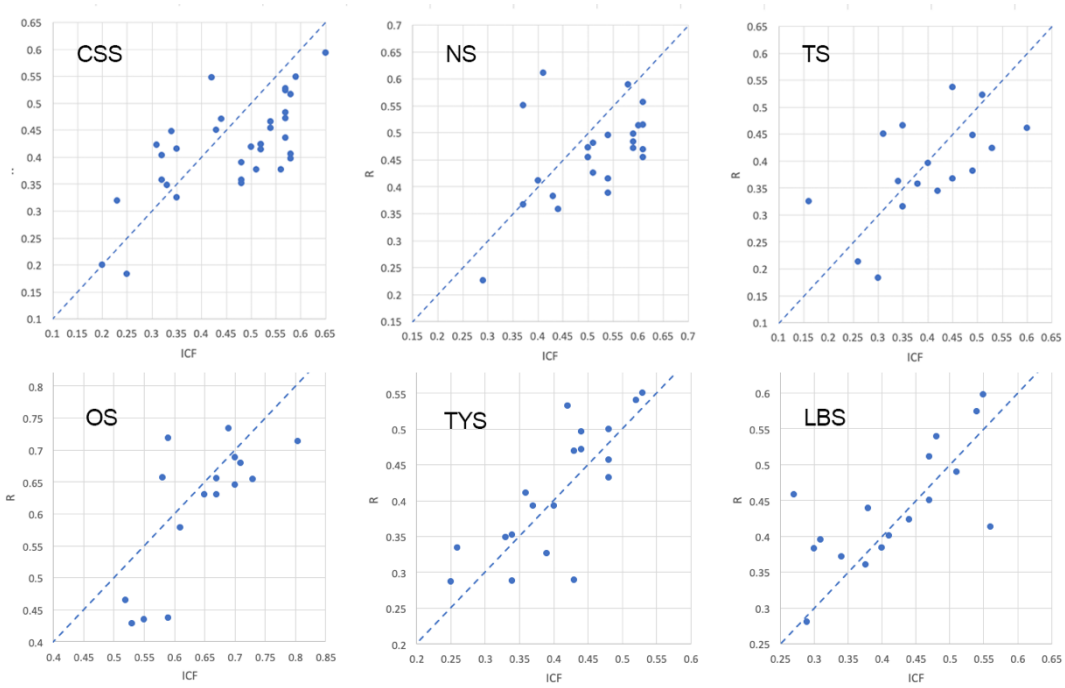

Figure 4.18 Comparison of ICF and R values.

Figure 4.18 also illustrates also the comparison between R values obtained through the method of Zheng et al (2015) and the ICF values. An equality line was drawn for each of the plots in order to easily compare the values.

The method was also used on mica and FAP samples that could be challenging for traditional roundness calculation because of the highly irregular features of the boundaries.

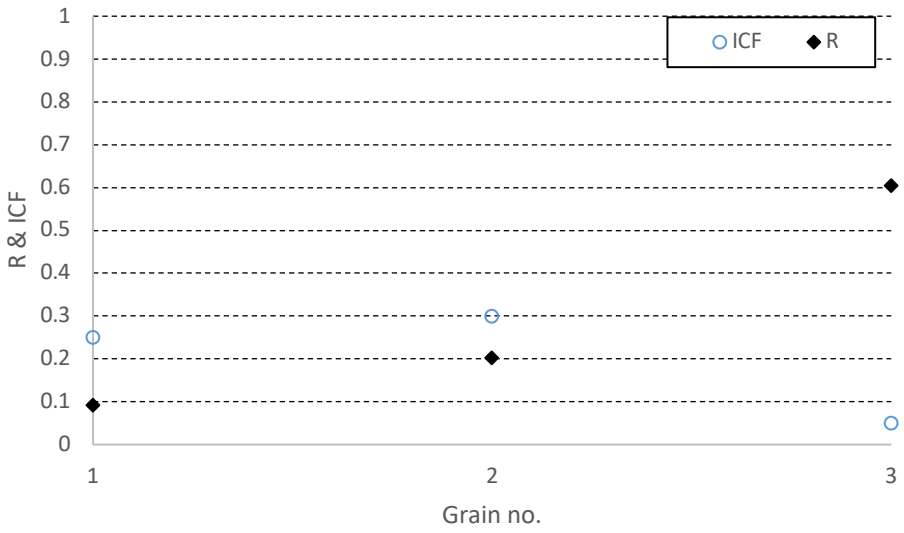

Figure 4.19 Mica sample ICF and R values.

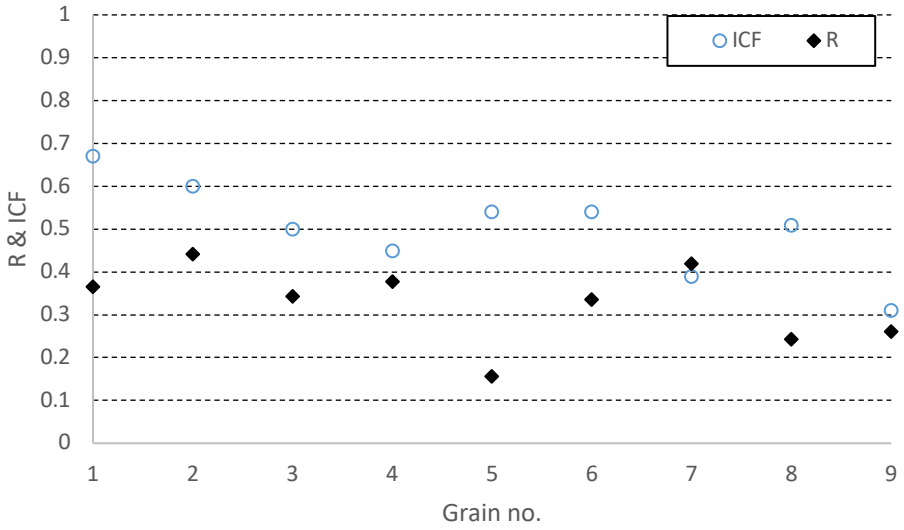

Figure 4.20 Fly ash sample ICF and R values.

For some of the particles that the R vs ICF values were compared, the differences are more prominent as can be witnessed in Figures 4.19-4.20. These differences were caused because of the fact that the particular sample they belong in, had irregular features. As it is illustrated in Figure 4.21a, the mica particle numbered 3, had a mostly concave shape, which resulted in the calculation of an decreased roundness value despite its seemingly rounder shape. The correlation ratio was calculated as 64% for the OS sample, while this value was 90.7% for the LS sample. Even though mica

originally had a negative correlation, when the concave particles were not added in the calculation, a 100% correlation was observed.

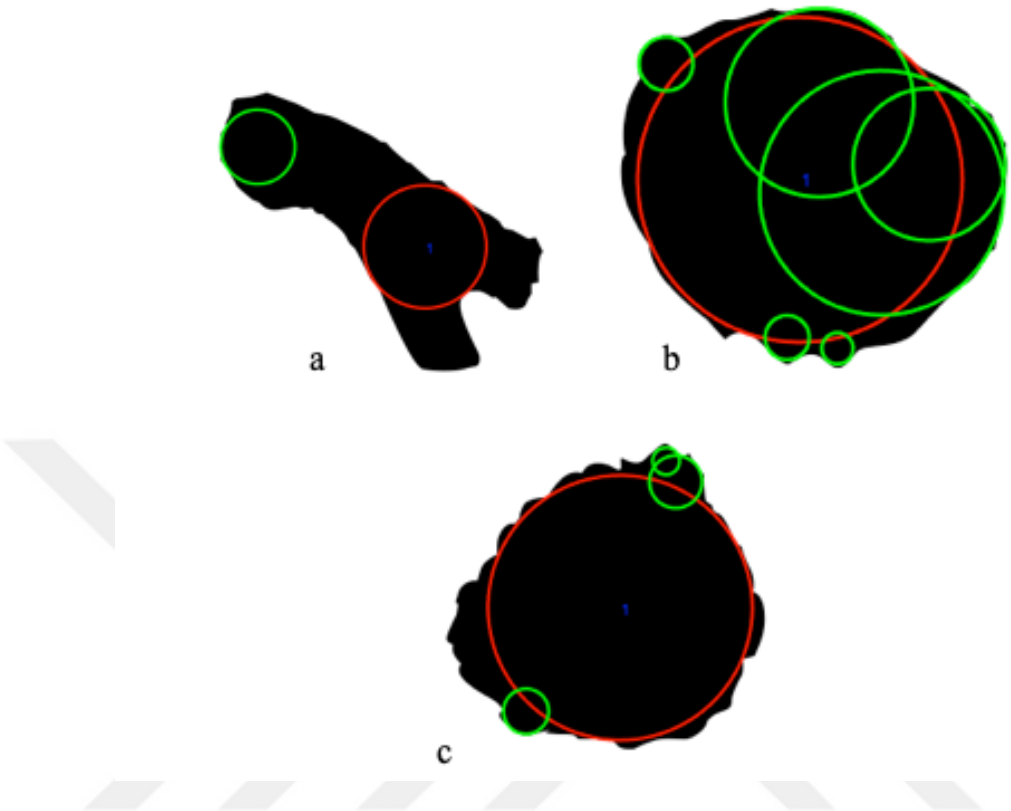

Figure 4.21 (a) Mica grain #3, (b) fly ash grain #1, (c) fly ash grain #5.

This conflicting values issue while calculating the R values also demonstrated in Figure 4.21a, Figure 4.21b, and Figure 4.21c. Because of the mentioned features of these certain particles the R values are calculated to be lower than expected, whereas the ICF values always seemed to present consistent results.

The roundness of particles has been traditionally determined by the usage of visual aids (Krumbein & Sloss, 1963; Powers, 1953; Less, 1964), which is still the most commonly used method today. Wadell's roundness (1932), which has been a highly accepted parameter was chosen for the definition for the term for the calculations. The advent of computer technologies made it possible for more advanced imaging methods to be developed, which in turn can be utilized in order to characterize complex soil geometries. Even the traditional methods can be automated with the usage of computers, as in the study presented by Zheng et al. (2015). In the literature, new

algorithms were developed that overcome the issue where the observer can be faulty by subjectively being more attentive to the more unusual particles (Hryciw et al., 2016). Roundness in detail was investigated in a number of other studies (Hryciw et al., 2016, Kandasami & Murthy, 2017, Kalyan & Kandasami, 2021). The examples presented in this chapter utilizes Fourier transformation method, which has also been investigated by other researchers (Schwarcz et. al., 1969, Diepenbroek et. al., 1992, Drevin, G.R., 2006, Resentini et. al., 2018, Demir et al., 2019; Sayinci et al ., 2015; Tralic et al., 2011; Koo & Kim, 2016). It is an powerful method that can be used to mathematically represent the shapes in a basic way.

Fourier transformation method has been mainly utilized to investigate the Fourier descriptors and the values produced with regards to triangularity, squareness, asymmetry, and elongation in order to evaluate the roundness of certain shapes. One of the methods that uses Fourier analysis in the literature is in the study of Sayinci et al. (2015) where they categorized certain cultivars of Turkish hazelnuts. The similar technique was presented by Demir et al. (2019) for the almond cultivars. The Fourier descriptor method was also used in medical fields in the study of the shape of breast tumors in order to identify malignant and benign tumors (Tralic et al. 2011). Resentini et al. (2018) used the analysis of Fourier transformation for soil particles and mapped them in the scale of Krumbein using the 4^{th} and 30^{th} order Fourier coefficients. The Fourier descriptors was also used in the study of roundness of soils (Koo and Kim 2016, Drevin 2006). A correlation between angularity and square root of the mean square differentiation of the particle diameters with regards to the order of Fourier sum was found (Schwarcz et al. 1969).

In this chapter, a novel use for the Fourier transformation has been presented throughout the intensive series of experiments that are conducted within the scope of shape analysis. This method has been used in a variety of disciplines also including shape recognition with powerful tools available to it, which makes it an ideal method for description of soils. The shape factor named ICF is comparable to the definition used commonly for soils to describe their shape, namely roundness. The comparisons to the roundness value were made by the computerized version of the roundness definition presented by Zheng et al. (2015) in order to eliminate subjectivity that will be caused by visual comparison. The new shape factor called ICF can also be used to

analyze how irregular a given shape is, which is the key difference between ICF and R. The resolution of the image or the density of the pixels are not the main influencer in comparison to the method provided by Zheng et al. (2015), which makes it possible to overcome challenges and the complexities associated by it, including divergence from the shape outline, aliasing effect. In the initial calculations, it was observed that some of the particles did not have consistent values within the particle group of the sample. For these particles, as the image resolution was improved the R values became higher and more consistent with the other particles. Therefore, it is concluded that the main issue causing this conflicting behavior is related with the pixels per circumscribing circle radius and the allowed maximum divergence from the curves, which is a fixed number. The ICF presented here is basically a shape parameter that is a description of the behavior of the shape of a particle, where the information about how a given representation of the shape or its inverse Fourier transformed version is able to fit its shape outline. The advantage of this proposed shape factor is its ability to give insight into the roundness, and efficiently describe detailed features of a particle no matter how complicated the features are. Additionally, regarding the computational performance, since the program is written in a standalone environment, it is able to produce the outputs almost instantly, where a modern processor took around 1 second to finish all the calculations. In comparison with the other numerical methods that evaluate shape of soils, the procedure presented here gives a detailed description of shape using the Fourier transformation method, which can also be improved further for shapes in different disciplines. The procedure relies on the computer algorithm which takes the user inputs which have been preprocessed. The SEM images has to be properly acquired and transferred to the computer. In terms of the pixels are concerned, simple photographs do not provide detailed level information that is needed for the precision of the algorithm. Once the images are acquired the editing procedure can take place, where the particle images are converted into monochrome layers. Despite the advantages of the algorithm, the procedure approximates the shape characteristics, which may not always be sufficiently precise depending on the factors such as image quality, editing, and the constants for the harmonics.

4.2 Large-Scale Model Slope Stability Test Results

An intensive series of laboratory experiments were conducted using the 3m x 2m x 1.5m large-scale soil box. All of the samples were tested in the dry condition. The conditions during the setup can be separated into 3 cases: (1) The first case is where the soil-box is completely full of soil, (2) the second one is where the soil-box is empty, (3) and lastly the case where there is a gradual loading of the soil-box. In order to remotely differentiate these cases, pressure cell gauges were used, which were located inside the soil-box. For the samples, the dry unit weights (γ_{dry}) were calculated to be 2.65 kN/m^3 and 2.18 kN/m^3. Considering the dimensions of the setup, the volume of soil to be loaded was calculated to be 5.33 m^3. The pressure cells that were placed on the bottom layer were tasked for measuring the speed of the loading process. While the workers were loading the soil, the students who are logged into the remote program were able to track of the progress of the experimental procedure as can be seen in Figure 4.22.

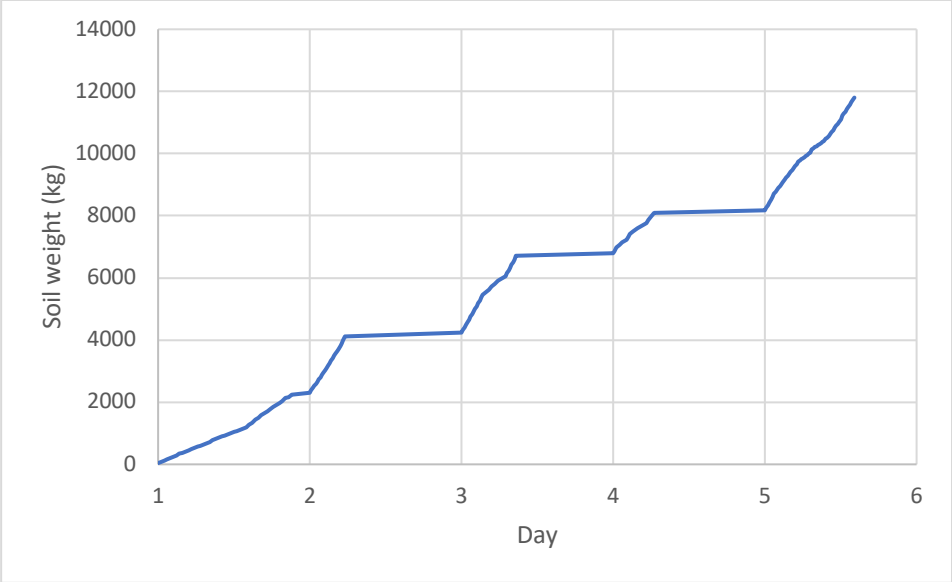

Figure 4.22 Change in soil weight measured by the pressure cells.

Figure 4.22 shows the soil loading process in a graph. The horizontal axis shows the time in days starting from the first day, when the loading started. As the work progresses, the data logger application keeps track of it simultaneously, collecting the data and plotting it into a graph.

Plate load tests were conducted in the rectangular footing setup for RRS and ACS samples. Taking into consideration the amount of soil to be loaded and the area of the footing, well graded and poor graded samples with a 45% relative density were chosen for the experiments. The laboratory tests were compared with numerical models created in Plaxis 3D software. A 3D model was created using the soil input properties that correspond to the samples used in the laboratory. Table 4.6 shows the input parameters that were used in the calculation for the numerical models. The steel plate which the load was applied from had a diameter of 30.5 cm and a thickness of 25 mm. The specific gravity of the steel material was 78.5 kN/m^3. The modulus of elasticity and poisson ratio values were 200,000 MPa and 0.3, respectively. The 3D mesh that was generated before the calculations is shown in Figure 4.23. The samples were correlated with the numerical models with varying stiffness values as shown in Figure 4.24. During the series of numerical simulations tests it was concluded that the best matching stiffness values for ACS and RRS samples were E=20 and E=24, respectively.

Table 4.6 Material properties in the FEM software

Sand type	Relative density	Dry unit weight (γ_d)	Stiffness €	Poisson ratio (ν)	Friction angle (φ)
RRS	45%	17.2	24	0.2	38
ACS	45%	16.4	20	0.2	38

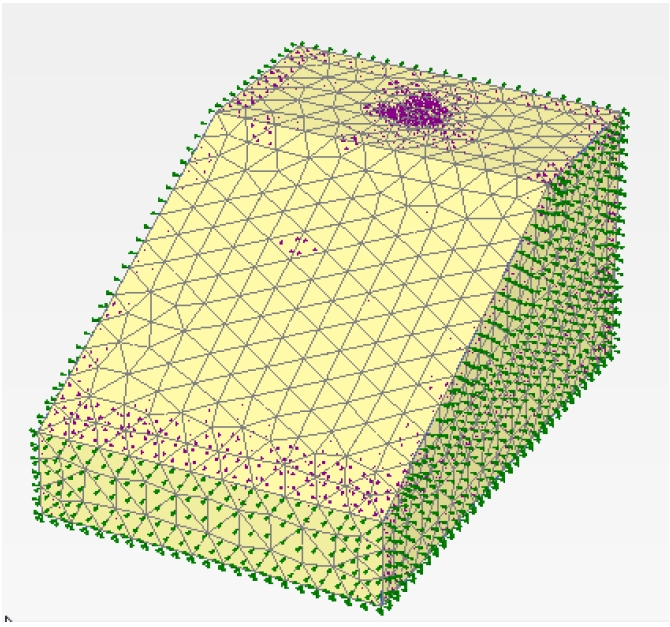

Figure 4.23 3D mesh connectivity plot generated in the FEM software.

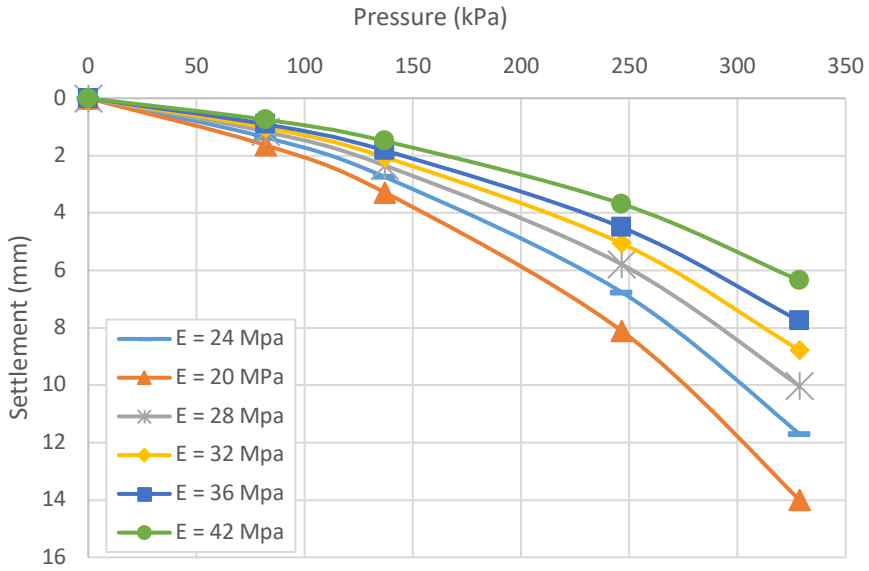

Figure 4.24 Pressure-settlement curves for ACS and RRS compared with the FEM models.

Table 4.3 Vertical settlements for the FEM models and the laboratory samples in plate load test

Applied Load (kPa)	Average settlement (mm)			
	E=20MPa	ACS	E=24MPa	RRS
0	0	0	0	0
27.4	0.43	0.2	0.36	0.5
54.8	0.96	0.8	0.8	1.2
82.2	1.6	1.6	1.34	2.4
109.6	2.39	2.65	2	4.3
164.3	4.26	6	3.5	6.5
219.1	6.68	10	5.56	8
273.9	9.9	12	8.26	9.3
328.7	10.5	13	8.73	12

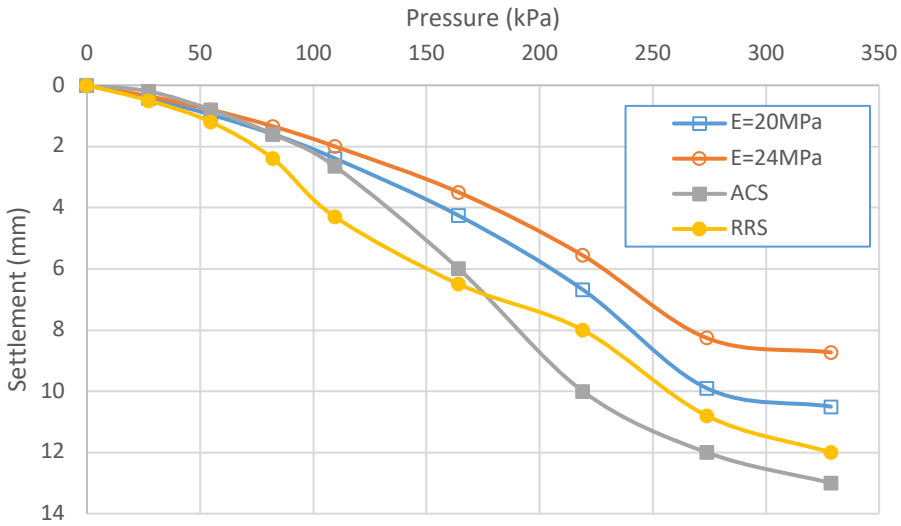

Figure 4.25 Pressure-settlement curves for ACS and RRS compared with the FEM models.

Figure 4.25 illustrates the comparison of pressure vs settlement curves of laboratory tests and the FEM models. It can be seen that for the angular samples, higher settlement values were observed, which is consistent with the numerical models.

There were 6 pressure gauges installed at specific locations of the soil in order to collect data during the plate load test. 2 of them were located at the bottom and 4 were installed on the side wall to measure lateral pressures as shown in Figure 4.26.

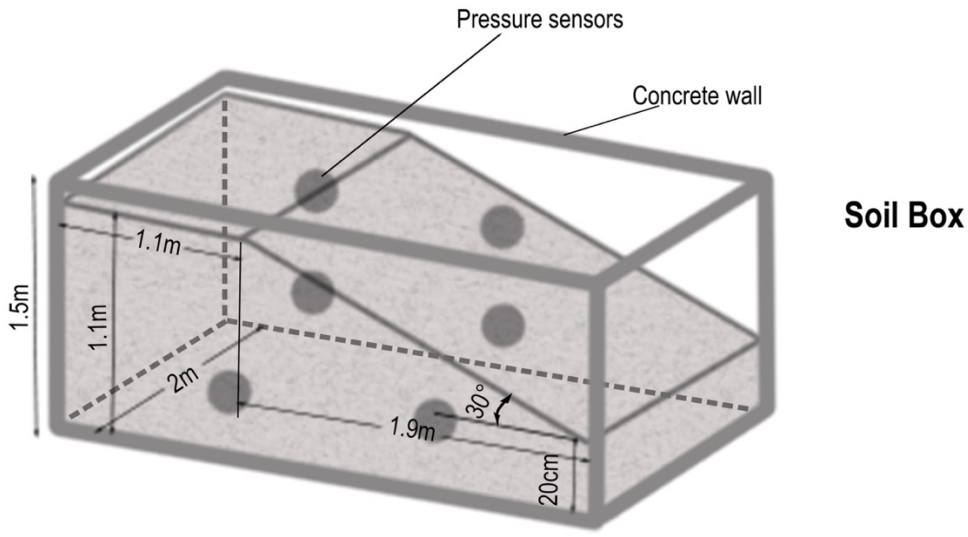

Figure 4.26 Pressure gauge installments in the soil box

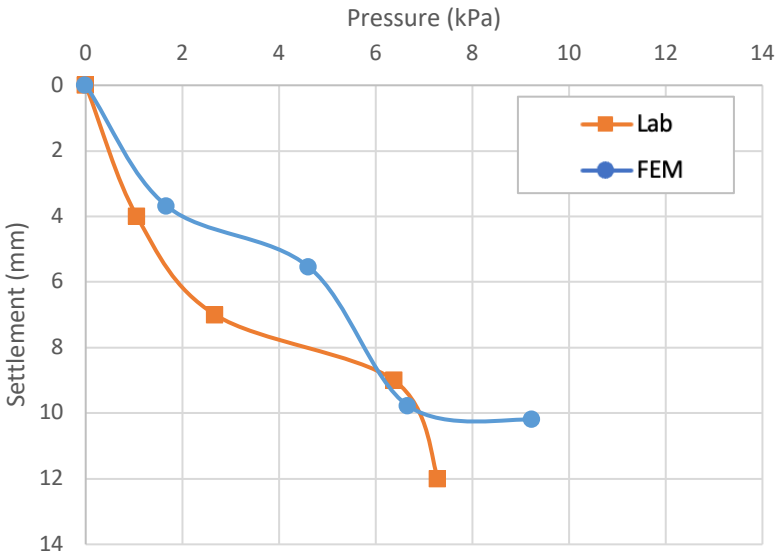

Figure 4.27 Pressure-settlement curve for the pressure gauge at back top location for RRS and the FEM model E=24

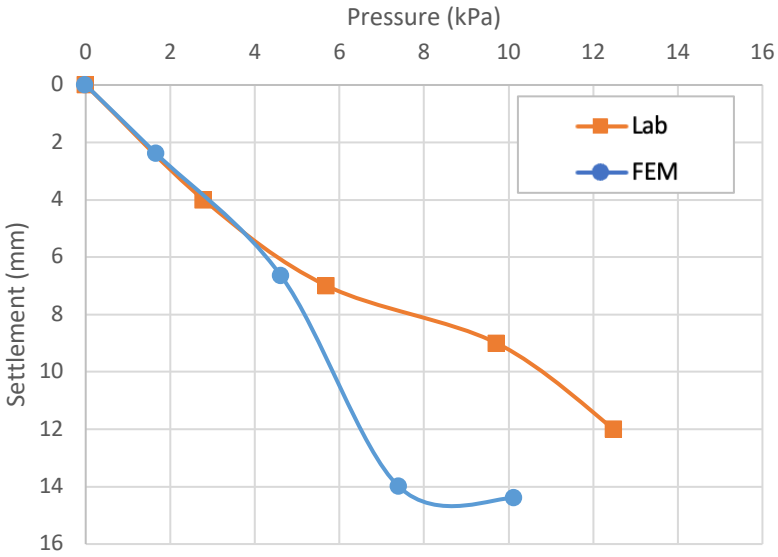

Figure 4.28 Pressure-settlement curve for the pressure gauge at back top location for ACS and the FEM model E=20

Figures 4.27 and 4.28 show the graphs for the pressure gauge located at back top location for the ACS and RRS samples compared with corresponding numerical models. It can be observed from the graphs that as the pressure increases near the failure point settlements values tend to go down in the y axis for the laboratory results,

whereas in the FEM, as the soil failure approaches, the settlement values tend to stay around the same. The reason for this behavior is that, in the physical laboratory experiments, the load is keep being applied even after failure, resulting in a downwards curve at the end of the plots. Figures 4.29 and 4.30 show the relationship of the pressure values obtained from the pressure gauge located at back top position for the ACS and RRS between the laboratory results and the 3D FEM analysis. The dashed lines represent the trendline between the data points. For each of the plots the trendline equation was given inside the graph. The results indicate that there is an 87% and 90% correlation rate for the RRS and ACS for this particular pressure gauge.

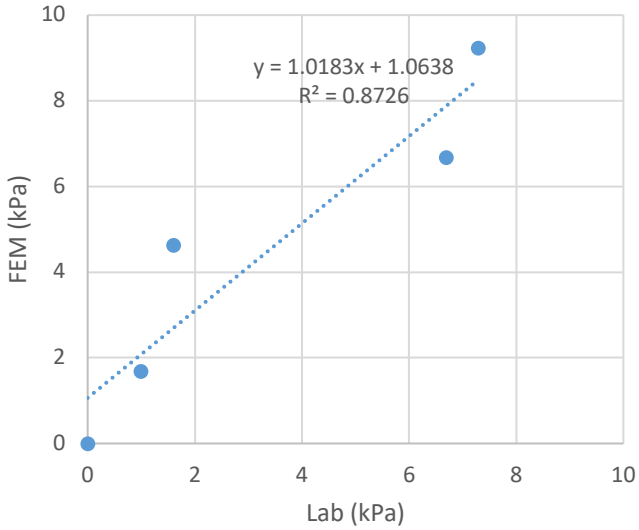

Figure 4.29 Relationship of the pressure values for the pressure gauge at back top location for RRS and the FEM model E=24

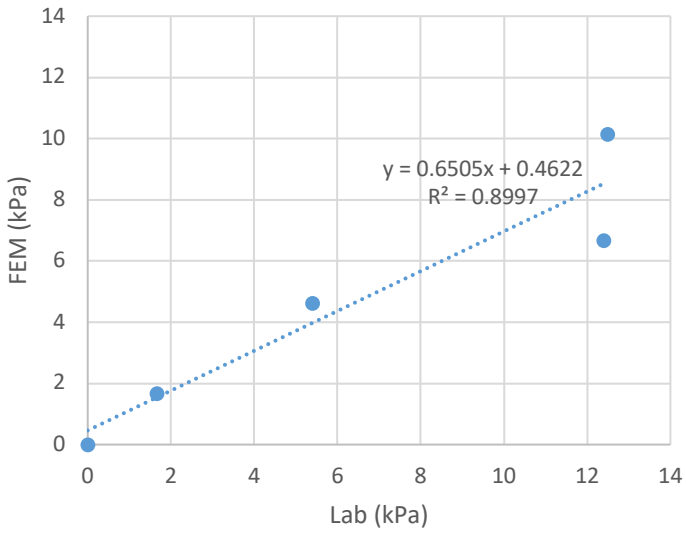

Figure 4.30 Relationship of the pressure values for the pressure gauge at back top location for ACS and the FEM model E=20

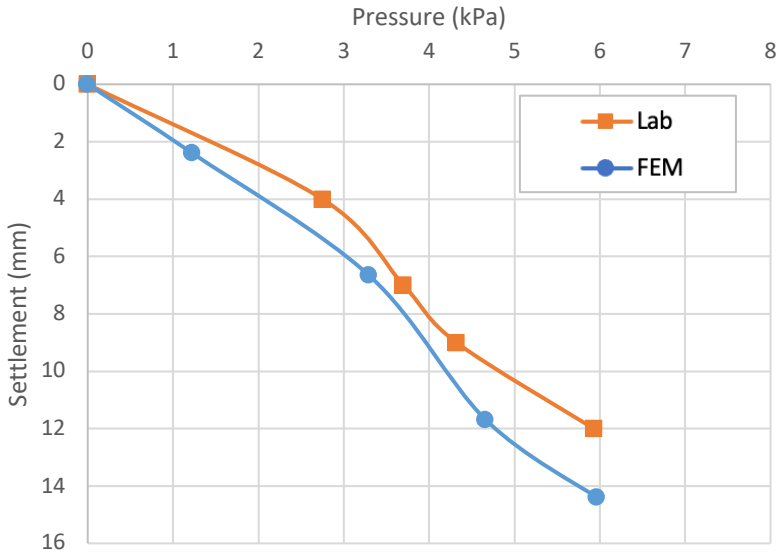

Figure 4.31 Pressure-settlement curve for the pressure gauge at back bottom location for RRS and the FEM model E=24

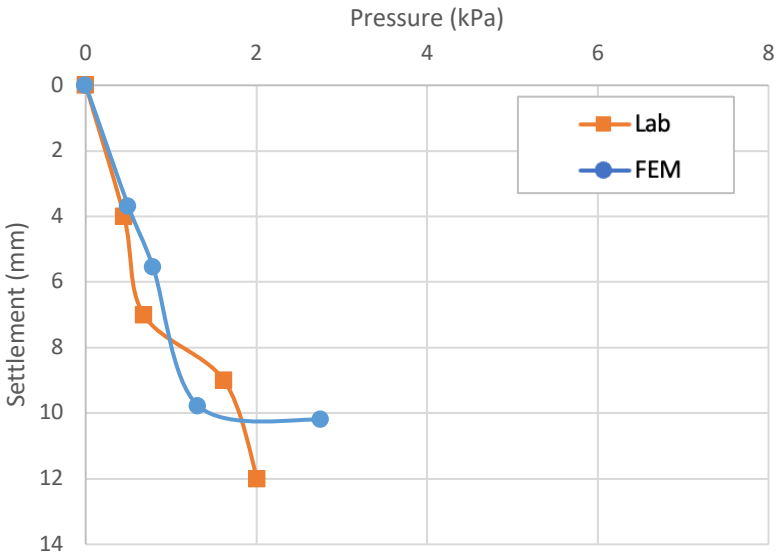

Figure 4.32 Pressure-settlement curve for the pressure gauge at back bottom location for ACS and the FEM model E=20

The most consistent values were collected from the pressure gauge installed at back bottom location. Comparisons of the values obtained from this gauge with the numerical analysis model is given in Figures 4.31 and 4.32. As can be seen from the figures, the graphs from the laboratory experiments more closely follow the pattern of the numerical ones compared with the previous gauge results.

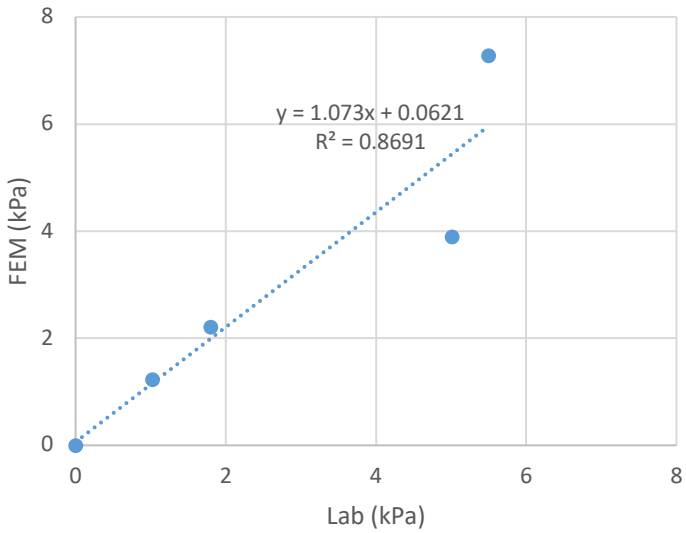

Figure 4.33 Relationship of the pressure values for the pressure gauge at back bottom location for RRS and the FEM model E=24

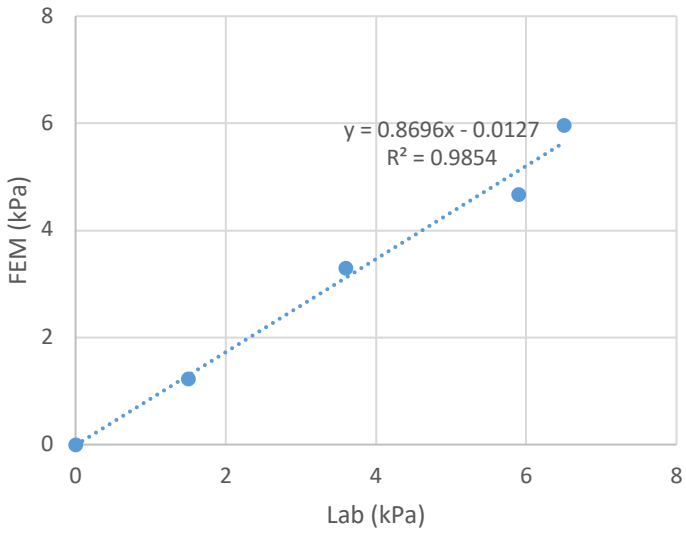

Figure 4.34 Relationship of the pressure values for the pressure gauge at back bottom location for ACS and the FEM model E=20

High correlation rates were calculated for this particular pressure gauge positioned at back bottom location. Figures 4.33 and 4.34 show the correlation plots of the ACS and RRS values obtained through the laboratory experiments and the FEM analysis. According to the results it can be seen that there is an 87% and a 99% correlation rate between the laboratory and simulation results for the RRS and ACS, respectively.

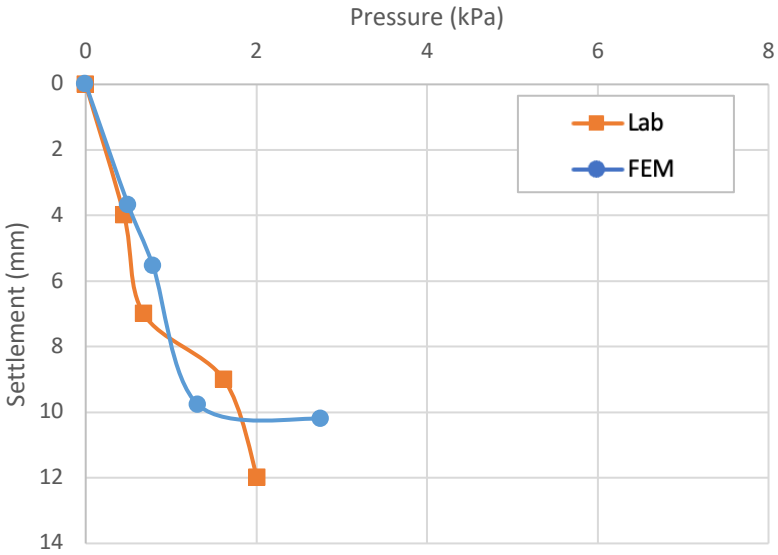

Figure 4.35 Pressure-settlement curve for the pressure gauge at front top location for RRS and the FEM model E=24

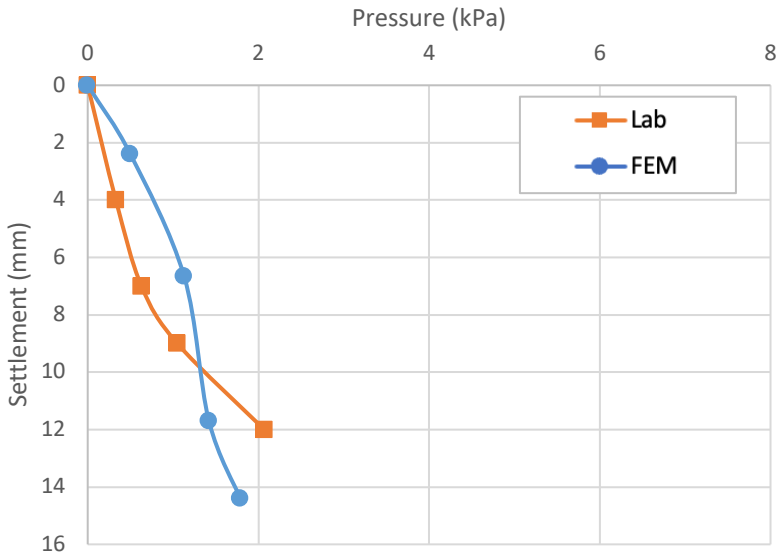

Figure 4.36 Pressure-settlement curve for the pressure gauge at front top location for ACS and the FEM model E=20

Figures 4.34 and 4.35 show the comparison graphs for the pressure gauge located at front top location for the ACS and RRS samples. It can be seen that the pressure gauge at this location shows consistent results with the previous measurements. Since the location was close to the surface and under the slope, the pressure readings from this particular gauge were smaller compared to the other ones. The maximum recorded pressures at 12 mm settlement were 2.01 kPa and 2.07 for RRS and ACS, respectively whereas the maximum readings for the numerical model were 2.76 kPA at 10.2 mm and 1.79 kPA at 14.4 mm.

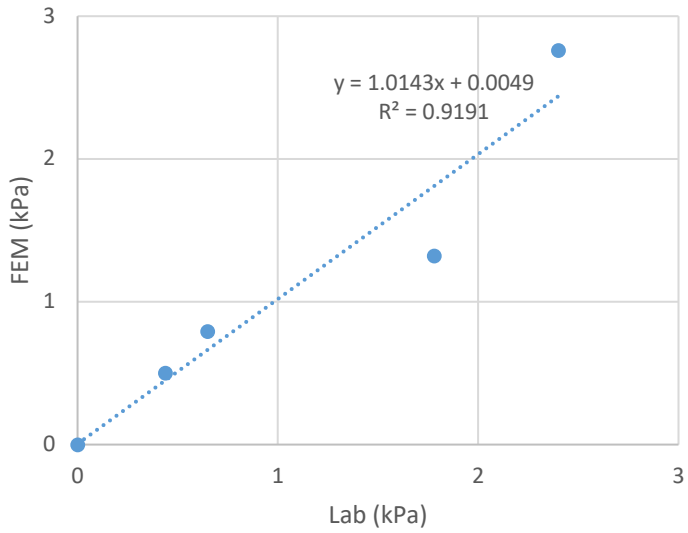

Figure 4.37 Relationship of the pressure values for the pressure gauge at front top location for RRS and the FEM model E=24

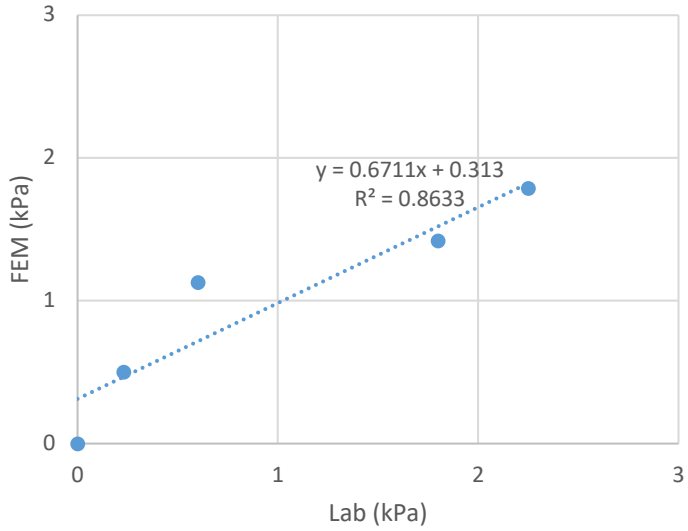

Figure 4.38 Relationship of the pressure values for the pressure gauge at front top location for ACS and the FEM model E=20

As can be seen from Figures 4.37 and 4.38, the relationship between the numerical models and the experimental values concerning this pressure gauge indicate a 91% and an 86% correlation rate for RRS and ACS samples, respectively.

The fourth lateral pressure gauge placement was at front bottom location. The comparison graphs for the ACS and RRS samples are given in Figures 4.39 and 4.40.

A 95% correlation rate was calculated between the experimental values and numerical values for this gauge as can be seen in Figures 4.41 and 4.42. Figure 4.43 shows the relationship between the results obtained from bottom pressure gauges and the numerical model. The results indicate that there is a 93% and a 94% correlation rate between the numerical and the experimental models.

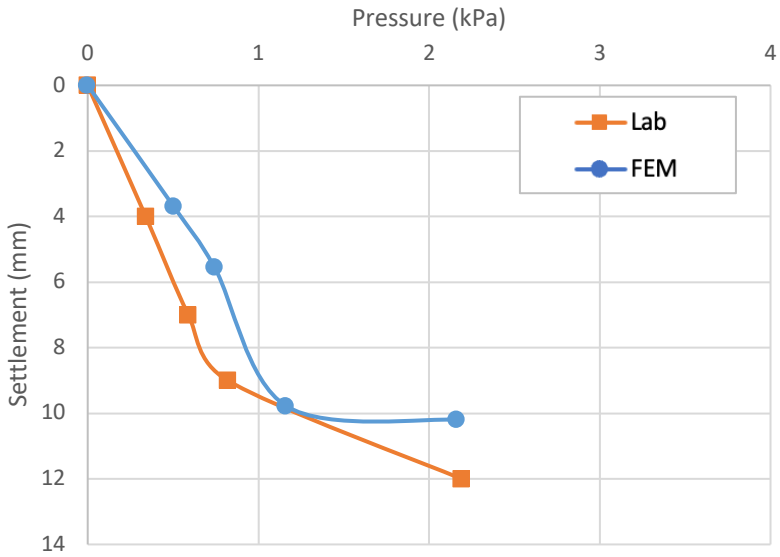

Figure 4.39 Pressure-settlement curve for the pressure gauge at front bottom location for RRS and the FEM model E=24

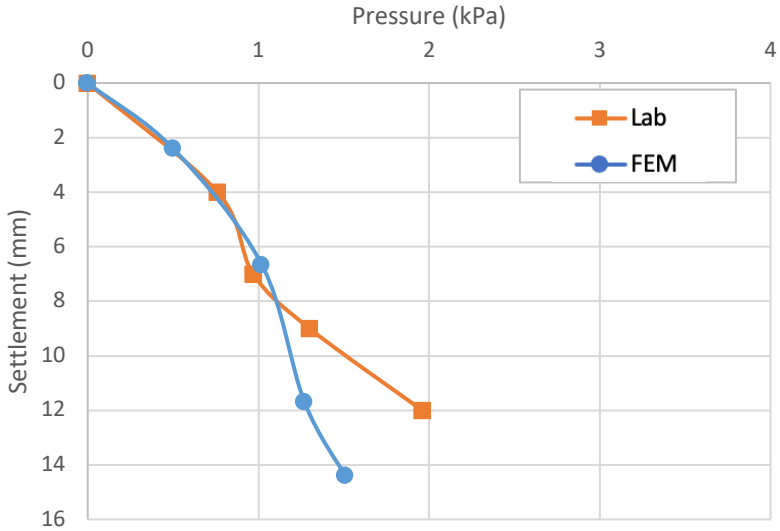

Figure 4.40 Pressure-settlement curve for the pressure gauge at front bottom location for ACS and the FEM model E=20

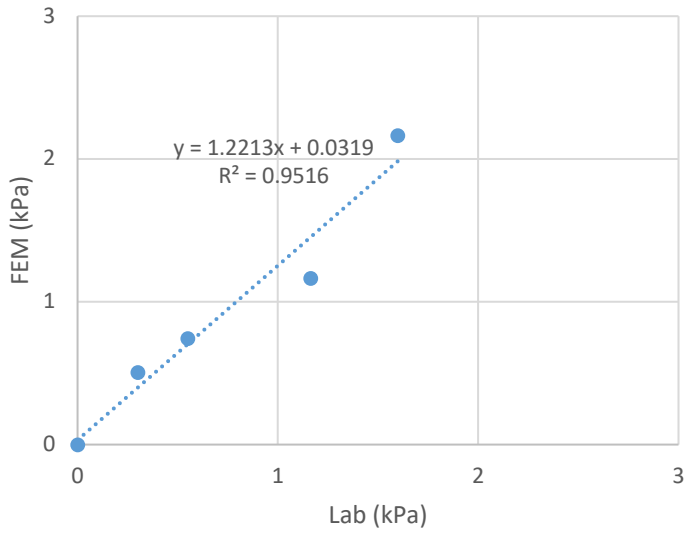

Figure 4.41 Relationship of the pressure values for the pressure gauge at front bottom location for RRS and the FEM model E=24

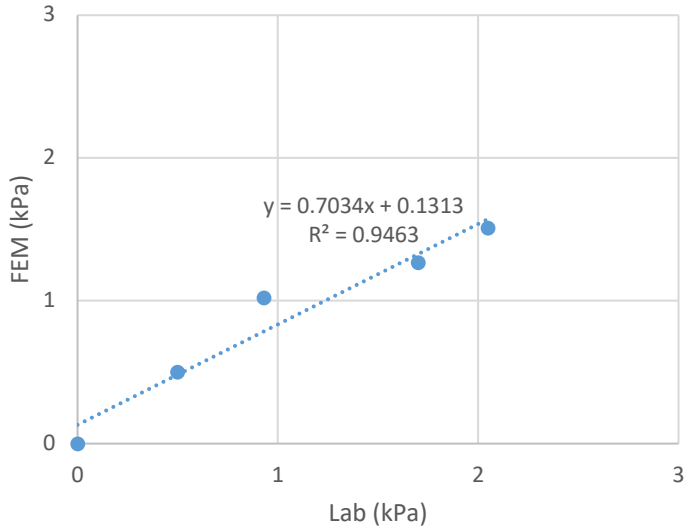

Figure 4.42 Relationship of the pressure values for the pressure gauge at front bottom location for RRS and the FEM model E=20

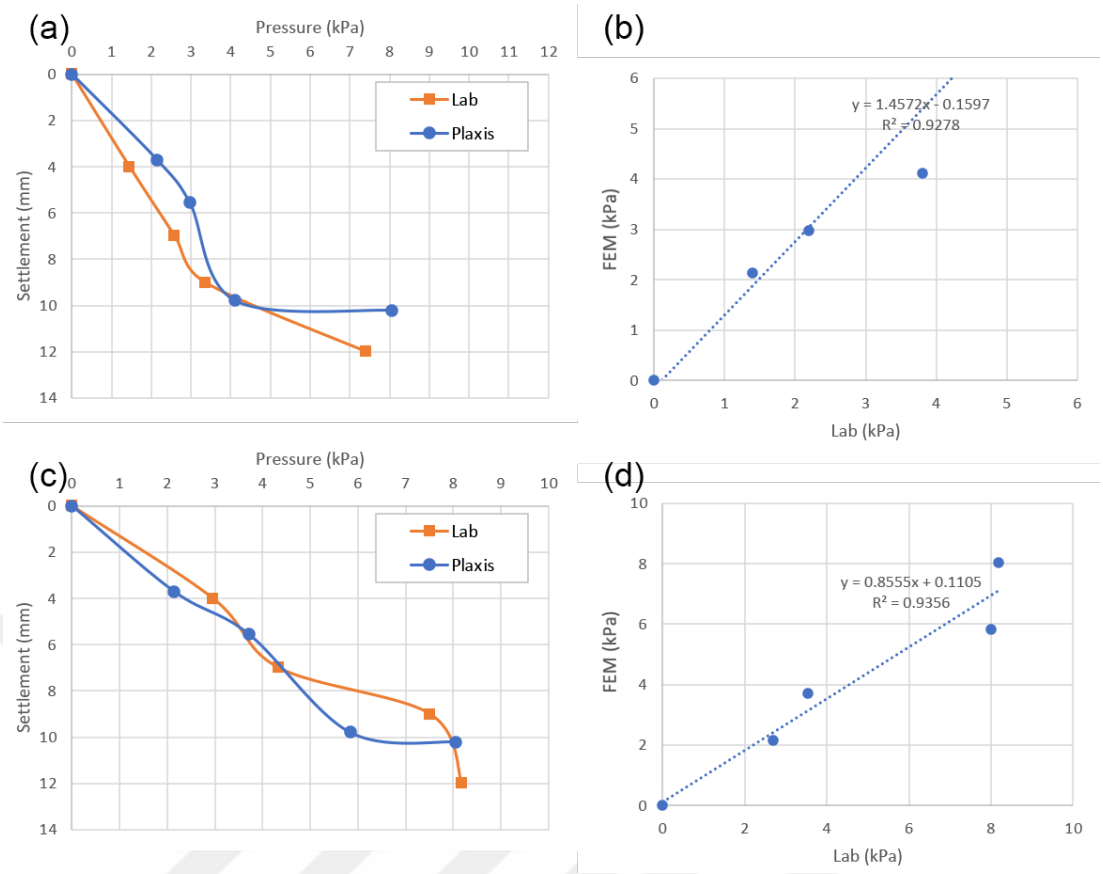

Figure 4.43 Pressure-settlement curves for the pressure gauge at bottom locations for RRS and the FEM model E=24 and their correlation graphs

4.3 Relationship between ICF and stiffness values

An intensive series of laboratory experiments were conducted using the 3m x 2m x 1.5m large-scale soil box. ACS and CCS grains were also taken for shape analysis to determine their ICF values as shown in Table 4.8.

Table 4.8 Shape analysis results for the ACS and CCS samples

Sample	ICF	Standard deviation	E (Modulus of elasticity)
ACS	0.45	0.13	20 MPa
RRS	0.54	0.13	24 MPa

As can be seen from Table 4.8, a group of grains were selected for shape analysis from each sample set. Their standard derivative values were found to be 0.13. All the

experiments were carried out in dry conditions. The results indicate that a 20% increase in ICF value causes a 20% increase in modulus of elasticity value.

CHAPTER V

CONCLUSIONS

5.1 General

The aim of this thesis is to study the behavior of sandy soil with relation to different shape variations in the micro scale, find relationships to understand and explain the behavior of the soil in this regard. A datalogger system was built, an intensive series of laboratory tests have been conducted in order to derive a relationship between shape characteristics of the soil and the effect on its strength. Furthermore, 3D analyses were also done using an FEM application (PLAXIS 3D) and comparisons were made between the numerical analyses and the laboratory test results. A steel loading frame with a capacity of 40 ton were used during the plate load testing procedures. A sloped soil model was developed and different soil samples were filled using an apparatus to achieve a 30-degree slope. The shape of the soil was characterized using a novel technique to assess the shape of the sand.

The primary objectives of the present research can be outlined as follows:

1. Define a new shape factor and show its efficiency by comparing it to the traditional method of roundness (This comparison should ideally be made digital representation of the method in order to minimize the subjectivity involved in assessing the roundness values)
2. To study the shape characteristics of several different sand samples of varying sizes using Scanning Microscope Imaging and digital image processing
3. To build a monitoring and a datalogger system which will be used in the large-scale slope model tests
4. Build 3D models and conduct numerical analyses of various samples in a computer software

5. Conduct experiments in the large-scale slope model and get stress readings from various locations of the soil in order to have a large collection of data to interpret the tests

The current research has completed all of its objectives. Regarding the objectives that are mentioned, two main studies were conducted in which the results are shown with the correlation values: (1) A novel shape factor was developed and a computer algorithm was given that shows its usage. This shape factor was compared with the program developed by Zheng et al (2015), (2) An extensive series of laboratory tests were conducted and compared with the numerical analyses made on PLAXIS. These results were used to show the behavior of the soil using the newly developed shape factor.

5.2 Conclusions for the Shape Factor Studies

A novel shape factor, which is named ICF for soils was presented using eight different types of granular materials (NS, CSS, TS, LBS, OS, TOS, fly ash, mica). The new shape factor and the method was evaluated by comparisons with the program by Zheng et al (2015) written in MatLAB, which calculates the shape factors automatically based on traditional definition of roundness (R). Their program was chosen in order to remove subjectivity while assessing the new method. The study reported the following about the new method:

1. The method showed up to 91% correlation with the calculated roundness values.
2. It was seen that the shape factor is closer to the roundness values for more angular and irregular shapes. The average values of ICF/R ratio of the TS sample were 1.01.
3. It is shown that it produced more consistent results for shapes that have too many concave corners.

The results suggest that the ICF produces consistent results and is more sensitive to shape changes for more rounded particles. Moreover, since the method is based on the OpenCV library, which is a cross platform and highly optimized open-source library

with a large community, it will be easy for other researchers to change it and optimize it, or develop it further for other purposes.

5.3 Conclusions for the Large-Scale Slope Box Experiments

In order to understand the effect of sand particle shape on its behavior, two sand samples of varying shape properties were investigated using a large-scale soil box model. The results were compared using software simulations. The outcome from the study can be summarized as follows:

1. The software simulations showed between 86%-99% correlation rate with the pressure readings from the laboratory.
2. An increase of 20% in the ICF value caused a 20% increase in the modulus of elasticity ratio.
3. The results of the plate load test showed that the increase in the ICF value improved the ultimate bearing capacity of sand.

5.4 Recommendations for Future Studies

The results and conclusions from the numerical studies encourage further investigation. Shape and size analysis methods are always growing, and they provide an alternative viewpoint to soil problems. Some recommendations can be given in order to study the effect of the shape more in depth. Some of the suggestions for further research can take into consideration the following:

- Since these studies were carried out in a large-scale box, only 2 kinds of materials were able to be tested within the limited timeframe. More sand samples with varying values of ICF's can be used to compare the results.

- The current study may be extended to use different percentages of water with the sand.

- Triaxial or cyclic triaxial tests can be performed in order to verify the results, and to understand the characteristics of sand with respect to the ICF value.

- Adjustments to the soil box can be done in order to study the effect of the change in the bearing plate.

- The test results can be compared using a different software, which can make discrete element simulation, or flow simulation, and the results can be correlated with the soil properties.

REFERENCES

Abramson, LW; Lee, TS; Sharma, S and Boyce, G.M. (2002). *Slope Stability Concepts. Slope Stabilisation and Stabilisation Methods*, second edition, published by John Willey & Sons, Inc., 329 - 461.

Ahmed, J., Ghazali, M. A., Mukhlisin, M., Alias, M. N. and Taha, M.R. (2011). Effectiveness of Horizontal Drains in Improving Slope Stability: A Case Study of Landslide Event in Putrajaya Precinct 9, Malaysia. *Unsaturated Soils: Theory and Practice:* 753-758.

Alshibli, K. 2020. Alshibli - Archives Of Granular Materials. [online] Alshibli.utk.edu. Available at: <https://alshibli.utk.edu/research/MGM/archives.php> [Accessed 31 May 2020].

Alshibli, K.A., Alsaleh, M.I. 2004. Characterizing surface roughness and shape of sands using digital microscopy, *Journal of Computing in Civil Engineering* **18(1)**, 36–45. doi.org/ 10.1061/(asce)0887-3801(2004)18:1(36)

ASTM C136, (2014). Standard Test Method for Sieve Analysis of Fine and Coarse Aggregates. American Society for Testing and Materials.

Barrett, P.J. 1980. The shape of rock particles: a critical review. *Sedimentology* **27(3)**, 291–303. doi.org/10.1111/j.1365-3091.1980.tb01179.x

Bishop, A.W. (1955). "The use of slip circles in stability analysis of slopes", *Geotechnique*, **5(1)**, 7-17.

Bowman, E.T., Soga, K., Drummond, W. 2001. Particle shape characterization using Fourier descriptor analysis. *Géotechnique* **51(6)**, 545–554. doi.org/10.1680/geot.2001.51.6. 545

Burland, J.B., Burbidge, M.C. (1984). Settlement of foundations on sand and

gravel.*Proceedings of the Institution of Civil Engineers*, **78**, 1325-1381.

Chapuis, R.P. 2012. Estimating the in situ porosity of sandy soils sampled in boreholes. *Engineering Geology* **141–142(19)**, 57–64. doi.org/10.1016/j.enggeo.2012.04.015

Cho, G.C., Dodds, J., Santamarina, J.C. 2005. Particle shape effects on packing density, stiffness and strength: natural and crushed sands. *Journal of Geotechnical and Geoenvironmental Engineering* **132(5)**, 591-602. doi.org/10.1061/(asce)1090-0241(2006)132:5(591)

Casagrande, A. (1948). *Classification and identification of soils.*New York, N.Y: American Society of Civil Engineers.

Chowdhury, R., Flentje, P. and Bhattacharya, G. (2009). *Geotechnical Slope Analysis.* Crc Press.

Clark, M.W. 1981. Quantitative shape analysis: a review. *Journal of the International Association for Mathematical Geology* **13(4)**, 303-320. doi.org/10.1007/bf01031516

Craig, R.F. (2004). *Craig's Soil Mechanics.* New York, N.Y: Taylor & Francis.

D. V. Griffiths, P. A. (1999). Lane, Slope stability analysis by finite elements, *Geotechnique*, **3**, 387-403

Das, S.K., Biswal, R.K., Sivakugan, N. et al. (2011). Classification of slopes and prediction of factor of safety using differential evolution neural networks. *Environ Earth Sci,* **64**, 201–210. https://doi.org/10.1007/s12665-010-0839-1

Dawson, E.M., Roth, W.H. and Drescher, A. (1999). Slope Stability Analysis by Strength Reduction, *Geotechnique*, **49(6)**, 835-840.

Demir, B., Sayinci, B., Cetin, N., Yaman, M., Comlek, R. (2019). Shape Discrimination of Almond Cultivars by Elliptic Fourier Descriptors. *Erwerbs-Obstbau* **61(3)**, 245-256. doi.org/10.1007/s10341-019-00423-7

Drevin, G.R. (2006). Computational Methods for the Determination of Roundness of Sedimentary Particles. *Math Geol,* **38**, 871.

Diepenbroek, Michael, Alexander Bartholomä, and Hillert Ibbeken. (1992). "How round is round? A new approach to the topic 'roundness' by Fourier grain shape analysis." *Sedimentology,* **39(3)**, 411-422.

Duke, J., & Rushforth, K. (2021). Main - Main - OpenJDK Wiki. Retrieved 9 January 2022, from https://wiki.openjdk.java.net/display/OpenJFX/Main

Edil, T.B., Krizek, R.J., Zelasko, J.S. (1975). Effect of grain characteristics on packing of sands. *Proceedings of the Istanbul conference on soil mechanics and foundation engineering, Istanbul*, 46–54.

Ehrlich, R., Brown, P.J., Yarus, J.M., Przygocki, R.S. (1980). The origin of shape frequency distributions and the relationship between size and shape. *SEPM Journal of Sedimentary Research* **50**. doi.org/10.1306/212f7a2c-2b24-11d7-8648000102c1865d

Ehrlich, R., Weinberg, B. (1970). An exact method for characterization of grain shape. *SEPM Journal of Sedimentary Research* **40(l)**. doi.org/10.1306/74d71f1e-2b21-11d7-8648000102c1865d

Eisma, D. (1965). Eolian sorting and roundness of beach and dune sands. *Netherlands Journal of Sea Research* **2(4)**, 541–555.doi.org/10.1016/0077-7579(65)90002-5

Farin., G. (1993). *Curves and surfaces for computer aided geometric design. A practical guide.* Acad. Press.

Fellenius, W. (1936). Calculation of the Stability of Earth Dams, Transaction, *2nd Congress on Large Dams*, **4**, 445-462.

Folland, G. B. 1992. *Fourier Analysis and its Applications*. Belmont, CA, USA.

Fontanet A, Autran B, Lina B, Kieny MP, Abdool Karim SS, Sridhar D. (2021). SARS-CoV-2 variants and ending the COVID-19 pandemic. *Lancet*. 2021;397:952–954.

Friedrich, H.G., (2011). *Assessment of Sand and Gravel and Clay Deposits in Parts of Northern St. Louis and Lake Counties*. (Report no. 380), Minnesota Department of Natural Resources Division of Lands and Minerals.

Frossard, E. (1979). Effect of sand grain shape on the interparticle friction; indirect measurements by Rowe's stress dilatancy theory. *Géotechnique* **29(3)**, 341–35. doi.org/10.1680/geot.1979.29.3.341

Görüm, T., Fidan, S. (2021). Spatiotemporal variations of fatal landslides in Turkey. *Landslides,* **18**, 1691–1705 https://doi.org/10.1007/s10346-020-01580-7

Griffiths, D.V., and Lane, P.A. (1999). Slope Stability Analysis by Finite Elements, *Geotechnique*, **49(3)**, 387-403.

Hammah, R.E., Curran, J.H., Yacoub, T.E., and Corkum, B. (2004). Stability Analysis of Rock Slopes using the Finite Element Method. *ISRM Regional Symposium EUROCK 2004 and the 53rd Geomechanics Colloquy, Salzburg, Austria.*

Hammouri, NA; Husein Malkawi, AI and Yamin, M.M.A. (2008). Stability analysis of slopes using the finite element method and limiting equilibrium approach. *Bulletin of Engineering Geology and the Environment*, **67(4)**:471-478.

Hawkins, H.H. (1993). Asymptotic Determination of Run off Curve Numbers from Data. *ASCE Journal of Irrigation and Drainage Engineering* **119(2)**, 334-345. doi.org/10.1061/(ASCE)0733-9437(1993)119:2(334)

Hentschel, M.L., Page, N.W. (2003). Selection of descriptors for particle shape characterization. *Particle & Particle Systems Characterization* **20(1)**, 25–38. doi.org/10.1002/ppsc.200390002

Hryciw, R.D., Zheng, J., Shetler K. 2016. Particle roundness and sphericity from images of assemblies by chart estimates and computer methods *J. Geotech. Geoenviron. Eng.*, **142**

Imai, T. and Yoshimura, Y. (1970). Elastic wave velocity and Soil properties in soft soil. *Tsuchi-to-Kiso*, **18**, 17-22.

Isik, H. (2014a). [online] Available at: http://www.gantep.edu.tr/~halukisik/sieve-analysis.xlsm [Accessed: 1 March 2022].

Isik, H. (2014b). [online] Available at: http://www.gantep.edu.tr/~halukisik/spt-

correlation.xlsm [Accessed: 1 March 2022].

Işık, H. (2014c). SPT Rocks (1.0) [Mobile application software]. Retrieved from https://itunes.apple.com/ us/app/spt-rocks/id886258382?ls=1&mt=8

Işık, H., Çabalar, A. F. (2014) A Numerical Analysis of the Standard Penetration Test. *11th International Congress on Advances in Civil Engineering*.

Isik, H. & Cabalar, A. (2018). Sieve analysis and standard penetration test correlations using Microsoft Excel VBA and an iPhone app. *Computer Applications in Engineering Education,* **26(6)**, 2092-2101. doi: 10.1002/cae.22002

Isik, H. & Cabalar, A.F. (2022). A shape parameter for soil particles using a computational method. *Arabian Journal of Geosciences*, **(15)**, 581. https://doi.org/10.1007/s12517-022-09777-x

Janbu, N. (1954). *Stability analysis of Slopes with Dimensionless parameters*, Thesis for the Doctor of Science in the Field of Civil Engineering, Harvard University Soil Mechanics Series.

Jaritngam S, Chuchom S, Limsakul C, Jaritngam R. (2001). Slope stability analysis using neural networks. In: *The 6th mining, metallurgical and petroleum engineering conference on resources exploration and utilization for sustainable environment (REUSE)*. 24–6.

Jiang YS. (1990). *Slope analysis using boundary elements.* New York: Springer-Verlag Publishers.

Karim, S., & Karim, Q. A. (2021). Omicron SARS-CoV-2 variant: a new chapter in the COVID-19 pandemic. *Lancet* (London, England), **398(10317)**, 2126–2128. https://doi.org/10.1016/S0140-6736(21)02758-6

Kandasami, R., Murthy, T. (2014). Effect of particle shape on the mechanical response of a granular ensemble. *Geomechanics from Micro to Macro*, Taylor & Francis Group, Abingdon, U.K., 1093–1098.

Knodel, P., Yudhbir, Abedinzadeh, R. (1991). Quantification of particle shape and

angularity using the image analyzer. *Geotechnical Testing Journal*, **14(3)**, 296–308. doi.org/10.1520/gtj10574j

Koestel, J. (2017). SoilJ: An ImageJ plugin for semi-automatized image-processing of 3-D X-ray images of soil columns. *Vadose Zone Journal* **17(1)**, 170062. doi.org/10.2136/vzj2017.03.0062

Koo, B., Kim, T. (2016). Soil Particle Shape Analysis Using Fourier Descriptor Analysis. *Journal of the Korean Geoenvironmental Society* **17(3)**, 21-26. doi.org/10.14481/jkges.2016.17.3.21

Krumbein, W.C., Sloss, L.L. (1963). *Stratigraphy and Sedimentation,* 2nd edition, Freeman, San Francisco.

Kuhlman, D. (2011). *A Python Book: Beginning Python, Advanced Python, and Python Exercises*, Platypus Global Media

Kumar, A., Rathee, R. (2017). Monitoring and evaluating of slope stability for setting out of critical limit at slope stability radar. *Geo-Engineering,* **8**, 18 https://doi.org/10.1186/s40703-017-0054-y

Lees, G. (1964). A new method for determining the angularity of particles. *Sedimentology,* **1(3)**, 2–21.doi.org/10.1111/j.1365-3091.1964.tb00271.x

Liao, S. S. C., Whitman, R. V. (1986). Overburden correction factors for SPT in sand. *Journal of Geotechnical Engineering Div. Am. Sot.Ciu. Engrs*, **112(3)**, 373-377.

Matsui T, San K. (1992). Finite element slope stability analysis by shear strength reduction technique. *Soils Foundat,* **32**, 59–70.

McGregor, J. A., Duncan, J. M., (1998). *Performance and Use of the Standard Penetration Test in Geotechnical Engineering Practice*, Report of Center for Geotechnical Practice and Research, Virginia Polytechnic Institute, Blacksburg, VA, October 1998.

Meng, Q., Qian, K., Zhong, L., Gu, J., Li, Y., Fan, K., Yan, L. (2020). Numerical Analysis of Slope Stability under Reservoir Water Level Fluctuations Using a FEM-

LEM-Combined Method. *Geofluids*, **2020**, Article ID 6683311. https://doi.org/10.1155/2020/6683311

Niazkar, M. (2020). An Excel VBA ‐ based educational module for bed roughness predictors. *Computer Applications in Engineering Education*, **29(5)**, 1051-1060. doi: 10.1002/cae.22358

Ozbay, A., Cabalar, A.F. (2015). FEM and LEM stability analyses of the fatal landslides at Çöllolar open-cast lignite mine in Elbistan, Turkey. *Landslides* **12**, 155–163. https://doi.org/10.1007/s10346-014-0537-2

Luo CH, Morris CP, Sachithanandham J, et al. (2021). Infection with the SARS-CoV-2 delta variant is associated with higher infectious virus loads compared to the alpha variant in both unvaccinated and vaccinated individuals. *medRxiv*. 2021 doi: 10.1101/2021.08.15.21262077. published online Aug 20. (preprint).

Petley, D. (2012). Global patterns of loss of life from landslides. *Geology* **40(10)**, 927–930. https://doi.org/10.1130/G33217.1

Podczeck, F. (1997). A shape factor to assess the shape of particles using image analysis. *Powder Technology,* **93(1)**, 47-53. doi.org/10.1016/s0032-5910(97)03257-9

Powers, M.C. (1953). A new roundness scale for sedimentary particles. *SEPM Journal of Sedimentary Research,* **23**, 117-119. doi.org/10.1306/d4269567-2b26-11d7-8648000102c1865d

Rauch, A. (1997). *EPOLLS: An Empirical Method for Predicting Surface Displacements Due to Liquefaction-Induced Lateral Spreading in Earthquakes*. Ph.D. Virginia Polytechnic Institute and State University.

Roussillon, T., Piegay, H., Sivignon, I., Tougne, L., Lavigne, F. (2009). Automatic computation of pebble roundness using digital imagery and discrete geometry." *Computers & Geosciences,* **10(35)**, 1992–2000.doi.org/10.1016/j.cageo.2009.01.013

Sagga, A.M.S. (1993). Roundness of sand grains of longitudinal dunes in Saudi Arabia. *Sedimentary Geology,* **87(1-2)**, 63–68. doi.org/10.1016/0037-0738(93)90036-5

Santamarina, J.C., Cho, G.C. (2004). Soil behaviour: The role of particle shape. *Advances in Geotechnical Engineering: The Skempton Conference, Thomas Telford, London*, 604–617.

Santamarina, J.C., Klein, K.A., Fam, M.A. (2001). *Soils and Waves.* Wiley & Sons. Ltd, England, pp. 488.

Sayinci, B., Kara, M., Ercisli, S., Duyar, O., Erturk, Y. (2015). Elliptic Fourier analysis for shape distinction of Turkish hazelnut cultivars. *Erwerbs-Obstbau* **57(1)**, 1-11. doi.org/10.1007/s10341-014-0221-7

Sepúlveda S.A., Petley D.N. (2015). Regional trends and controlling factors of fatal landslides in Latin America and the Caribbean. *Nat Hazards Earth Syst Sci,* **15**:1821–1833. https://doi.org/10.5194/nhess-15-1821-2015

Schwarcz, H. P., and K. C. Shane. (1969). Measurement of particle shape by Fourier analysis. *Sedimentology* **13(3-4),** 213-231.

Sezer, A. (2008). *Goruntu Isleme Teknikleri Kullanilarak Farkli Turlerde Zeminlerin Mikroyapisal Ozelliklerinin Belirlenmesi.* Doctoral thesis, Ege University, Izmir, Turkey.

Shin, H., Santamarina, J.C. (2013). Role of particle angularity on the mechanical behavior of granular mixtures. *Journal of Geotechnical and Geoenvironmental Engineering,* **139(2)**, 353–355. doi.org/10.1061/(asce)gt.1943-5606.0000768

Sowers, G. and Sowers, G. (1979). *Introductory soil mechanics and foundations*. 1st ed. New York: Macmillan.

Standard Practice for Classification of Soils for Engineering Purposes. (2011). Philadelphia, Pa.: ASTM International.

Stead, D. (2016). The Influence of Shales on Slope Instability. *Rock Mech Rock Eng* **49**, 635–651. https://doi.org/10.1007/s00603-015-0865-0

Stroud, M. (1974). The standard penetration test in insensitive clays and soft rock. Stockholm, Sweden: *European Symposium on Penetration Resistance, National*

Swedish Institute for Building Research, 367-375.

Sukumaran, B., Ashmawy, A.K. (2001). Quantitative characterization of the geometry of discrete particles. *Géotechnique* **51(7)**, 171–179. doi.org/10.1680/geot.2001.51.7.619

Rauch, A. (1997). *EPOLLS: An Empirical Method for Predicting Surface Displacements Due to Liquefaction-Induced Lateral Spreading in Earthquakes*. Ph.D. Virginia Polytechnic Institute and State University.

Resentini, Alberto, Sergio Ando, and Eduardo Garzanti (2018). Quantifying roundness of detrital minerals by image analysis: Sediment transport, shape effects, and provenance implications. *Journal of Sedimentary Research,* **88(2)**, 276-289.

Thomas, M.C., Wiltshire, R.J., Williams, A.T. (1995). The use of Fourier descriptors in the classification of particle shape. *Sedimentology* **4(42)**, 635-645. doi.org/10.1111/j.1365-3091.1995.tb00397.x

Tralic, D., Bozek, J., Grgic, S. (2011). Shape Analysis and Classification of Masses in Mammographic Images using Neural Networks. Systems, *Signals and Image Processing (IWSSIP), 18th International Conference.*

Vepraskas, M.J., Cassel, D.K. (1987). Sphericity and roundness of sand in coastal plain soils and relationships with soil physical properties. *Soil Science Society of America Journal,* **51(5)**, 1108–1112.doi.org/10.2136/sssaj1987.03615995005100050003x

Wadell, H. (1932). Volume, shape and roundness of rock particles. *The Journal of Geology,* **40(5)**, 443–451.doi.org/10.1086/623964

Wadell, H. (1933). Sphericity and roundness of rock particles. *The Journal of Geology* **41(3)**, 310–331.doi.org/10.1086/624040

Wadell, H. (1935). Volume, shape, and roundness of quartz particles. *The Journal of Geology,* **41(3)**, 250–280.doi.org/10.1086/624298

Wang, X. (2017). On the slopes of semistable representations of tame quivers, *Communications in Algebra*, **45(11)**, 4809-4816.

https://doi.org/10.1080/00927872.2017.1284223

Wettimuny, R., Penumadu, D. (2004). Application of Fourier analysis to digital imaging for particle shape analysis. *Journal of Computing in Civil Engineering,* **18(1)**, 2–9. doi.org/10.1061/(asce)0887-3801(2004)18:1(2)

What is Arduino?. (2018). Retrieved 9 January 2022, from https://www.arduino.cc/en/Guide/Introduction

What is Gradle?. (2022). Retrieved 9 January 2022, from https://docs.gradle.org/current/userguide/what_is_gradle.html

Xue, X., Li, Y., Yang, X., Chen, X., & Xiang, J. (2015). Prediction of Slope Stability Based on GA-BP Hybrid Algorithm. *Neural Network World*, **25**, 189-202.

Yin, Z., Teng, J., Wang, H., & Jin, Y. (2021). A MATLAB‐based educational platform for analysis of slope stability. *Computer Applications in Engineering Education*. doi: 10.1002/cae.22474

Yuan, W. B., Ye, C. M., Yao, J., & Wang, L.D. (2012). Stability Analysis of Mountain Slope Based on Finite Element and Discrete Element. *Applied Mechanics and Materials,* **170-173**, 1087–1090. Trans Tech Publications, Ltd. https://doi.org/10.4028/www.scientific.net/amm.170-173.1087

Zekkos, D. (2001). [online] Available at: http://www.geoengineer.org/ sptprogram.html [Accessed: 10 June 2014].

Zekkos, D. (2004). Reliability of shallow foundation design using the standard penetration test. *ISC-2 on Geotechnical and geophysical Site Characterization, Viana da Fonseca & Mayne (eds.), Millpress, Rotterdam*, pp.1575--1582.

Zhang, D., Lu, G. (2005). Study and evaluation of different Fourier methods for image retrieval. *Image and Vision Computing* **23(1)**, 33-49. doi.org/10.1016/j.imavis.2004.09.001

Zheng, J., Hryciw, R.D. (2015). Traditional soil particle sphericity, roundness and surface roughness by computational geometry. *Géotechnique* **65(6)**, 494–506.

doi.org/10.1680/geot.14.p.192

Zingg, T. (1935). *Beitrag zur Schotteranalyse.* Doctoral thesis, ETH Zürich. doi.org/10.3929/ethz-a-000103455

CIRRICULUM VITAE

PERSONAL INFORMATION

Name and Surname : Haluk IŞIK

EDUCATION

Degree	Graduated School	Year
MS	Istanbul Technical University	2013
BS	Istanbul Technical University	2007

WORK EXPERIENCE

Year	Place	Enrollment
2013 - Present	Gaziantep University	Research Assistant

PUBLICATIONS

International Journals

1. **Işık H.,** Çabalar, A. F. (2022) Remote Data Logging and Monitoring Plate Load Tests During the Covid-19 Pandemic. *Ingeniería e Investigación* (in review)

2. **Işık H.,** Çabalar, A. F. (2022) A Shape Parameter for Soil Particles Using Computational Analysis. *Arabian Journal of Geosciences.*

3. Çabalar, A. F., **Işık H.** (2019) Use of spiral aluminum CNC milling waste in road pavement subgrade.

4. Çabalar, A. F., Abdulnafaa, M. D., **Işık H.** (2019) The role of construction and demolition materials in swelling of a clay. *Arabian Journal of Geosciences.*

5. **Işık H.,** Çabalar, A. F. (2018) Sieve Analysis and Standard Penetration Test Applications for Geotechnical Engineering Students. *Computer Applications in Engineering Education.*

6. Edinçliler, A., Çabalar, A. F., Çevik, A., **Işık H.** (2018) New formulations for dynamic behavior of sand-waste tire mixtures in a small range of strain amplitudes. *Periodica Polytechnica Civil Engineering.*

International/National Congress, Conference and Symposium

1. **Işık, H.**, Çabalar, A. F. (2014) A Numerical Analysis of the Standard Penetration Test. *11th International Congress on Advances in Civil Engineering.*

2. Çabalar, A.F., Akbulut, N., **Işık, H.** (2014) On the transition fines contents of sand- clay mixtures. *IS-Cambridge 2014.*

3. **Işık, H.**, Çabalar, A. F. (2014) A Numerical Classification of Soils. 8th *European Conference on Numerical Methods in Geotechnical Engineering.*

4. Karabash Z., Çabalar A. F., **Işık H.** (2015) Stabilization of clayey soil by waste steel pieces. *The International Conference on Civil and Environmental Engineering (ICOCEE - Cappadocia 2015)*

5. **Işık H.**, Akbulut N., Çabalar A. F. (2016) Stabilization of clayey soil by incinerated sewage sludge ash. *The International Conference on Civil and Environmental Engineering (ATINER - 6th Annual International Conference on Civil Engineering in Athens, Greece).*

6. **Işık H.**, Akbulut N., Çabalar A. F. (2016) Unconfined Compressive Strength Test on Sewage Sludge Ash - Clay Mixtures, *4th International Conference on New Developments in Soil Mechanics and Geotechnical Engineering 2-4 June 2016, Near East University, Nicosia, North Cyprus*.

7. Yalçın H., Çabalar A. F., **Işık H.** (2016) A Case Study of Retaining Piles in Limestone Using Plaxis 2D, *World Congress on Civil, Structural, and Environmental Engineering (CSEE'16).*